Micromachined Silicone Rubber Membrane Valves for Fluidic Applications

Thesis by

Xing Yang

In Partial Fulfillment of the Requirements

For the Degree of

Doctor of Philosophy

California Institute of Technology

Pasadena, CA 91125

1999

(Submitted July 27, 1998)

To my parents

Acknowledgments

I would like to thank my advisor, Prof. Yu-Chong Tai, for giving me a chance to have fun, teaching me how to have fun, and letting me have fun in the exciting field of MEMS. Without his advice, guidance, and support, I would not have accomplished what I have achieved in my six years at Caltech. I also thank Prof. Chih-Ming Ho of UCLA, our project PI, for his advice and help.

My thanks go to previous members of our group, especially Drs. Jianqiang Liu and Chang Liu, for helping me start in our lab. Through my six years at Caltech, I have enjoyed a close collaboration with a number of people who I feel fortunate to count as both colleagues and friends. In particular, I am deeply indebted to my partner, Mr. Charles Grosjean, one of the most creative people I have ever known. During the last two years, I have worked closely with him on valves. The project would never have been successful without his brilliant ideas and technical skills. Sincere thanks also go to Dr. Sang-Wook Lee for his friendship. I got to know him at one of the most difficult moments of my life. I thank him not only for his technical help, but more importantly for teaching me many things about life by sharing with me his experiences. My gratitude goes to Ms. Ellis Meng for her tremendous help with testing and proofreading the entire thesis. I also want to thank my fellow student, Dr. Thomas Tsao, for sharing with me his understanding of graduate school, life, and many other things through many long, late night discussions. His help with managing the lab is appreciated by me and all the other people in the group. I have no doubt that he will be successful for what he wants to do.

I would like to thank other members of our group, especially Mr. Shuyun Wu (and his family), Mr. Xuan-Qi Wang, Mr. Tze-Jung Yao, Mr. Wen Hsieh, Mr. Amish Desai, Mr. John Wright, Dr. Tseng Yang Hsu, and Dr. Weilong Tang or their help during my stay at Caltech.

Thanks are due to Dr. Joon Mo Yang of UCLA for his friendship and help with fluid dynamic testing of membrane filters. I thank Dr. Douglas Kerns for many stimulating discussions of technical issues and proofreading some papers I published.

I also wish to thank Dr. Tai's family, especially his wife, Judy, not only for taking care of some travel arrangements, but also for the spiritual encouragement she gave to me during the last few years. The help from Prof. Tai's secretary, Ms. Janice Tucker, is greatly appreciated. Janice has taken care of all the administrative things so that I can concentrate on my research.

My thanks go to our technician, Mr. Trevor Roper. Without his help with the equipment, my life in the lab would be much more difficult and the research would never be finished on time.

I thank my friend, Robert Good, and his parents, Robert and Ruth Good, for helping me get over the culture shock when I first came to this country, and their generosity and hospitality they have shown to me since then. The same thanks go to Robert and Darlene Egge.

Words can not describe my thanks to my parents whom I dedicate this thesis to. Through their words and examples, they have taught me many invaluable lessons in life that I could not learn from any classroom. I know without many years of their sacrifice, understanding, encouragement, love, and support, I would not achieve anything in my life.

Micromachined Silicone Rubber Membrane Valves for Fluidic Applications

Thesis by
Xing Yang
In Partial Fulfillment of the Requirements
For the Degree of
Doctor of Philosophy

Abstract

The goal of this thesis is to develop high flow rate, low power consumption valves for micromachined fluid handling systems. It has been identified that large actuation deflection and force are the key. In this thesis, several technologies have been developed to achieve large deflection in micromechanical structures.

First, a surface micromachined multi-layer structure, microbellows, has been successfully developed. With polysilicon as the sacrificial layer, the structure of the microbellows has been optimized to achieve large deflection and high strength. It has been shown that the microbellow can deliver more than three times the deflection of a flat membrane of the same size. Thermopneumatic actuators using the microbellows have been demonstrated.

Second, silicone rubber has been explored as the valve membrane material. Several methods for fabricating silicone membranes and integrating them with micromachined components to make actuators and valves have been developed. The silicone has been characterized and has been found to have many desirable properties including high elongation, low modulus, and good sealing. A thermopneumatically actuated valve has been successfully demonstrated.

Third, a normally open, low power thermopneumatic MEMS valve utilizing a composite silicone/Parylene membrane has been developed. A novel suspended silicon nitride membrane heater has been developed to reduce heat loss. By using a "soft" membrane with a large gap and thermopneumatic actuation, high flow rates are achievable while still keeping power consumption low. The steady state and transient response of the thermopneumatic action with various working liquids have been studied. Valves with various constructions have been tested extensively with nitrogen and water flow. As low as 35.5 mW of power is sufficient to control a nitrogen flow of 1.04 lpm with an inlet pressure of 32 psi.

Also, to prevent particles from clogging the microfluidic system, membrane filters (8×8 mm^2) with various shapes of filtering holes have been developed. By varying hole dimensions from 6 to 12 μm, opening factors from 4% to 45% are achieved. A composite silicon nitride/Parylene membrane technology is developed to enhance filter strength. Fluid dynamic performance of the filters has been studied extensively through experiments and numerical simulations.

Table of Contents

List of Figures

List of Tables

Chapter 1

MEMS and Microfluidics

1.1 Background

When the transistor was invented at Bell Labs in 1947, the world took little notice. By the mid-1950's, physicists and electrical engineers recognized the transistor as an alternative to bulky vacuum tubes because the transistor was much simpler, smaller, and consumed less power [1]. Many efforts were made to miniaturize the transistor with the dream of making smaller radios, television sets, and other electronic devices. The scientists soon ran into a difficulty which was called "tyranny of numbers" [1]. The transistor made it theoretically possible to build a powerful computer the size of a wristwatch. Unfortunately, such a computer could not be manufactured because no one had figured out how to connect the vast number of required components. At the time, the best available method for assembling the electronics – soldering a myriad of connections by hand – produced computers that filled entire rooms but had limited capabilities. Computational rates were slowed by the delay of electronic signals traveling through miles of wiring to complete a circuit. Not only was the soldering process expensive, but some electrical connections were inevitably flawed, forcing engineers to design redundant wiring routes that only exacerbated the tyranny of numbers. Then in 1958, Jack Kilby from Texas Instruments and Robert Noyce from Fairchild Semiconductor independently invented a method for integrating all the components for a circuit on the same piece of semiconductor, such as silicon. Integrated Circuits (IC) were born. The tyranny of numbers was broken. Since then, these two processes of **miniaturization and integration** have revolutionized the electronics industry. The growth of IC complexity has followed Moore's Law. As a result, computers that once occupied several rooms have now been replaced by more powerful laptops weighing only a few pounds. These processes have also been applied to moving photons of light on a microchip, giving birth in the last decade to the optoelectronics industry and applications ranging from the CD-ROM to fiber optical telecommunications.

At the end of 1970's and the beginning of 1980's, IC fabrication processes (deposition, etching, lithography, etc.) and materials (silicon, polysilicon, silicon nitride, silicon oxide, aluminum, etc.) were exploited to fabricate mechanical devices, such as beams, pin-joints, cranks, sliders, and gears [2, 3]. This new technology was named "micromachining." It was hoped that by miniaturizing mechanical and electronic devices and integrating them on the same substrate, smaller, smarter microsystems could be made. Since then, new materials, technologies, and devices have been explored. Many devices such as integrated pressure sensors [4], accelerometers [5], and digital mirror displays [6] are now commercially available.

Until now, however, few of these advanced engineering technologies have been applied to the problem of fluid handling. In a typical medical diagnostics laboratory today, most laboratory procedures are cumbersome. Diagnostic processes are labor-intensive and carried out by highly trained personnel. Because of the bulky diagnostic equipment, procedures are often performed at specialized testing sites far from where the resulting information is ultimately used. The chemical and biochemical information is still largely inaccessible on a routine basis. If we follow the same path that the electronics industry has taken, this bottleneck can be and has to be overcome using miniaturization and integration processes. The advancement of micromachining technology makes it possible to produce micro-scale fluid handling devices such as pumps, valves, channels, reservoirs, reactors, extractors, flow manifolds, separation, and detection systems. The miniaturization of these devices will dramatically reduce sample and reagent consumption. This can be particularly advantageous in many situations in which either the quantity of the sample is low, or when any of the required reagents are toxic or expensive. The small volume of sample will also reduce the power consumption, and reduce the analysis time as a result of the short diffusion pathways inside microfluidic systems. The integration of these devices into a microfluidic system will yield several advantages. First, it will significantly reduce the size of existing macro-scale systems or totally replace them. A portable system and on-site, real-time diagnostics will be possible. Second, the diagnostic sequence can be automated, which relaxes the requirement of highly trained personnel and possibly reduces or eliminates human intervention. The chance of sample contamination of the sample and hence false diagnostics will be minimized. Third and most importantly, micro-scale fluid handling together with integrated control will allow the development of new protocols, for example, an entirely new way of accomplishing a given chemical reaction sequence. The protocols made possible by microfabrication can offer many benefits to the end-user, including increased sensitivity/specificity/speed, a broader range of deployment scenarios and entirely new capabilities.

Microfluidic systems will dramatically change the way biological and chemical information is acquired and processed, and will revolutionize biomedical diagnostics. They will also find wide applications in other fields such as health care, environmental monitoring, agriculture, microchip cooling, etc.

1.2 Micro Electro Mechanical Systems (MEMS)

In his legendary paper, “Silicon as a Mechanical Material” [7], K. E. Peterson reviewed the 1970’s micromechanics research achieved by taking advantage of then well-established IC materials and microfabrication technologies. The excellent polysilicon micromechanics work done later at Berkeley, MIT, and other institutions in 1980’s created more interests among researchers all over the world. In late 1980’s, when DARPA started to sponsor research in this field, the name Micro-Electro-Mechanical Systems (MEMS) was used for their programs. Although the name was soon accepted by most US researchers, other names such as micromachining, micro system technology (MST), and micromachines have been used by the rest of the world. So far, there is still no consensus on the name of this field. However, it is acceptable to define MEMS as the fabrication technologies that make it possible to mass-produce small three-dimensional structures with dimensions from subcentimeters to submicrometers. The two main technologies are bulk micromachining and surface micromachining, which are explained in more detail here.

Bulk micromachining In bulk micromachining, three-dimensional mechanical structures are created within the confines of a substrate by selectively removing substrate material. There are many choices for substrate materials and many techniques of material removal. The most popular bulk micromachining technique uses single-crystalline silicon as a substrate and wet chemical etchant to remove unwanted silicon as shown in Figure 1-1. Some chemical solutions such as HNA (hydrofluoric acid, nitric acid, acetic acid) [8] etch silicon isotropically, while other strong alkaline solutions have crystallographic orientation dependent etching characteristics. In the case of anisotropic etching, etching is slowest in the <111> direction, and fastest in the <100> and <110> direction. Some silicon etchants have a reduced etch rate in regions that are heavily doped with boron, adding flexibility in defining the finished structures. Furthermore, an externally applied electrical potential on one side of a p-n junction (electrochemical etching) within the bulk silicon can also be used to influence the etch rate in the direction perpendicular to the junction. The common anisotropic etchants are EDP (ethylenediamine, pyrocatechol, water) [9, 11], KOH (potassium hydroxide, water) [10, 11], and TMAH (tetramethylammonium hydroxide, water) [12]. EDP shows excellent boron etch stop performance with the disadvantage of being very toxic. KOH has the highest <100>/<111> etch selectivity among the three. TMAH is metal-ion-free and hence compatible with IC fabrication, making it suitable for integrated MEMS/IC fabrication. In most cases, silicon oxide and silicon nitride are used as masking films because of their low etch rates in the silicon etchants. Many silicon microstructures, such as cantilevers, beams, diaphragms, channels, and nozzles, have been realized using this technique. In the past few years, some other new techniques have been developed to further increase the capability of bulk micromachining. For example, it was reported that fluorine-containing interholagens, including xenon difluoride (XeF_2) [13] and bromine trifluoride (BrF_3) [14], will etch silicon spontaneously in the vapor phase. The use of this gas phase etching in bulk micromachining has several advantages. It has extremely high etch selectivity over

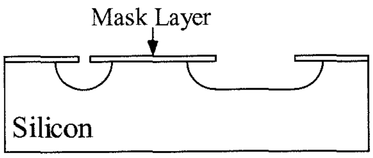

(a) Isotropic Etching

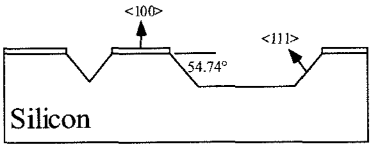

(b) Anisotropic Etching on <100> Silicon Substrate

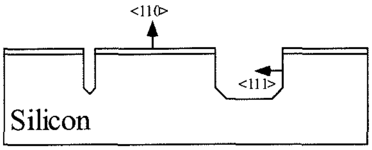

(c) Anisotropic Etching on <110> Silicon Substrate

Figure 1-1 Bulk Micromachining

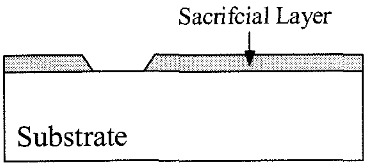

(a) Deposition and Patterning of Sacrificial Layer

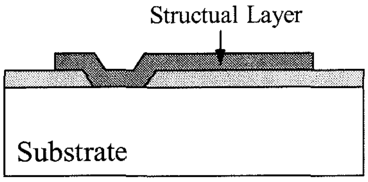

(b) Deposition and Patterning of Structural Layer

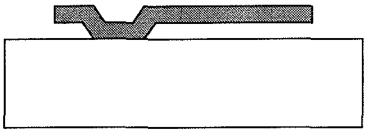

(c) Sacrificial Layer Etching

Figure 1-2 Surface Micromachining

most masking materials (silicon oxide, silicon nitride, and metal), is a room temperature process, and is surface tension free which prevents damage of fragile structures during drying. The other popular technology is deep reactive ion etching (DRIE). With deep RIE, very high aspect ratio structures (>20:1) can be etched into the silicon substrate, and it is not limited by the crystallographic orientation as is the case with wet chemical anisotropic etching.

Surface micromachining The term “surface micromachining” is derived from the fact that structures are built up on the surface of the substrate with layers of thin films. The substrate does not participate in the processing and only provides mechanical support. Because of this, the substrate can be a piece of silicon, glass, alumina, or even metal. The basic concept of surface micromachining is shown in Figure 1-2. It starts with deposition and patterning of a spacer layer (this layer is referred to as a sacrificial layer). The next step is the deposition of a structural layer over the sacrificial layer followed by patterning the structural layer to define the structure. Finally, the sacrificial layer is selectively etched away to free the structure. In 1983, Howe and Muller [15] fabricated micro cantilevers and bridges by using polysilicon surface micromachining technology (LPCVD polysilicon as the structural layer, phosphosilicate glass (PSG) as the sacrificial layer, and hydrofluoric acid (HF) as the selective etchant). The following work at Berkeley in the 1980's demonstrated the broad use of this technology for various devices such as micro pin-joints, sliders [2], resonators [16], grippers [17], and micromotors [18]. In 1991, surface micromachined accelerometers integrated with CMOS circuits were successfully developed and are now commercially available from Analog Devices, Inc. Today, polysilicon micromachining has established itself as one of the most important branches of surface micromachining. In addition to polysilicon surface micromachining, researchers have also explored many other technologies such as silicon nitride/PSG [19] or polysilicon [20, 21], aluminum/polyimide [22], polyimide/aluminum [23], Parylene/photoresist [24], polysilicon/copper [25], etc. Although surface micromachining offers many advantages such as better structure control, complex three-dimensional structure fabrication and possible integration with circuits, there are several issues that have to be addressed before a surface micromachined device can be successfully made. First, the properties (electrical and mechanical) of the amorphous and polycrystalline thin film materials used in surface micromachining depend heavily on the processing conditions. A tight control over the processing parameters is absolutely necessary for device reproducibility. Second, the residual in-plane stress and out-of-plane stress gradient in the thin films may cause warping, buckling or cracking of the structures. Third, the boundary conditions [26] of the structures will significantly affect their mechanical performance. Finally, the wet chemical etching process of releasing the structural elements from the substrate tends to cause the sticking [27] of suspended structures to the substrate. In some cases, cracking or collapse of the structures could happen. Some of these issues and related surface micromachining processes will be discussed more in detail in Chapter 4.

Over these years, many other micromachining technologies have also been developed, such as LIGA [28] (a German acronym for Lithographie, Galvanoformung, Abformung), silicon-silicon fusion bonding [29], silicon-glass anodic bonding [30], 3-D stereolithography [31], micro electrical discharge machining (EDM) [32], laser micromachining [33], plastic injection molding [34], etc.

1.3 Microfluidics Review

Microfluidics is a relatively young field. Most research efforts have been focused on microfluidic components, ranging from fluid sensors, such as pressure, temperature, and flow rate sensors, to fluid actuators, such as mixers, valves, and pumps. In order to fully understand these microfluidic devices, work has been done to study fluid mechanics in micron-size structures. The following is a brief review of the status and achievements of microfluidics research.

1.3.1 Micro Flow Study

Compared to conventional devices, MEMS has a length scale several orders of magnitude smaller. Because of this size reduction, the governing mechanisms might be changed. Many assumptions that we normally take for granted are now questionable. For example, the gas flow might not be considered as continuum flow when the length scale is on the order of the gas mean free path. As a result of this, the common fluid mechanical assumption that says the flow velocity at the wall is zero (no-slip boundary condition) might not be valid anymore. J. Pfahler *et al.* [35] studied fluid flow in bulk micromachined channels. The flow rate and pressure drop across the inlet and outlet of the microchannels were measured. The channels had a trapezoidal cross section and depths ranging from 0.5 μm to 50 μm. It was found that the friction or the apparent viscosity is consistently smaller than that predicted by conventional incompressible theory. E. Arkilic *et al.* [36] reported that the flow in microchannels cannot be modeled using Navier-Stokes equations with a no-slip boundary condition. They repeated J. Pfahler's pressure drop *vs.* flow rate experiments with a more delicate setup. It was found that Navier-Stokes equations with a modified slip boundary condition fit the experimental results. The Caltech/UCLA group has also done extensive study on this subject. J. Liu *et al.* [37] developed a surface micromachined flow system in which pressure sensors were integrated along microchannels with dimensions of 4000 μm × 40 μm × 1.2 μm. The goal was to not only measure the pressure drop across the inlet and outlet, but also the pressure distribution along the whole length of the channel. It was found, for the first time, that the pressure distribution is not a linear function of the streamwise distance. The compressibility effect becomes very important and the viscous dissipation is extremely high. They also found that modification of the no-slip boundary condition is necessary to model the fluid flow in the microchannels. S. Wu *et al.* [38] studied the temperature distribution along surface micromachined channels. The channels had dimensions of 4400 μm × 20 μm × 2 μm. In order to improve thermal isolation, microchannels with integrated temperature sensors were suspended from substrate. The temperature measurements suggested a friction effect along the microchannels. More work needs to be done to integrate both temperature and pressure sensors along the microchannels.

1.3.2 Fluid Sensors

Pressure measurement is an indispensable part of fluid study and control. Ever since C. S. Smith discovered the piezoresistance effect in germanium and silicon, many micromachined pressure sensors have been developed. Today, pressure sensors with integrated conditioning circuits are commercially available from many companies such as Lucas NovaSensor®, Motorola, etc. The two most common working principles are piezoresistive sensing and capacitive sensing. For piezoresistive sensing, it was found the piezoresistance coefficient of silicon is much higher than the ones of metal. Piezoresistive pressure sensors have very linear response and their processing is more IC compatible compared to capacitive pressure sensors. However, temperature influence is a major concern for piezoresistive pressure sensors because of the non-zero temperature sensitivity of the piezoresistance coefficient. The temperature effect can be decreased using the Wheatstone-bridge configuration. Generally speaking, capacitive pressure sensors are more sensitive than piezoresistive pressure sensors. Other advantages include relatively simple construction and low inherent temperature coefficient. However, capacitive pressure sensors suffer from nonlinear response because of the nonlinear relationship between capacitance and the electrode gap distance.

In a microfluidic system, if pressure plays the role of "voltage," then flow rate is "current." Most of today's flow sensors are based on the thermal principle. When a heated element is placed in a flow field, the fluid flow on the surface will take the heat away by forced convection and change the heated element temperature. By measuring this temperature change, the flow rate on the surface can be obtained. Y. C. Tai *et al.* [39] and follow-up work by F. Jiang *et al.* [40] reported surface micromachined polysilicon bridge anemometers. Lightly doped polysilicon was used as the thermal sensing element because of its high temperature coefficient of resistivity (TCR). Other sensing elements such as platinum resistors, silicon diffused resistors, or even bipolar transistors were also explored. The performance of these sensors depends not only on the sensing element, but also on the thermal isolation of sensor structure. With good thermal isolation, the heat loss through the substrate is significantly reduced. This helps increase the sensitivity and reduce power consumption. The frequency response is also improved due to smaller thermal mass. To achieve good thermal isolation, many micromachined structures such as cantilever beams, freestanding bridges and plates, and vacuum-sealed cavities [41] have been developed.

1.3.3 Fluid Actuators

Mixing is a fundamental process in chemical and biological analysis. The mixing process proceeds as follows. When two parts of different liquids are placed in contact, the molecules from both parts start to diffuse into each other. Homogeneous mixing is achieved when the diffusion process is finished. It is clear that diffusion is the speed-limiting step in the mixing process. The solution to fast mixing is to increase the contact area which will shorten the diffusion length. In a turbulent flow field, this is done by the unsteady turbulence. In a system with laminar flow, this is usually achieved by agitation. Miyake *et al.* [42] reported a micro-mixer that operates in the laminar flow regime. Two different liquids were forced through an array of 400 bulk micromachined nozzles (15 μm × 15 μm) to form many micro-plumes. These plumes increased the contact area drastically. Mixing time on the order of 1 second was achieved in their mixer. Branebjerg *et al.* [43] developed a mixer based on the same concept. The increase of contact area was achieved by multi-stage, multi-layer lamination of two liquids. Mixing times of 100 – 300 ms were reported. A. Desai *et al.* [44] developed a bulk micromachined high Reynolds number (2000 – 6000) flow mixer to study chemical reaction kinetics. More than one mixer was integrated on one chip so that initiating and quenching (starting and stopping) chemical reactions in intervals as short as 100 μs were achieved.

To prevent clogging of microfluidic system, filtration is necessary. C. J. M. van Rijin *et al.* [45] reported silicon nitride membrane filters. Low stress silicon nitride membranes (1 mm × 1 mm × 1 μm) with perforations of 4.5 μm in diameter were fabricated, but fluid dynamic performance of the filters was not studied. In such a filter, the size of the perforation holes determined the filtration threshold, i.e., the minimum size of the particles that were blocked. This could be a problem in the case of very small particle filtration because the hole size is limited by the photolithography and etching processes. By using surface micromachining technology, G. Kittilsland *et al.* [46] developed a sub-micron particle filter in which filtration took place through the gap defined by the sacrificial layer. It was shown that filtration down to 50 nm was achieved.

As the basic fluid control device, the valve plays the role of the "transistor" in fluidic circuits. Over these years, different micromachined valves have been developed. M. Zdeblick [47] conceived a thermopneumatically actuated valve while he was a graduate student at Stanford. Later, he founded the company, Redwood Microsystems, to further explore this technology. Basically, the valve worked like an electrically-heated, closed-cycle steam engine. Liquid was trapped in a sealed cavity which had a thin silicon membrane on one side and a resistive heater on the other side. When the liquid was heated up, the liquid expanded and/or evaporated causing an increase of the pressure in the cavity. As a result, the silicon membrane deflected outward to open/close the flow. It was demonstrated that thermopneumatic actuation can generate very large force (~1 N) over a large displacement (~ 50 μm). Because of this, high pressure load and high flow rate were achieved in their valve. However, the valve had a slow response (~ 1 second) inherent with thermopneumatic actuation and large power consumption (~ 1 W) due to large thermal mass. P. Barth [48] from Hewlett Packard Laboratories and H. Jerman [49] from EG & G IC Sensors developed bimetallic actuated valves. In both cases, the valve membrane was made of two materials that had different coefficients of thermal expansion. When the temperature changed, the membrane displaced as the result of thermal expansion. P. Barth used nickel/silicon as the bimetallic pair for their valve, while H. Jerman used aluminum/silicon. The group led by D. Johnson in The TiNi Alloy Company and Microflow, Inc., [50] developed a valve based on shape memory alloy (SMA) actuation. Shape memory alloy is a mixture of nickel and titanium which has a plastically-deformable martensite crystal structure at low temperature, but undergoes a phase transition to a stiff austenite structure at a higher transition temperature. The material "remembers" its original shape in the high-temperature phase and above the transition temperature, it returns to that remembered shape and generates considerable force in the process. The SMA valve delivered very good performance (100 psi pressure load, 8 liter/min flow rate and 0.3 W power), but the processing of SMA and integrating it with conventional micromachining fabrication was challenging.

Pump is another important device for microfluidic systems. Its main function is to provide the driving force for the fluid flow. Although many types of micromachined pumps, such as gear pump, ion drag pump, bubble pump, acoustic wave driven pump, etc., have been developed, the membrane pump is still the most popular one.

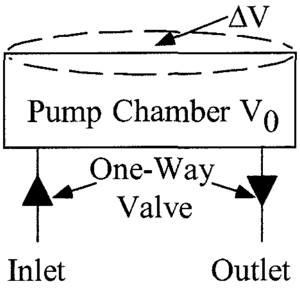

Figure 1-3 Schematic of a Membrane Pump

Typically, a membrane pump has a pump chamber and two one-way check valves as shown in Figure 1-3. It works in cycles. In the first half of the cycle, when the membrane moves upwards and the pump chamber expands, an under-pressure is generated in the pump chamber and fluids can only flow into the pump chamber through the inlet. This operation mode is called supply mode. In the next half of the cycle, the pump volume decreases and an over-pressure is generated in the pump chamber. Since the valves are one-way, the fluid can only flow out of the chamber through the outlet. This concludes the pumping cycle. A micromachined pump unavoidably has a dead volume, V_0, and a volume change due to membrane actuation defined as ΔV, then the compression ratio ε can be defined as

$$\varepsilon = \frac{\Delta V}{V_0} . \qquad (1\text{-}1)$$

Usually, ε is very small. During the pumping cycle, when the pump membrane moves, it generates a pressure difference, ΔP, between inside and outside the pump chamber. This pressure difference ΔP depends on the compression ratio ε and the compressibility of the fluids. The higher ε, the higher ΔP. The higher the compressibility, the lower ΔP. In order for the pump to work, ΔP has to be larger than certain pressure threshold, ΔP_{th}, which is the pressure difference to switch the check valve, i.e., the operation condition is

$$|\Delta P| \geq |\Delta P_{th}| . \qquad (1\text{–}2)$$

Generally speaking, a liquid pump is relatively easy to make. The reason is that even though the compression ratio ε is small, condition (1-2) can be still met because most liquids are incompressible. However, in the case of gas pumps or liquid pumps that have gas bubbles, the nontrivial compressibility of gas in the pump chamber significantly decreases the pressure difference ΔP. When ΔP becomes too small and the condition (1-2) is not satisfied, the pump will not work. In the case of self-priming pump, the right-hand side of condition (1-2) is changed. ΔP_{th} is increased because now the pump has to overcome not only the check valve threshold pressure, but also the meniscus force to suck the liquid into the pump chamber. We can conclude from above that a high compression ratio ε is the key to a successful pump. This can be achieved by increasing the pumping volume, ΔV, and/or decreasing dead volume, V_0. Large stroke and large force actuation mechanisms such as piezoelectric or thermopneumatic actuation have been tried to increase ΔV. Careful pump structure design could decrease the dead volume. Besides the one-way check valve design, there are other designs such as diffuser/nozzle [51] or even valveless peristaltic pump [52] in which three membranes deflect in such a sequence that the fluid is squeezed towards one direction and not the other.

1.4 Goal and Organization of Thesis

The goal of the work described in this thesis is to develop microfluidic devices for chip scale fluid handling. These devices should have high performance, low power consumption, and should be easily integrated into a system. The direct application is a project funded by DARPA to develop a handheld system for airborne virus and toxin detection in chemical/biological warfare environments.

The rest of the thesis is organized as follows. In Chapter 2, the design, fabrication, and testing of particle membrane filters are presented. Review of several actuation mechanisms for valve applications are studied in Chapter 3. It is concluded that thermopneumatic actuation can provide large force and large deflection. The disadvantage of the common flat silicon membranes is then described and a new microbellows structure and flexible membrane technology are introduced. Before details of various generations of valves are presented, surface micromachined membranes including their cracking, boundary conditions, and a new polysilicon sacrificial technology to make them are studied in Chapter 4. Chapter 5 describes the design, fabrication, and testing of the microbellows. Testing shows that they are very suitable for valve and pump applications. A new silicone rubber membrane technology is shown in Chapter 6. Thermopneumatic valves using the silicone rubber membrane are fabricated and tested. Although good performance is achieved, most of the working liquid in the actuation cavity leaks through the silicone rubber membrane in a matter of days. A new Parylene membrane technology is developed in Chapter 7 to solve this problem. A composite membrane combining both silicone rubber and Parylene is described in Chapter 8. A new valve using this technology is designed, fabricated, and tested. A new silicon nitride membrane heater is developed to reduce the power consumption. The frequency response and flow study of the valve is presented. Finally, the thesis concludes with a summary and suggests future work.

Bibliography

[1] *Scientific American*, Special Issue on the Solid-State Century, 1997.

[2] L. S. Fan, Y. C. Tai, and R. S. Muller, "Integrated Movable Micromechanical Structures for Sensors and Actuators," IEEE Transactions on Electron Devices, Vol. ED-35 (6), pp. 724-730, June 1988.

[3] M. Mehregany, K. J. Gabriel, and W. S. N. Trimmer, "Integrated Fabrication of Polysilicon Mechanisms," IEEE Transactions on Electron Devices, Vol. ED-35 (6), pp. 719-723, June 1988.

[4] Lucas NovaSensor®, http://www.novasensor.com.

[5] Analog Devices, Inc., http://www.analog.com.

[6] Texas Instruments, Inc., http://www.ti.com/dlp.

[7] K. E. Peterson, "Silicon as a Mechanical Material," Proceedings of IEEE, Vol. 70 (5), pp. 420-457, May 1982.

[8] H. Robbins and B. Schwartz, "Chemical Etching of Silicon, II. The System HF, HNO_3, H_2O and $HC_2H_3O_2$," Journal of Electrochemical Society, Vol. 107, pp. 108-111, 1960.

[9] A. Reisman, M. Berkenblit, S.A. Chan, F.B. Kaufman, and D.C. Green, "The Controlled Etching of Silicon in Catalyzed Ethylenediamine-Pyrocatechol-Water Solutions," Journal of Electrochemical Society, Vol. 126 (8), pp. 1406-1415, 1979.

[10] D. L. Kendall and G. R. de Guel, "Orientations of the Third Kind: the Coming of Age of (110) Silicon," Micromachining and Micropackaging of Transducers, Elsevier Science Publishers B. V., Amsterdam, 1985.

[11] H. Seidel, "The Mechanism of Anisotropic Silicon Etching and its Relevance for Micromachining," Technical Digest, International Conference on Solid-State Sensors and Actuators (Transducers'87), pp. 120-125, Tokyo, Japan, June 1987.

[12] O. Tabata, R. Asahi, H. Funabashi, K. Shimaoka, and S. Sugiyama, "Anisotropic Etching of Silicon in TMAH Solutions," Sensors and Actuators (A: Physical), Vol. 34, pp. 51-57, 1992.

[13] P. B. Chu, J. T. Chen, R. Yeh, G. Lin, J. C. P. Huang, B. A. Warneke, and K. S. J. Pister, "Controlled Pulsed Etching with Xenon Difluoride," Technical Digest, International Conference on Solid-State Sensors and Actuators (Transducers'97), Vol. 1, pp. 665-668, Chicago, USA, June 1997.

[14] X. Q. Wang, X. Yang, K. Walsh, and Y.C. Tai, "Gas Phase Silicon Etching with Bromine Trifluoride," Technical Digest, International Conference on Solid-State Sensors and Actuators (Transducers'97), Vol. 2, pp. 1046-1415, Chicago, USA, June 1997.

[15] R. T. Howe and R. S. Muller, "Polycrystalline Silicon Micromechanical Beams," Journal of Electrochemical Society, Vol. 130, pp.1420-1423, 1983.

[16] W. C. Tang, T.-C. H. Nguyen, and R. T. Howe, "Laterally Driven Polysilicon Resonant Microstructures," Proceedings of IEEE Workshop on Micro Electro Mechanical Systems (MEMS'89), pp. 53-59, Salt Lake City, USA, February 1989.

[17] C. J. Kim, A. P. Pisano, R. S. Muller, and M. G. Lim, "Polysilicon Microgripper," Technical Digest, IEEE Solid-State Sensors and Actuators Workshop, pp. 48-51, Hilton Head Island, South Carolina, USA, June 1990.

[18] Y. C. Tai, *IC-Processed Polysilicon Micromechanics: Technology, Materials and Devices*, Ph.D. Thesis, University of California, Berkeley, 1989.

[19] J. Q. Liu, Y. C. Tai, J. Lee, K. C. Pong, Y. Zohar, and C. M. Ho, "*In Situ* Monitoring and Universal Modeling of Sacrificial PSG Etching Using Hydrofluoric Acid," Proceedings of IEEE Workshop on Micro Electro Mechanical Systems (MEMS '93), pp. 71-76, Fort Lauderdale, USA, February 1993.

[20] S. Sugiyama, T. Suzuki, K. Kawahata, K. Shimaoka, M. Takigawa, and I. Igarashi, "Micro-Diaphragm Pressure Sensor," Proceedings of IEEE International Electron Devices Meeting, pp. 184-187, Los Angeles, USA, December 1986.

[21] O. Tabata, H. Funabashi, K. Shimaoka, R. Asahi, and S. Sugiyama, "Surface Micromachining Using Polysilicon Sacrificial Layer," Proceedings of International Symposium on Micromachine and Human Science, pp.163-172, Nagoya, Japan, October 1991.

[22] C. Storment, D. Borkholder, V. Westerlind, J. Suh, N. Maluf, and G. Kovacs, "Dry-Released Process for Aluminum Electrostatic Actuators," Technical Digest, Solid-state Sensor and Actuator Workshop, pp. 95-98, Hilton Head Island, South Carolina, USA, June 1994.

[23] M. A. Schmidt, R.T. Howe, S.D. Senturia, and J.H. Haritonidis, "Design and Calibration of a Microfabricated Floating-Element Shear-Stress Sensor," IEEE Transactions on Electron Devices, Vol. ED-35 (6), pp. 750-757, June 1988.

[24] P. Man, D. Jones, and C. Mastrangelo, "Microfluidic Plastic Capillaries on Silicon Substrates: A New Inexpensive Technology for Bio Analysis Chips," Proceedings of IEEE Workshop on Micro Electro Mechanical Systems Workshop (MEMS '97), pp. 311-316, Nagoya, Japan, January 1997.

[25] T. R. Tsao, T. Y. Hsu, and Y. C. Tai, "Copper Sacrificial Layer Technology for Use in Surface Micromachining," Micromachining Workshop III, Southern California Chapter of American Vacuum Society, Anaheim, CA, September 1996.

[26] X. Yang, F. M. Siu, and Y. C. Tai, "Strength of Surface Micromachined Diaphragms," MRS Spring Meeting, Symposium N: Microelectromechanical Structures for Material Research, San Francisco, CA, April 1998.

[27] C. H. Mastrangelo and C. H. Hsu, "Mechanical Stability and Adhesion of Microstructures under Capillary Forces – Part I, II," Journal of Microelectromechanical Systems, Vol. 2, pp. 30-55, 1993.

[28] A. Rogner, W. Ehrfeld, D. Münchmeyer, P. Bley, C. Burbaum, and J. Mohr, "LIGA-Based Flexible Microstructures for Fiber-Chip Coupling," Journal of Micromechanics and Microengineering, Vol. 1 (3), pp. 167-170, 1991.

[29] K. Peterson, P. Barth, J. Poydock, J. Brown, J. Mallon Jr., and J. Bryzek, "Silicon Fusion Bonding for Pressure Sensors," Technical Digest, IEEE Solid-State-Sensors and Actuators Workshop, pp. 144-147, Hilton Head Island, South Carolina, USA, June 1988.

[30] W. H. Ko, J. T. Suminto, and G. J. Yeh, "Bonding Techniques for Microsensors," Micromachining and Micropackaging of Transducers, Elsevier Science Publishers B. V., Amsterdam, 1985.

[31] K. Ikuta and K. Hirowatari, "Real Three-Dimensional Micro Fabrication Using Stereo Lithography and Metal Molding," Proceedings of IEEE Workshop on Micro Electro Mechanical Systems Workshop (MEMS '93), pp. 42-47, Fort Lauderdale, USA, February 1993.

[32] T. Masaki, K. Kawata, and T. Masuzawa, "Micro Electro-Discharge Machining and Its Applications," Proceedings of IEEE Workshop on Micro Electro Mechanical Systems (MEMS'90), pp. 21-26, Napa Valley, USA, February 1990.

[33] D. J. Elliott, *Ultraviolet Laser Technology and Applications*, Academic Press, San Diego, CA, 1995.

[34] R. C. Anderson, G. J. Bogdan, and R. J. Lipshutz, "Miniaturized Genetic-Analysis System," Technical Digest, Solid-State-Sensors and Actuators Workshop, pp. 258-261, Hilton Head Island, South Carolina, USA, June 1996.

[35] J. Pfahler, J. Harley, and H. Bau, "Gas and Liquid Flow in Small Channels," Micromechanical Sensors, Actuators, and Systems, Vol. 32, pp. 49-60, ASME, 1991.

[36] E. B. Arkilic, M. A. Schmidt, and K. S. Breuer, "Gaseous Slip-Flow in Long Microchannels," Journal of Microelectromechanical Systems, Vol. 6 (2), pp.167-178, 1997.

[37] J. Q. Liu, *Integrated Micro Devices for Small Scale Gaseous Flow Study*, Ph.D. Thesis, California Institute of Technology, 1995.

[38] S. Wu, J. Mai, Y. Zohar, Y.C. Tai, and C.M. Ho, "A Suspended Microchannel with Integrated Temperature Sensors for High Pressure Flow Studies," Proceedings of International Workshop on Micro Electro Mechanical Systems (MEMS '98), pp. 87-92, Heidelberg, Germany, January 1998.

[39] Y. C. Tai and R. S. Muller, “Lightly Doped Polysilicon Bridge as an Anemometer,” Technical Digest, International Conference on Solid-State Sensors and Actuators (Transducers’87), pp. 360-363, Tokyo, Japan, June 1987.

[40] F. Jiang, Y. C. Tai, W. Li, C. M. Ho, and W. J. Li, “A Micromachined Polysilicon Hot-Wire Anemometer,” Technical Digest, Solid-State Sensor and Actuator Workshop, pp. 264-267, Hilton Head Island, South Carolina, USA, June 1994.

[41] C. Liu, Y. C. Tai, J. B. Huang, and C. M. Ho, "Surface Micromachined Thermal Shear Stress Sensor," Application of Microfabrication to Fluid Mechanics, ASME International Mechanical Engineering Congress and Exposition, pp. 9-15, Chicago, USA, November 1994.

[42] R. Miyake, T.S. Lammerink, M. Elwenspoek, and J. Fluitman, “Micro Mixer with Fast Diffusion,” Proceedings of IEEE Workshop on Micro Electro Mechanical Systems Workshop (MEMS '93), pp. 248-253, Fort Lauderdale, USA, February 1993.

[43] J. Branebjerg, P. Gravesen, J. P. Krogand, and C. R. Nielsen, “Fast Mixing by Lamination,” Proceedings of International Workshop on Micro Electro Mechanical Systems (MEMS '96), pp. 441-446, San Diego, USA, February 1996.

[44] A. Desai, D. Bokenkamp, X. Yang, Y. C. Tai, E. Marzluff, and S. Mayo, "Microfluidic Sub-millisecond Mixers for the Study of Chemical Reaction Kinetics," Technical Digest, International Conference on Solid-State Sensors and Actuators (Transducers '97), Vol. 1, pp. 167-170, Chicago, USA, June 1997.

[45] C. J. M. van Rijin and M. C. Elwenspoek, “Micro Filtration Membrane Sieve with Silicon Micro Machining for Industrial and Biomedical Applications,” Proceedings of IEEE Workshop on Micro Electro Mechanical Systems (MEMS’95), pp. 83-87, Amsterdam, The Netherlands, January 1995.

[46] G. Kittilsland, G. Stemme, and B. Norden, “A Sub-Micron Particle Filter in Silicon,” Sensors and Actuators (A: Physical), Vol. 23, pp. 904-907, 1990.

[47] M. J. Zdeblick, *A Planar Process for an Electric-to-Fluidic Valve*, Ph.D. Thesis, Stanford University, 1988.

[48] P. Barth, C. C. Beatty, L. A. Field, J. W. Baker, and G. B. Gordon, "A Robust Normally Closed Silicon Microvalve," Technical Digest, Solid-State Sensor and Actuator Workshop, pp. 248-250, Hilton Head Island, South Carolina, USA, June 1994.

[49] H. Jerman, "Electrically-Activated, Micromachined Diaphragm Valve," Technical Digest, IEEE Solid-State Sensor and Actuator Workshop, pp. 65-69, Hilton Head Island, South Carolina, USA, June 1990.

[50] J. D. Busch and A. D. Johnson, "Prototype Microvalve Actuator," Proceedings of IEEE Workshop on Micro Electro Mechanical Systems (MEMS'90), pp. 40-41, Napa Valley, USA, February 1990.

[51] A. Olsson, P. Enoksson, G. Stemme, and E. Stemme, "Micromachined Flat-Walled Valveless Diffuser Pumps," Journal of Microelectromechanical Systems, Vol. 6 (2), pp.161-166, 1997.

[52] Charles Grosjean, personal communications, 1997.

Chapter 2

Membrane Filters

2.1 Introduction

Unavoidably, particles can get into a microfluidic system and cause many problems. For example, they can partially clog up the flow channels and affect the flow rate. In a valve, if particles get stuck on the valve seat, they can cause leaks when the valve is supposed to be closed. The same situation can happen in the check-valves of a pump. The leak can cause back flow and reduce the pump rate. To prevent this, filters should be used to keep the particles outside the microfluidic system. In some other applications such as airborne particle sampling, not only filtration but also collection of the particles is needed. Here, we target airborne particles in the range of 1 to 10 μm [1], and micromachined membranes with perforations are ideal candidates for filtering such particles. For MEMS membrane filters to be effective, various requirements must be met. They must be mechanically robust so as to stand a potentially high pressure drop. The filter opening factor (β = area of holes/total area) must be high to allow for a large amount of air flow. Finally, the pressure drop, and hence the power loss, has to be low. A lot of factors including hole dimension, shape, membrane thickness, and the opening area factor affect the performance of the filters. Large holes and a large opening factor will decrease the pressure drop and increase the flow rate, but decrease the strength of the membrane. Different hole shapes will not only change the flow rate and pressure drop, but also the stress concentration level in the membrane, and thus the strength of the filter as well.

C. J. M. van Rijin *et al.* [2, 3] developed silicon nitride membrane filters. As shown in Figure 2-1, 1 μm thick LPCVD low stress silicon nitride membranes are fabricated. The membranes have maximum size of 1 mm × 1 mm and perforations of 4 μm. No detailed information on fluid dynamic performance of the filters was given. In such a filter, the size of the perforation holes determined the filtration threshold, i.e., the minimum size of the particles that were blocked. This could be a problem in the case of very small particle filtration because the hole size is limited by the photolithography and etching process. By using surface micromachining technology, G. Kittilsland *et al.* [4] developed a sub-micron particle filter shown in Figure 2-2. In this filter, filtration takes place through the gap defined by the sacrificial layer. They reported that filtration down to 50 nm is achieved.

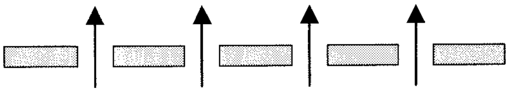

Figure 2-1 Silicon Nitride Membrane Filter (From [2])

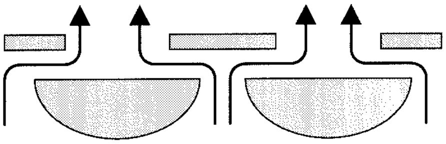

Figure 2-2 Sub-micron Particle Filter (From [4])

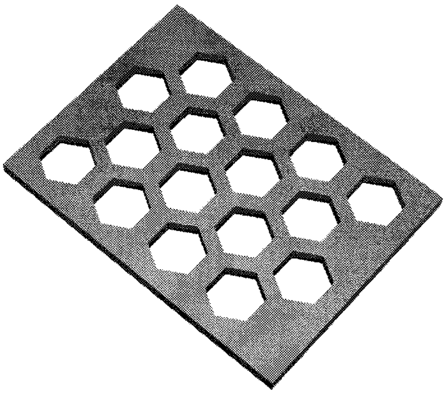

Figure 2-3 Our Approach

As shown in Figure 2-3, the basic structure of our filter is similar to what was described in [2, 3]. However, our goal is to develop high performance membrane filters (high flow rate, low pressure drop, high strength, and low power consumption) by using novel materials/structures and fabrication processes. Also, we would like to study the fluid dynamic performance of the filters experimentally and numerically, and establish a guideline for optimal membrane filter design.

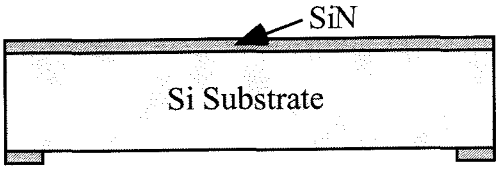

(a) SiN Deposition and Backside Patterning

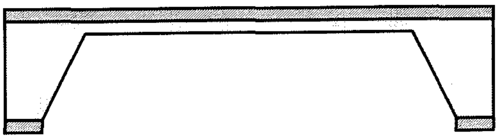

(b) KOH Etching

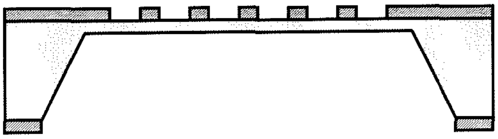

(c) Frontside SiN Patterning

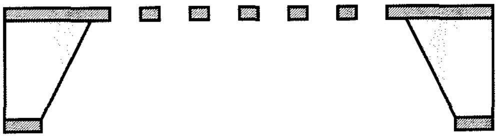

(d) Si Etching

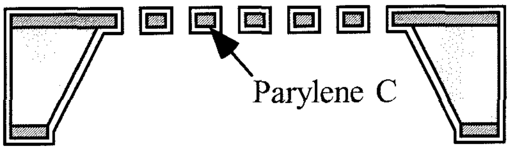

(e) Parylene C Deposition

Figure 2-4 Membrane Filter Fabrication Process

2.2 Fabrication

The filters were fabricated by using the process shown in Figure 2-4. First, a layer of 1 μm thick LPCVD silicon nitride (SiN) was deposited at 850 °C with a SiH_2Cl_2/NH_3 gas flow ratio of 4/1 to achieve low stress [5]. Windows on the back side of the wafers were opened using SF_6/O_2 plasma etching. The wafers were then etched in potassium hydroxide (KOH) until only 20 μm silicon was left. Next, an array of filtering holes was etched into the silicon nitride layer on the front side of the wafer using SF_6/O_2 reactive ion etching (RIE). Then the wafers were diced and etched in KOH again to remove the remaining silicon and free the membrane. By dicing the wafers before the membranes are freed, the possibility of damaging the fragile membranes during the dicing was avoided. Finally, a layer of Parylene C polymer was deposited conformally over the wafers or individual dies. This layer of Parylene is very important and serves two purposes. First, we found that the simple silicon nitride membrane filters are very fragile. By coating the silicon nitride membrane with a layer of Parylene, the strength of the membrane filters is significantly improved. Second, since the Parylene deposition is conformal, different hole sizes can be obtained from the same base filter by varying the thickness of the Parylene layer. Parylene will be discussed in more detail in Chapter 7.

2.3 Design

Using the fabrication process described above, several membrane filters as large as 8 × 8 mm^2 have been made. The membrane filters are perforated with holes of varying shapes such as circles, rectangles, and hexagons. As shown in Table 2-1, the opening factor of the filters is in the range of 4 to 45% with different hole sizes and pitches. As shown later in the testing section, the pressure drop and the power requirement of the filters to sustain a desired flow rate strongly depend on the opening factor. A high opening factor is necessary to achieve low pressure drop and high flow rate in the filters, and the opening factor increases as the hole size increases. However, the maximum hole size is determined by the target particle size. Thus, there is a tradeoff between opening factor and hole size. Typical filter parameters are, for example, 10.6 μm diameter circular holes with an opening factor of 13%. Hexagonal holes offer a higher opening factor than circular holes, but their geometry results in greater stress concentration in the membrane, which decreases the strength of the filters. Rectangular holes can give a large range of opening factors without changing the filtering threshold as long as one dimension of the rectangular holes is kept constant. But they suffer from the same stress concentration problem as hexagonal holes. Figure 2-5 shows photographs of the fabricated filters with circular (a), rectangular (b), and hexagonal holes (c, d).

Table 2-1 Membrane Filter Design

Filter	Top View (8 mm x 8 mm) ▨ : Non-Filtering Area ☐ : Filtering Area	Cross-sectional View ▨ : Silicon Nitride ☐ : Parylene Coating	Hole Size d (µm) or a × b (µm^2)	Opening Factor β (%)	Hole Shape
1	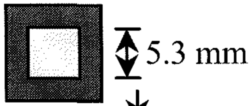	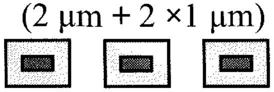	6	4	Circular
2	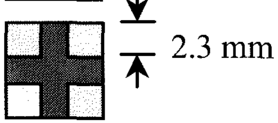		8 ~ 8.8	8	Circular
3	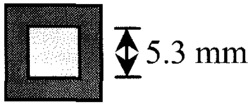		10.6	13	Circular
4	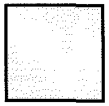	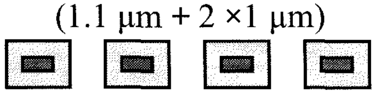	8	20	Hexagonal
5	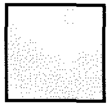	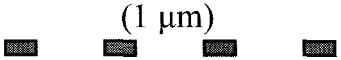	12	45	Hexagonal
6	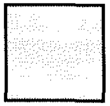	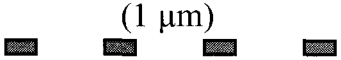	6 × 20	39	Rectangular
7	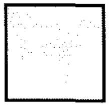	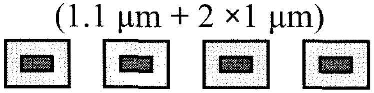	3 × 18	21	Rectangular

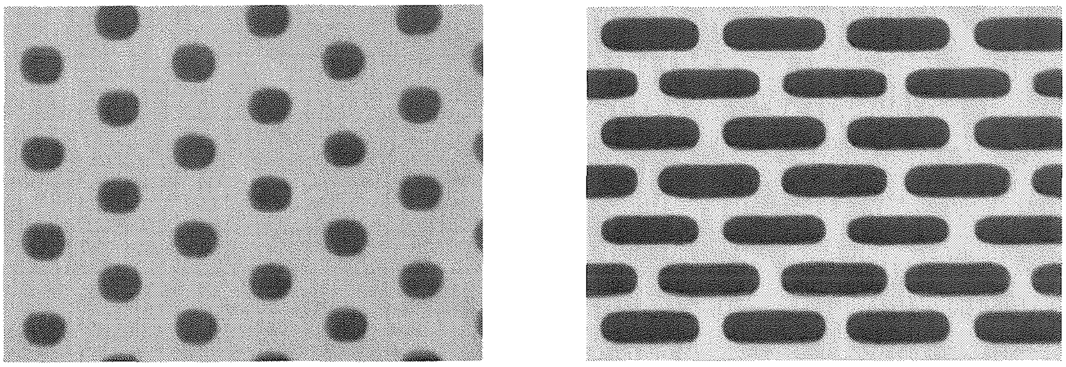

(a) Circular (b) Rectangular

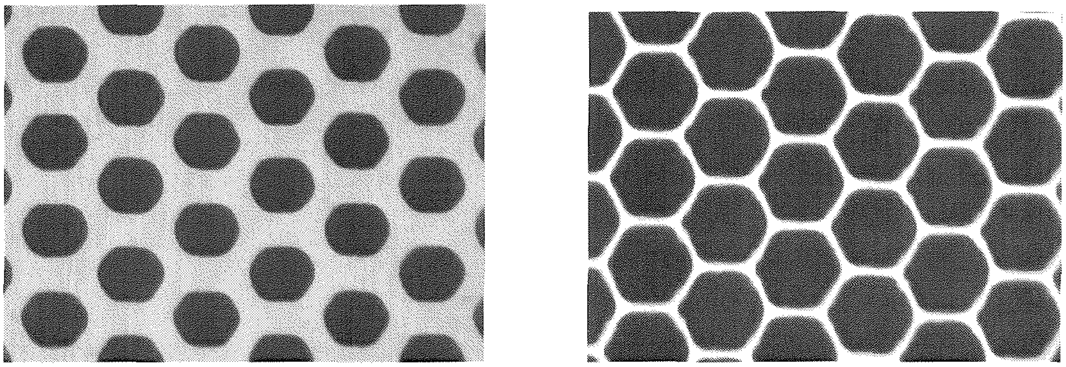

(c) Hexagonal (d) Hexagonal

Figure 2-5 Fabricated Membrane Filters

2.4 Strength

The membrane filters were found to be very fragile. During the experiments, they took very little pressure load. Also, they had to be handled very carefully. Otherwise, they broke very easily. Figure 2-6 shows a good membrane filter (a) and a broken one (b).

The strength of the membrane filters is studied and compared to that of flat silicon nitride membranes with identical dimensions but without perforations. High pressure air flow is passed through the filters. By increasing the flow until the filter breaks, the "burst pressure" is then determined as the differential pressure at burst. For example, an 8 mm × 8 mm × 1 μm membrane bursts at 5.5 psi while Filter 6 (Figure 2-7 (b)) in Table 2-1 bursts at 0.9 psi. Filter 6 has a lower burst pressure due to the stress concentration in the membrane caused by the perforations. As mentioned in 2.2, in order to improve the burst

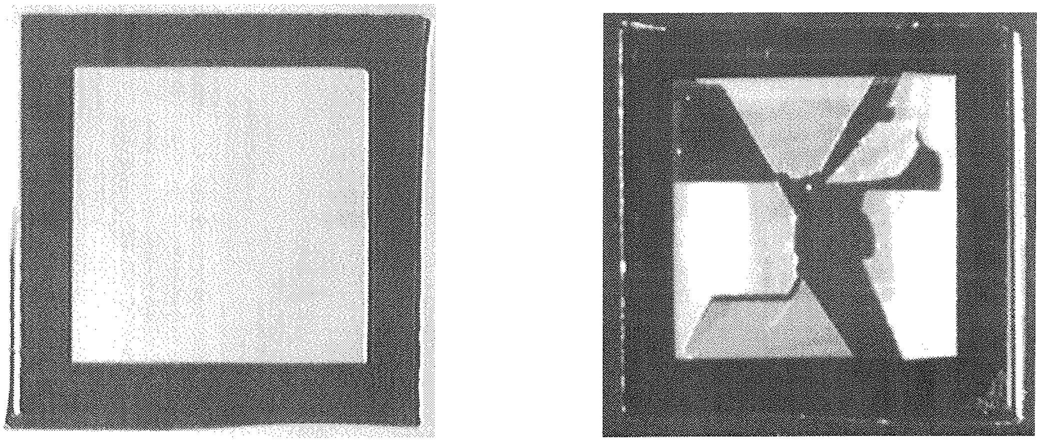

(a) Good (b) Broken

Figure 2-6 Pictures of Good and Broken Membrane Filter Dies (8 mm × 8 mm)

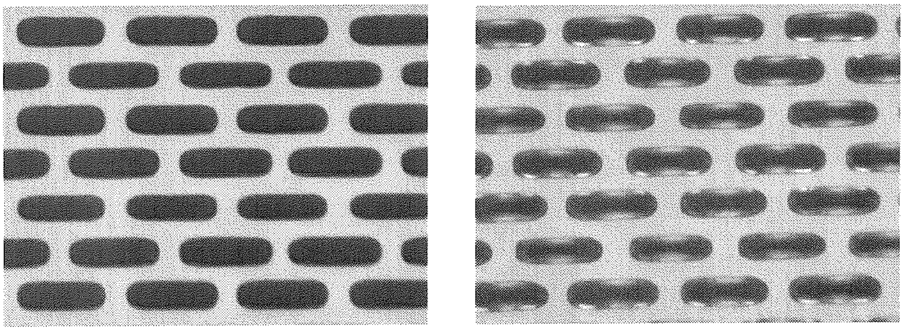

(a) Filters with Rectangular Holes Before and After Parylene Coating

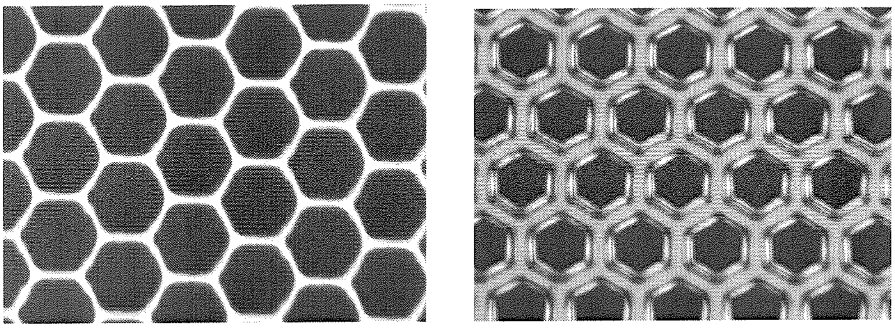

(b) Filters with Hexagonal Holes Before and After Parylene Coating

Figure 2-7 Parylene Coating on Membrane Filter

pressure, a layer of Parylene C is conformally deposited on the filters. Figure 2-7 (a) is a picture of a Filter 6 coated with 1.38 μm of Parylene. The shadows around every hole clearly show the conformal nature of the Parylene deposition. Table 2-2 shows that the thicker the membrane, the higher the burst pressure. With 2.69 μm thick Parylene

Table 2-2 Filter Strength
(Filter 6, $\beta = 39\ \%$)

Parylene Thickess (μm)	Burst Pressure (PSI)
0	0.9
1.38	1.9
2.69	4.2

deposition, the burst pressure of Filter 6 is increased to 4.2 psi which is more than four times that of an uncoated one and is comparable to that of an unperforated membrane.

2.5 Fluid Dynamic Testing

To test the fluid dynamic performance, a small wind tunnel shown in Figure 2-8 is designed and built. The wind tunnel consists of inlet, settling chamber, contraction, testing chamber, diffuser, and suction fan. A prefilter is inserted at the inlet of the wind tunnel to prevent particles in the air from clogging the filter under test. The contraction section is carefully designed so that a uniform mean flow in the test section can be

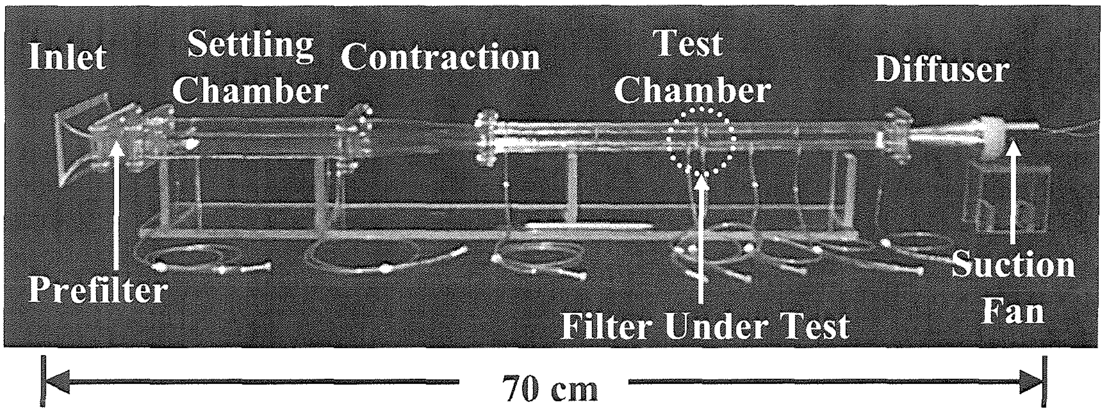

Figure 2-8 Wind Tunnel for Membrane Filter Fluid Dynamic Performance Testing

achieved and there is no separation of the flow at the inlet of the test section. Several different commercially available suction fans (computer fan, hair dryer fan, etc.) are used to provide flow up to 100 liter/min/cm^2. The test section has a length of 30 cm and a cross section of 8 mm by 8 mm. The filter is tested at the point 15 cm downstream from the contraction. Pressure drop across the filters is measured by using a manometer which has a resolution of 0.005 mmHg. The flow rate is measured by the Venturi tube principle, which is shown as follows.

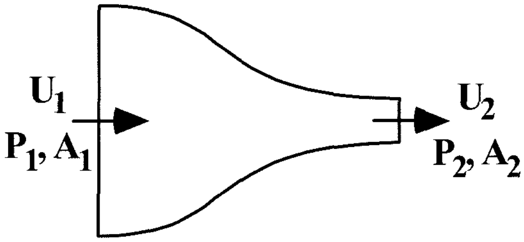

By measuring static pressure before (P_1) and after the contraction (P_2) of the wind tunnel using a MKS Baratron differential pressure transducer and solving the continuity equation,

$$U_1 A_1 = U_2 A_2, \tag{2-1}$$

and the Bernoulli equation,

$$P_1 + \frac{\rho U_1^2}{2} = P_2 + \frac{\rho U_2^2}{2}, \tag{2-2}$$

where

U: average velocity across the cross section,

A: area of the cross section,

ρ: density of air,

P: pressure.

The volumetric flow rate Q can then be calculated as

$$Q = U_2 A_2 = A_2 \sqrt{\frac{2(P_1 - P_2)}{\rho\left(1 - {A_2^2}/{A_1^2}\right)}}. \tag{2-3}$$

Pressure drop as a function of the flow rate per unit area for seven different filters is plotted in Figure 2-9. The power required to sustain a desired flow rate is calculated by multiplying the pressure drop by the volumetric flow rate and the result is shown in Figure 2-10. As expected, it can be seen that the pressure drop and the power requirements strongly depend upon the opening factor of the filter. More interestingly, the shape of the holes also plays an important role. For example, although the filter with hexagonal holes and the filter with rectangular holes have similar opening factors (20% and 21%), the filter with hexagonal holes has much higher pressure drop and power

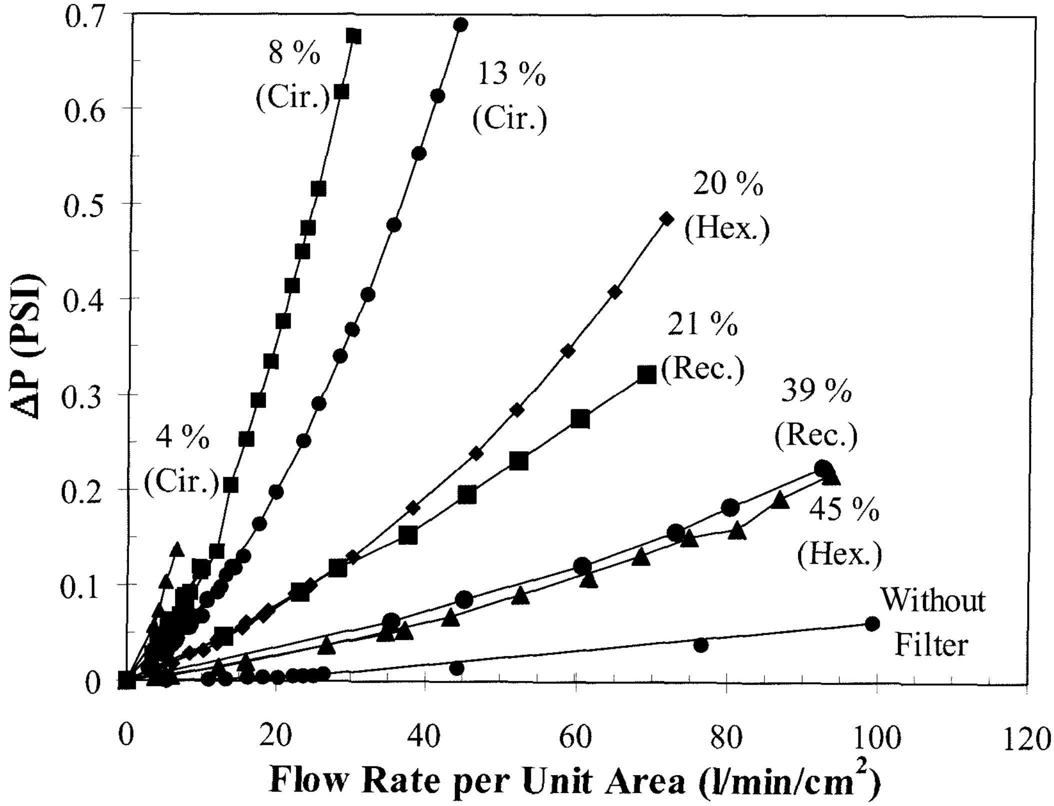

Figure 2-9 Pressure Drop of the Membrane Filters as a Function of Flow Rate

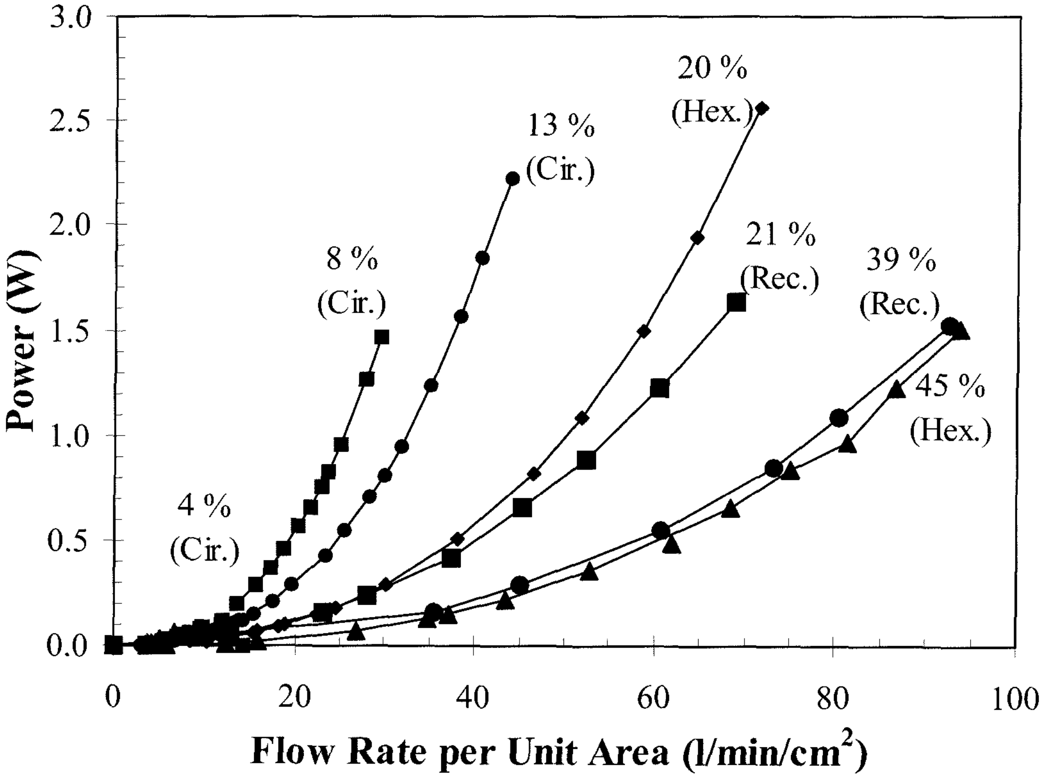

Figure 2-10 Power Requirement of Membrane Filters to Sustain Certain Flow Rate

requirement for any particular flow rate.

2.6 Numerical Calculation

One of the goals of this project is to establish a design guideline for membrane filters. As seen from filter testing results, the pressure drop and the power requirement depend upon the dimension (*d*) and shape of the holes, the thickness of membrane (*t*), and the filter opening factors (β). In non-dimensional analysis, this can be shown as

$$K = \frac{\Delta P}{\frac{1}{2}\rho U_{in}^2} = f(\mathrm{Re}, \beta, t/d), \qquad (2\text{-}4)$$

where

K: pressure coefficient,

ΔP: pressure drop,

Re: Reynolds number which is defined as

$$\mathrm{Re} = \frac{U_h d}{\nu}\,, \qquad (5)$$

where

U_h: average velocity across the hole,

d: diameter of the hole,

ν: kinematic viscosity of air.

In our filter testing experiments, Re is in the range of 1 to 40. Wieghardt [6] and Schubauer *et al.* [7] proposed empirical formulas for K based on their study of conventional screens. In their experiments, the screens were made of two layers of round wires forming a square mesh and had hole size ranging from 75 to 1000 μm. Figure 2-11 compares their empirical formulas with experimental data of conventional screens and our filters. It can be seen that the empirical formulas only fit the conventional screen

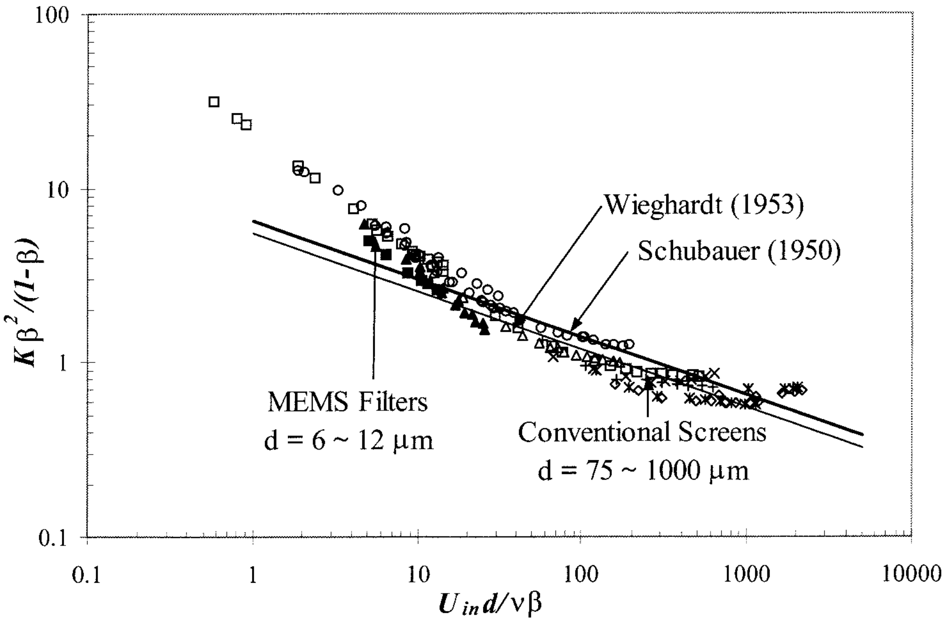

Figure 2-11 Empirical Formulas of Pressure Drop

data, i.e., large Reynolds number flow (Re > 60) and large holes (*d* > 100 μm). Recently, Hasegawa *et al.* [8] investigated the pressure drop through a single orifice as small as 8.8 μm. However, all the testing is conducted with liquid. Therefore, none of the existing empirical formulas can model the fluid dynamic behavior of our membrane filters. Numerical simulation is utilized to aid in determining the empirical formula for the micromachined membrane filters with small holes and operated in low Reynolds number flow regimes. Considering that the filter can be regarded as an array of small holes, we perform numerical simulation around a single axisymmetric cylindrical orifice by using the following model in CFDRC (Computational Fluid Dynamics Research Corporation) software.

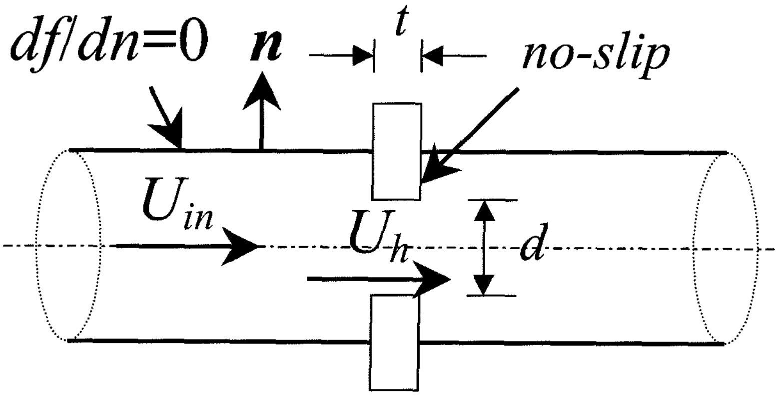

By assuming a no-slip boundary condition at the surface of the filter, viscous laminar flow, and varying the following parameters,

$10\ \% < \beta < 45\ \%$,

$0.08 < t/d < 0.5$,

$1 < \mathrm{Re} < 100$,

the pressure drop is calculated and plotted in Figure 2-12. It is found that the results can be expressed as a single curve regardless of the geometrical parameters if the following non-dimensional form is used:

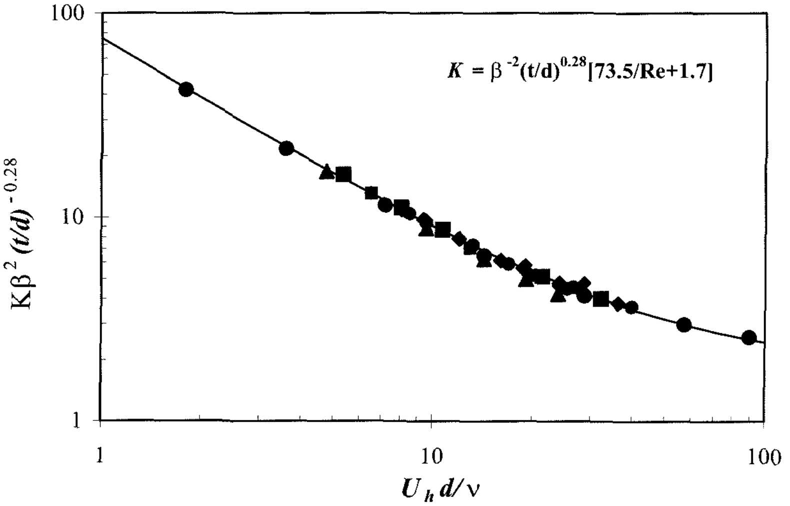

Figure 2-12 Numerical Calculation

$$K\beta^2(\frac{t}{d})^n = f(\frac{U_h d}{\nu}). \tag{2-6}$$

As shown in Figure 2-12, fitting the curve results in the following formula,

$$K = \frac{\Delta P}{\frac{1}{2}\rho U_{in}^2} = \beta^{-2}(\frac{t}{d})^{0.28}[73.5\frac{\nu}{U_h d} + 1.7]. \tag{2-7}$$

Equation (2-7) shows that the pressure drop coefficient varies inversely as the second power of the opening factor β. Thus, it can be concluded that the opening factor is an important parameter in determining the pressure drop. This is consistent with the results shown in Figure 2-9.

2.7 Results and Discussion

To examine the validity of the equation obtained from simulation, it is necessary to compare numerical calculation with experimental results. Plotted in Figure 2-13 are

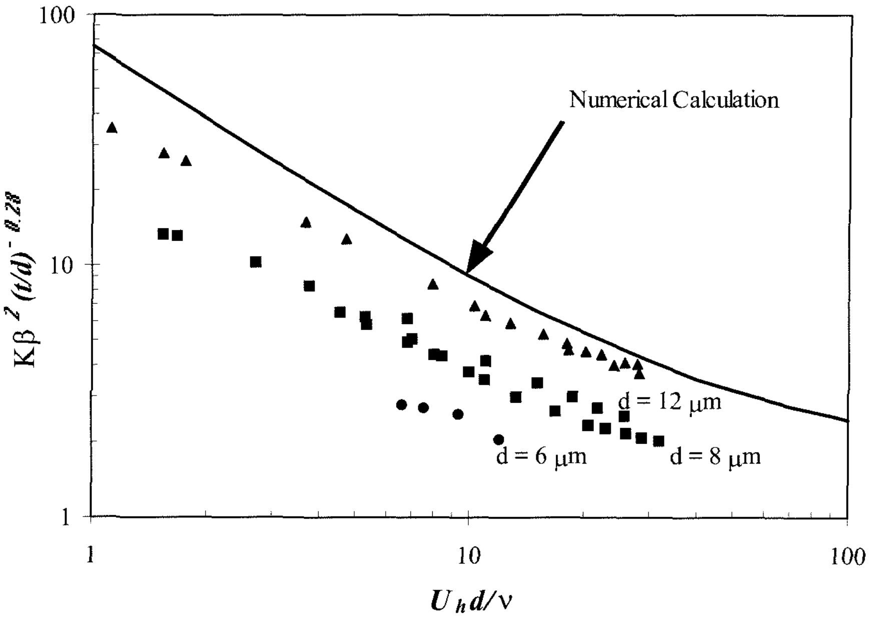

Figure 2-13 Numerical Calculation *Vs*. Experimental Results

pressure drop coefficients from the numerically simulated formula and experimental pressure drop coefficients of filters with 6 μm, 8 μm, and 12 μm holes. It can be seen that the deviation from the numerical result increases as the dimension of the holes decreases. This indicates that some of the assumptions used in numerical calculation are not valid. Since the filter holes are very small, one possibility is that the no-slip boundary condition does not hold. The conventional way to check the possibility of slip at the wall is to calculate the Knudsen number (*Kn*) of the flow field. Knudsen number is defined as the ratio of the mean free path (λ) of the working fluid (air, in this case, $\lambda = 0.0685$ μm at 1 atm) to the physical dimension of the flow field (hole size, d). It is traditionally known that slip occurs at the wall only if the Knudsen number is larger than 0.01. The Knudsen number is plotted as a function of the hole size of the filters in Figure 2-14. It is shown that Knudsen number of the filters ranges from 0.005 to 0.015. The Knudsen number in the case of d = 8 μm is approximately 0.009, which means that slip could be significant. To determine if the no-slip boundary condition is truly the cause of the large discrepancy between numerical calculation and experimental results,

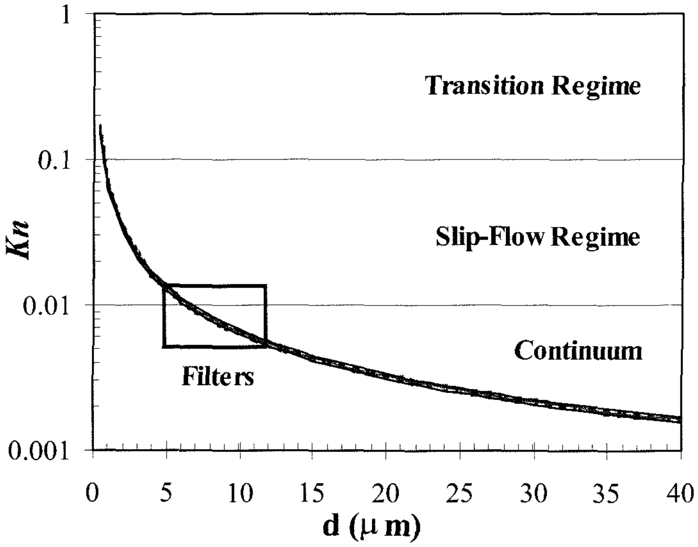

Figure 2-14 Knudsen Number of Flow in Filter

additional numerical calculation are performed that include the following slip boundary condition,

$$u_w = \pm \frac{2-\alpha}{\alpha} \lambda \left. \frac{du}{dy} \right|_w , \tag{8}$$

where

α : accommodation constant (which ranges from 0 to 1),

λ: mean free path of air.

The result is shown in Figure 2-15. Even though the slip boundary condition is included and α is varied between 0 and 1, there is still a large difference. This suggests that some other mechanisms must be attributed to this effect. For example, in the numerical calculations, no consideration is given to surface roughness and interaction between the wall surface molecules and the molecules in the air flow. Also, to simplify the simulation process, several assumptions about the filtering holes were used. First, the holes are assumed to be circular even though in reality the filter holes are hexagonal. Second, the holes are assumed to have vertical side walls. This is not true for the reason that the RIE etching has certain degree of undercut. So far, however, no specific mechanism has been

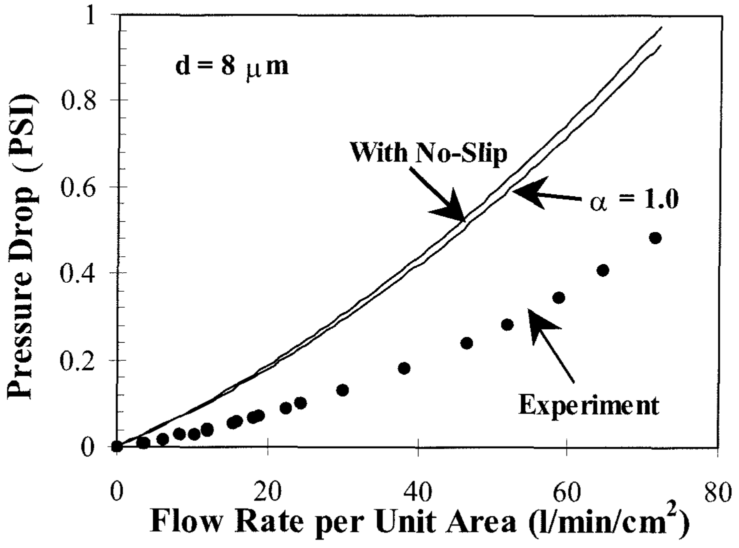

Figure 2-15 Numerical Calculation with Slip Boundary Conditions

identified that satisfactorily explains the discrepancy. More work is needed to determine which one of the above three mechanisms or all are responsible.

2.8 Conclusion

Several particle membrane filters (8 × 8 mm^2) with circular, hexagonal, and rectangular filtering holes have been designed, fabricated, and tested. By varying hole dimensions from 6 to 12 μm, opening factors from 4% to 45% are achieved. A composite silicon nitride/Parylene membrane technology is developed to enhance filter strength. Fluid dynamic performance of the filters has been studied extensively through experiments and numerical simulations. It is found that gaseous flow in the filters strongly depends on opening factors. Furthermore, the measured pressure drops are much lower in comparison to numerical simulation results. Numerical calculation with a slip boundary condition shows that surface velocity slip can only account for a minor part of the difference. Although the membrane filters and their functionality have been successfully developed, more work is needed to determine the fluid dynamic mechanism that causes this discrepancy.

Bibliography

[1] C. N. Davies, *Aerosol Science*, pp. 409, Academic Press, 1966.

[2] C. J. M. van Rijin, and M. C. Elwenspoek, "Micro Filtration Membrane Sieve with Silicon Micro Machining for Industrial and Biomedical Applications," Proceedings of IEEE Workshop on Micro Electro Mechanical Systems (MEMS'95), pp. 83-87, Amsterdam, The Netherlands, January 1995.

[3] C. J. M. van Rijin, M. van der Wekken, W. Nijdam, and M. C. Elwenspoek, "Deflection and Maximum Load of Microfiltration Membrane Sieves Made with Silicon Micromachining," Journal of Microelectromechanical Systems, Vol. 6 (1), pp. 48-54, March 1997.

[4] G. Kittilsland, G. Stemme, and B. Norden, "A Sub-micron Particle Filter in Silicon," Sensors and Actuators (A:Physical), Vol. 23, pp. 904-907, 1990.

[5] M. Sekimoto, H. Yoshihara, and T. Ohkubo, "Silicon Nitride Single-Layer X-Ray Mask," Journal of Vacuum Science and Technology, Vol. 21(4), pp.1017-1021, November/December 1982.

[6] K. E. G. Wieghardt, "On the Resistance of Screens," The Aeronautical Quarterly, Vol. IV, pp.186-192, February 1953.

[7] G. B. Schubauer, W. G. Spangenberg, and P. S. Klebanoff, "Aerodynamic Characteristics of Damping Screens," N. A. C. A., Technical Notes 2001, 1950.

[8] T. Hasegawa, M. Suganuma, and H. Watanabe, "Anomaly of Excess Pressure Drops of the Flow Through Very Small Orifices," Physics of Fluids, Vol. 9(1), pp. 1-3, January 1997.

[9] J. M. Yang, C. M. Ho, X. Yang, and Y. C. Tai, "Measurement of Viscous Dissipation Through Micro-Screens," American Physics Society, The 50th Annual Meeting of the Division of Fluid Dynamics, San Francisco, California, November 1997.

[10] X. Yang, J. M. Yang, X. Q. Wang, E. Meng, Y. C. Tai, and C. M. Ho, "Micromachined Membrane Particle Filters," Proceedings of IEEE Workshop on Micro Electro Mechanical Systems (MEMS'98), pp. 137-142, Heidelberg, Germany, January 1998.

[11] X. Yang, J. M. Yang, Y. C. Tai, and C. M. Ho, "Micromachined Membrane Particle Filters," Submitted to Sensors and Actuators (A:Physical).

Chapter 3

Valve Design Considerations

3.1 Introduction

As a basic fluid control device, the valve has attracted a lot of research attention over the last few years. When designing a valve, two things need to be considered: mechanical structure and actuation mechanism. Most of the reported MEMS valves have a membrane as the mechanical structure probably because membranes are easy to fabricate. Typically, a membrane valve consists of a valve seat (with fluid inlet/outlet) and a membrane which initially could be separated from the valve seat (normally-open) or be in contact with the valve seat (normally-off). To operate the valve, an actuation mechanism is required to deflect the membrane. Consider a normally-open valve (Figure 3-1) as an example. It operates as follows. When the actuation mechanism is off, there is a gap between the valve seat and the membrane and fluid flows through the gap. When the actuation mechanism is on, the membrane deflects upward, seals the flow inlet, and shuts off the flow. The desired performance features of such a valve are high flow rate and high pressure range. It is obvious from Figure 3-1 that when the valve is on, the flow rate through the valve is limited by the gap between the valve seat and membrane. To achieve high flow rate, a large gap is preferred, which means the membrane has to deliver a large deflection to close the valve. A typical gap distance is 50 μm for a reasonable flow rate (> 1 liter/min of nitrogen flow). Now, consider the pressure range. High pressure range means that the valve is able to shut off the flow against a high supply pressure. To this end, an actuation mechanism that can provide large force is desired. Besides high flow rate and high pressure range, other common requirements are small size, low power

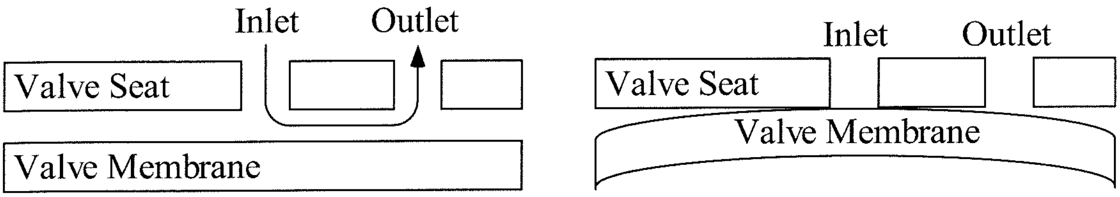

(a) Off (b) On

Figure 3-1 Conceptual Drawing of a Normally-Open Valve

consumption, and fast frequency response. It should be noted that, unfortunately, these requirements are not necessarily simultaneously achievable. For example, a large deflection membrane normally has a large size and a large actuation force often needs large power consumption.

In summary, a high performance MEMS valve requires a large-deflection, small-size mechanical structure and a large-force, low-power actuation mechanism. In the following sections, possible approaches to achieving these requirements will be studied.

3.2 Actuation Mechanism

Many actuation mechanisms have been explored. Here, the four most common ones, namely, electrostatic, electromagnetic, bimetallic, and thermopneumatic, are studied and compared for MEMS valve applications. For the sake of simplicity, a 2 mm × 2 mm membrane and a 50 μm gap are assumed.

3.2.1 Electrostatic Actuation

Electrostatic force is created by applying a voltage across a fixed plate and a movable plate which are separated by a gap. The force is calculated according to the following equation,

$$F = \frac{1}{2}\varepsilon S\left(\frac{V}{d}\right)^2 \tag{3-1}$$

Where

F: electrostatic force,

ε: dielectric constant (for air, 8.854×10^{-12} N/V^2),

S: electrode surface area,

V: applied voltage,

d: electrode distance.

Now, assuming 200 V is applied between the two electrodes, the electrostatic force is calculated to be 283 μN. By dividing the force with the total electrode area, we can also estimate the pressure, which is 71 Pa (~0.01psi).

It can be seen from the above simple calculation that the electrostatic force is small and usually in the range of μN. This should not be a surprise because as shown in Equation 3-1, the electrostatic force is inversely proportional to the second power of the distance. For high flow rate valve with large gap, the force is significantly decreased. For this reason, electrostatic actuation is not suitable for valve applications even though it has other advantages of simple structure, very low power consumption, and fast frequency response.

3.2.2 Electromagnetic Actuation

In the presence of a magnetic field strength of **B**, a current-carrying (**I**) wire with length L will experience the Lorentz force, which is defined as

$$\mathbf{F} = (\mathbf{I}\times\mathbf{B})L \tag{3-2}$$

Assuming there are ten 2 mm long wires, each carrying 1 A current and a magnetic field of 0.1 N/m-A generated by a typical magnet, the Lorentz force is calculated to be 2 mN. This shows that the Lorentz force is in the range of mN, but application of this force requires a bulky external permanent magnet.

Another common form of magnetic actuation [1] is shown in Figure 3-2. When the magnetic flux in a magnetic circuit crosses an air gap, it produces an attractive force

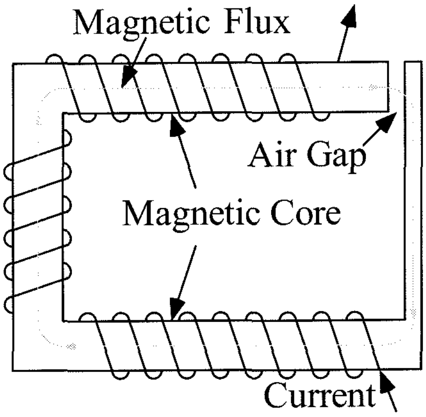

Figure 3-2 Magnetic Actuation

between the faces at both ends of the air gap. This force can be calculated using the following equation,

$$F = \frac{\phi_g^2}{2\mu_0 A_g} \tag{3-3}$$

where

μ_0: permeability,

A_g: the air gap cross-sectional area,

ϕ_g : magnetic flux in the magnetic circuit,

and ϕ_g can be found using magnetic circuit concept,

$$\phi_g = \frac{NI}{\Re_c + \Re_g} \tag{3-4}$$

where

N: number of coil turns,

I: coil current,

$\Re_c$: magnetic reluctance of the magnetic core,

$\Re_g$: magnetic reluctance of the air gap.

Theoretically, it is desirable to have $\Re_g >> \Re_c$ to maximize the efficiency of the actuator. However, in reality, it is difficult to achieve this due to the geometry constraints in

MEMS devices. Assuming $\Re_c$ can not be neglected, magnetic power transmitted to the gap is maximized when $\Re_g = \Re_c$.

Let's estimate the generated force. Assuming a layer of 20 μm thick, 2 mm long NiFe permalloy, which has a permeability of 5000, is used as the magnetic core, and that 10 turns of coil carrying 1 A current generate the magnetic flux, the attractive force between the two magnetic surfaces is calculated to be on the order of 1 mN. The advantage of this actuation over the Lorentz force is that everything is integrated on the chip and no external magnet is needed.

It can be concluded from the above that electromagnetic actuation can generate forces in the range of mN with reasonable power consumption.

3.2.3 Bimetallic Actuation

When a pair of materials with different thermal expansion coefficients are bonded together and subjected to a temperature change, stresses are generated in the structure and can cause useful deflections and forces. Although a large variety of combinations of materials can be used, the use of a silicon diaphragm and an aluminum metallic layer is one of the most attractive ones [2]. A typical bimetallic structure is shown in Figure 3-3. Assuming a clamped membrane, 2.5 mm in diameter with 9 μm thick silicon and 6 μm thick aluminum and a boss ratio (b/a) of 0.4, the force and deflection are plotted in Figure 3-4 [2]. The maximum force is about 71 mN.

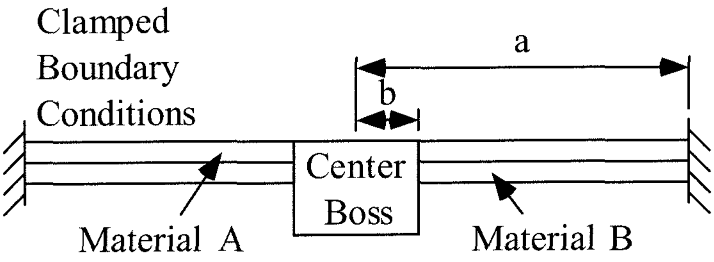

Figure 3-3 Bimetallic Structure

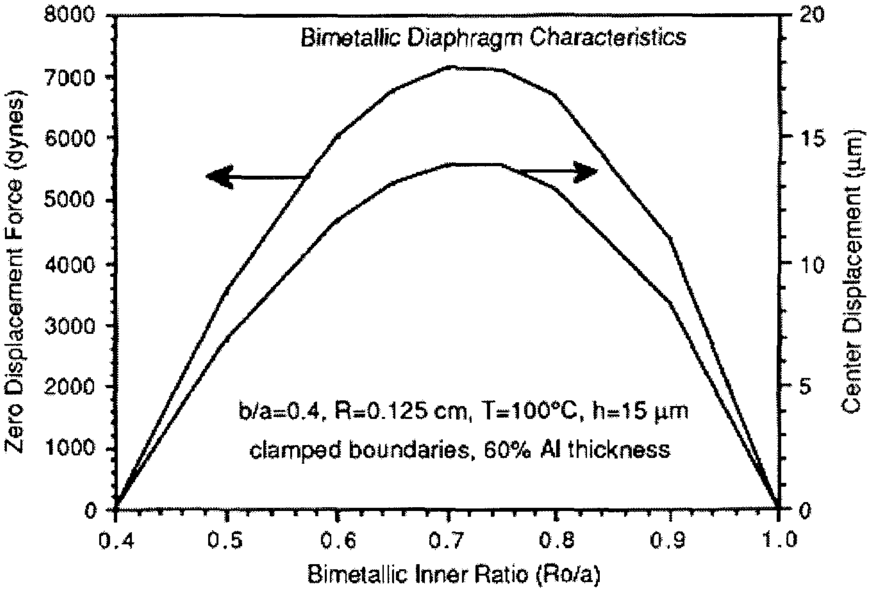

Figure 3-4 Force and Deflection of Bimetallic Structure (From [2])

3.2.4 Thermopneumatic Actuation

If gas or liquid is heated up, it will expand. If the gas or liquid is sealed in a cavity and the expansion is restricted, the pressure inside the cavity will rise. By taking advantage of this pressure increase, large actuation force can be generated. There are three possible ways to achieve the pressure increase, thermal expansion of gas, thermal expansion of liquid, and phase change from liquid to gas. Here, we will take thermal expansion of liquid as an example to estimate the generated force.

The pressure increase can be calculated according to the following equation:

$$\Delta P = E\left(\beta \Delta T - \frac{\Delta V}{V}\right) \qquad (3\text{-}5)$$

where

E: bulk modulus of elasticity,

β: thermal coefficient of expansion,

ΔT: temperature increase,

ΔV/V: cavity volume increase percentage.

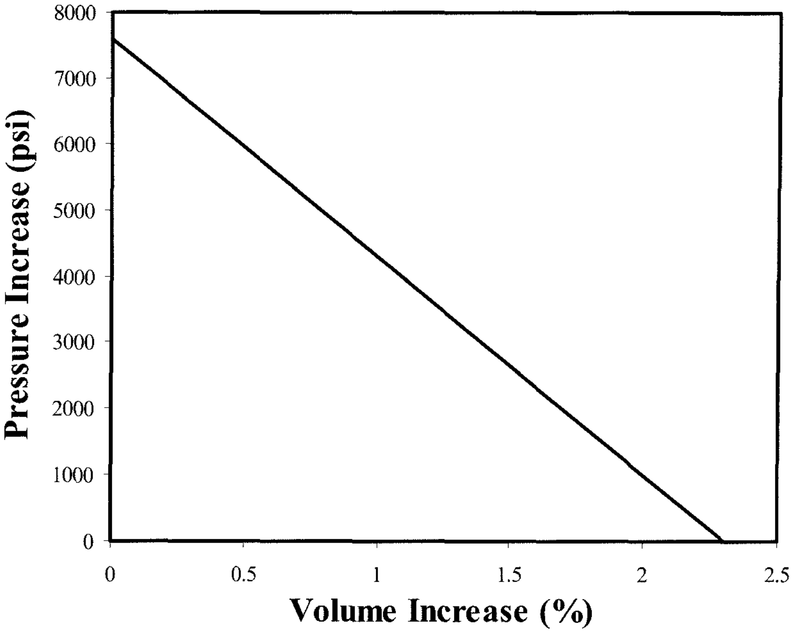

Figure 3-5 Pressure Increase Generated by Thermopneumatic Actuation

Take water as an example for the actuation liquid. It has a bulk modulus of 3.3×10^5 psi and a thermal expansion coefficient of 2.3×10^{-4} /°C. Assuming a temperature increase of 100 °C, the pressure increase as a function of the volume increase is plotted in Figure 3-5. We can see from the curve that in the case of MEMS valves, which have small volume change during operation, the generated pressure can be as high as a few thousand psi.

The power consumption can be estimated using Fourier's Law of thermal conduction.

$$q = kA\frac{\Delta T}{L} \tag{3-6}$$

Where

q: heater power consumption,

k: thermal conductivity of working liquid,

A: total surface area,

ΔT: temperature difference between heater and valve membrane,

L: distance between heater and valve membrane.

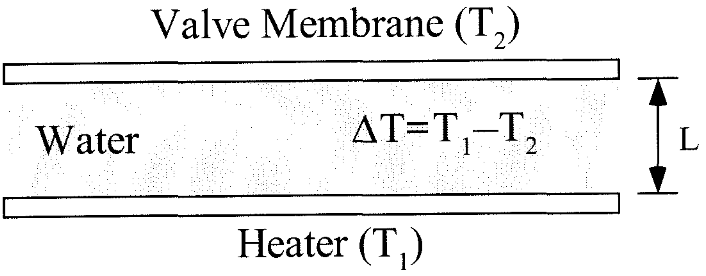

Figure 3-6 Simple Valve Actuator Model for Power Consumption Estimation

Shown in Figure 3-6 is a simple model of the actuator. Basically, it is a water filled cavity with a valve membrane on one side of the cavity and heater on the other side. Assume there is a temperature difference of 100 °C between the heater and the membrane which are apart by 500 μm, and the heater and membrane have an area of 2 mm × 2 mm. Since water has a thermal conductivity of 615 mW/m-°C, the power consumption is calculated to be 492 mW.

Other than water, many other liquids can be used for thermopneumatic actuation. Among them, one family of liquid, Freon^{TM} or Fluorinert^{TM}, is very attractive for many reasons. They are non-conductive, non-corrosive, and commercially available from DuPont and 3M. More importantly, their specific heat is one fourth that of water, but their thermal expansion coefficient is greater by a factor of six. Their thermopneumatic actuation performance has been studied by [3] and will be presented in Chapter 6 and 7.

In conclusion, among the four actuation mechanisms, thermopneumatic actuation can provide the largest pressure or force with reasonable power consumption. Also, it can be easily integrated with the mechanical structure to form a valve. For these reasons, we choose it to be our valve actuation mechanism.

3.3 Mechanical Structure

Due to the planar nature of the fabrication process, the membrane is the most common mechanical structure for MEMS valves. As pointed out in 3.1, in order to achieve high flow rate in MEMS valves, large membrane deflection is desired. Let's examine the

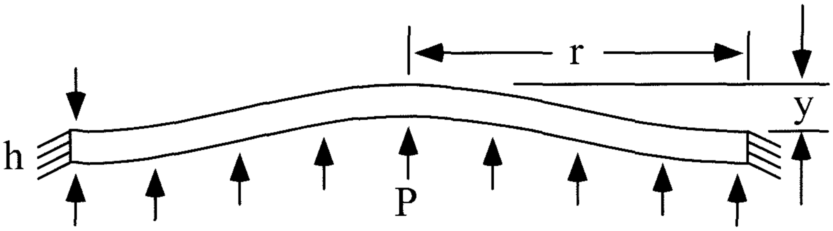

Figure 3-7 Circular Membrane with Clamped Boundary Conditions

membrane mechanical behavior and find out how to achieve large deflection. Shown in Figure 3-7 is a circular membrane with clamped boundary conditions. Its deflection can be determined from the following equation [4]:

$$\left(\frac{P}{E}\right)\left(\frac{r}{h}\right)^4 = \frac{16}{3(1-\nu^2)}\frac{y}{h} + \frac{7-\nu}{3(1-\nu)}\left(\frac{y}{h}\right)^3 \tag{3-7}$$

where

P: pressure,

E: Young's modulus of membrane material,

r: membrane radius,

h: membrane thickness,

ν: Poisson's ratio of membrane material,

y: membrane deflection.

In valve applications, the membrane is operated in the large deflection regime, i.e., y >> h. Under such a condition, at the right-hand side of the equation, the second term is much larger than the first term, which means the first term can be neglected.

$$\left(\frac{P}{E}\right)\left(\frac{r}{h}\right)^4 \approx \frac{7-\nu}{3(1-\nu)}\left(\frac{y}{h}\right)^3 \tag{3-8}$$

Equation (3-8) shows that there are three options to achieve large deflection (y) in membrane. First, materials with small Young's modulus (i.e., small E) can be used for the membrane. Unfortunately, this is not very practical because all the common materials in MEMS have relatively large Young's modulus. For example, the modulus of silicon is in the range of 139 to 190 GPa. The second option is to use thin membranes (i.e., small

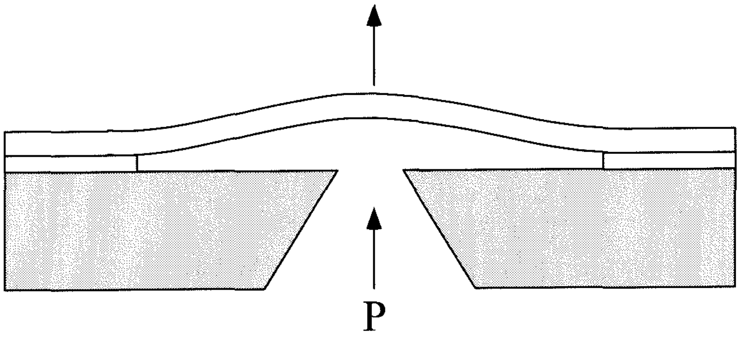

(a) Single-Layer Flat Membrane

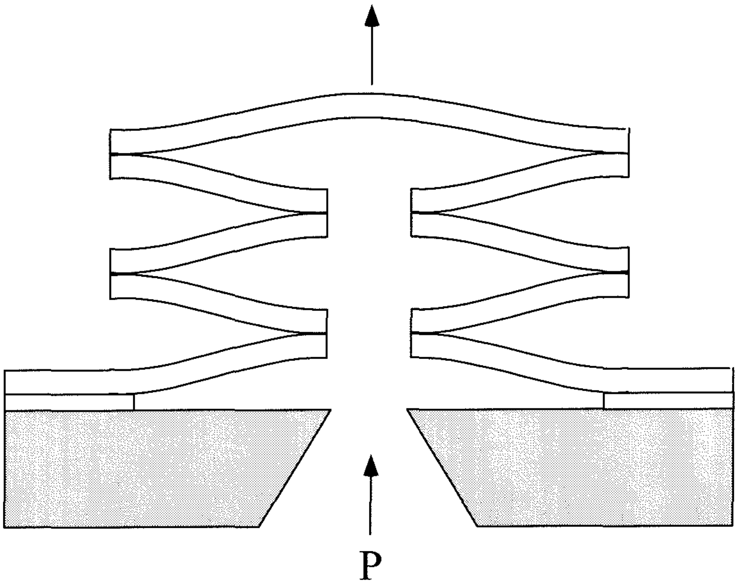

(b) Multi-Layer Microbellows

Figure 3-8 Membrane *Vs.* Microbellows

h). Although this will help increase the deflection, it will significantly decrease the strength of the membrane, which is directly related to the valve operating pressure range. Another concern is that very thin membranes are difficult to be fabricated. For these two reasons, the application of thin membranes is very limited. The third option is to use large membranes (i.e., large r). Since the first two options are not very useful, this one is commonly used to achieve large membrane deflection. As a result, most of today's MEMS valves have a very large membrane size (at least a few mm). In other words, there is a conflict between large deflection and small size in membrane structure.

Our first approach to this problem is to develop a new mechanical structure to achieve large deflection and small size at the same time. The new structure is shown in Figure 3-8. Instead of a single layer flat membrane, multiple structural layers are stacked together to form a structure in the form of bellows. This new structure, microbellows, will be described in detail in Chapter 5.

Another approach we took is to use alternative low modulus materials for membrane. To this end, we have chosen silicone rubber and Parylene. As shown in Chapter 6 and 7, silicone rubber and Parylene are much more flexible compared to silicon. We have also incorporated processing of these materials with conventional MEMS fabrications. The application of these materials in valves will be presented in Chapter 6 and 7.

3.4 Conclusion

It has been identified that large actuation deflection and large actuation force are the key to a high flow rate, high pressure range valve. Electrostatic, electromagnetic, bimetallic, and thermopneumatic actuation have been studied and compared. The results show that thermopneumatic actuation can provide the largest actuation force among the four. To achieve large deflection, the mechanical performance of membrane has been examined. Microbellows structure and low modulus materials (silicone rubber and Parylene) are proposed to achieve large deflection and small size in the valve actuator.

Bibliography

[1] J. A. Wright, Y. C. Tai, and S. C. Chang, “A Large-Force, Fully-Integrated MEMS Magnetic Actuator,” Technical Digest, International Conference on Solid-State Sensors and Actuators (Transducers '97), Vol. 2, pp. 793-796, Chicago, USA, June 1997.

[2] H. Jerman, “Electrically-Activated, Micromachined Diaphragm Valve,” Technical Digest, IEEE Solid-State Sensor and Actuator Workshop, pp. 65-69, Hilton Head Island, South Carolina, USA, June 1990.

[3] M. J. Zdeblick, *A Planar Process for an Electric-to-Fluidic Valve*, Ph.D. Thesis, Stanford University, 1988.

[4] M. Di Giovanni, *Flat and Corrugated Diaphragm Design Handbook*, Marcel Dekker, Inc., 1982.

Chapter 4

Technology Issues for Microbellows Design and Fabrication

4.1 Introduction

In the 1980's, Berkeley researchers fabricated various micromechanical devices [1,2,3,4] using polysilicon surface micromachining technology. In their fabrication process, LPCVD polysilicon was used as the structural layer, phosphosilicate glass (PSG) as the sacrificial layer and hydrofluoric acid (HF) as the selective etchant. Although advantages of this technology were demonstrated, many other issues remained unstudied. Since then, many efforts have been made to further improve this technology. For example, low stress and low stress gradient were achieved in the structural layer. The PSG etching process was studied and modeled [5]. The stiction of released structures to the substrate was studied and possible ways to avoid stiction were proposed [6]. In this chapter, we present the studies of three key issues related to the design and fabrication of surface micromachined bellow actuators (microbellows). First, polysilicon sacrificial layer technology is explored. Second, the cracking of the surface micromachined structures is studied and design guidelines to avoid cracking are provided. Finally, three boundary conditions of surface micromachined membranes are examined and the results show that the strength of surface micromachined membranes strongly depends on the boundary conditions.

4.2 Polysilicon Sacrificial Technology

Polycrystalline silicon (polysilicon) deposited using low pressure chemical vapor deposition (LPCVD) technology has been well studied because it is widely used as the gate material in IC's and the structural layer in MEMS. Until recently, surface micromachining using polysilicon as sacrificial layer has not been fully explored. In this technology, silicon nitride can be the structural layer and potassium hydroxide (KOH) or tetramethylammonium hydroxide (TMAH) can be the selective etchant. Potentially, this technology can have many advantages over the popular PSG/HF scheme [7]. First, TMAH shows extremely high etching selectivity of polysilicon over silicon nitride while in the case of PSG/HF technology, high concentration HF etches silicon nitride at the rate of 50-60 Å/min. Usually, no HF etching longer than 30 minutes is used because a significant amount of silicon nitride would be lost otherwise. Second, TMAH etches polysilicon sacrificial layers at a constant rate. But in HF etching, the etch rate decreases as the etching distance increases because the transport of fresh etchant to the etch front is limited by the diffusion process [5]. Because of these two reasons, large surface micromachined structures can be fabricated using polysilicon sacrificial technology. Third, similar to single crystalline silicon, polysilicon heavily doped with boron shows decreased etch rate in TMAH and hence can serve as an etch stop. As shown in Figure 4-1, by selectively doping certain areas of the polysilicon sacrificial layer, surface

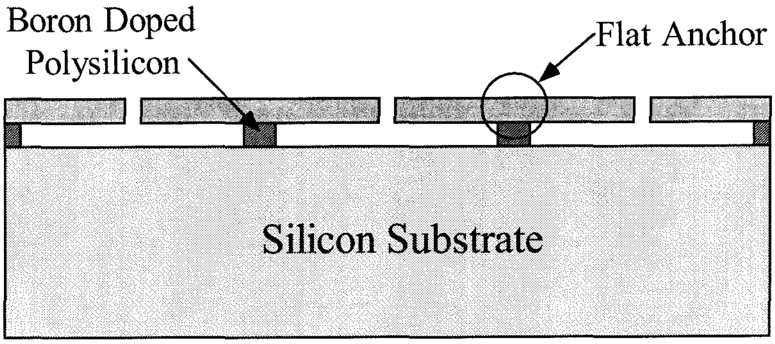

Figure 4-1 Boron Doped Polysilicon Etch Stop

micromachined structures with flat anchors can be fabricated. This is very important as it will be shown later in Section 4.4. However, in PSG/HF technology, it is very difficult to achieve the flat anchors. Last but not least, the TMAH etching process is IC compatible because TMAH was originally developed for use as photoresist developer in IC fabrication. This can be advantageous in the case of integrated IC/MEMS fabrication.

4.2.1 Design and Fabrication of Test Structures

In order to study the polysilicon sacrificial etching process, surface micromachined straight channels and circular membranes have been designed and fabricated. The fabrication process is as follows. First, a layer of 0.2 μm LPCVD silicon nitride was deposited on the substrate. This silicon nitride layer served as the passivation layer for the substrate during the final TMAH etching. Then, a layer of 1 μm thick LPCVD polysilicon was deposited at 620 °C, followed by patterning and SF_6/O_2 plasma etching to define the sacrificial layer. Another layer of 1 μm thick LPCVD silicon nitride was deposited at 850 °C with a SiH_2Cl_2/NH_3 gas flow ratio of 4/1 to achieve low stress [8]. This silicon nitride layer served as the structural layer. Finally, etching windows were patterned and etched using SF_6/O_2 plasma.

The diameter of circular membranes is from 300 μm to 1 mm. The straight channels are 4 mm long and their width is varied from 10 μm to 1mm.

4.2.2 *In situ* Study of Polysilicon Etching Using TMAH

Polysilicon etching by TMAH was studied using the experimental setup shown in Figure 4-2. A quartz beaker containing TMAH solution was placed on a hot plate. Constant cooling water was flowing through a condenser which sat on top of the beaker. The temperature of the solution was feedback controlled with a thermal probe inserted in the solution. A magnetic bar in the solution provided the stirring. Also, to slow down the aging of the solution, a small flow of nitrogen was passed through the solution to keep CO_2 out. The chip to be etched was positioned against the inside surface of the beaker.

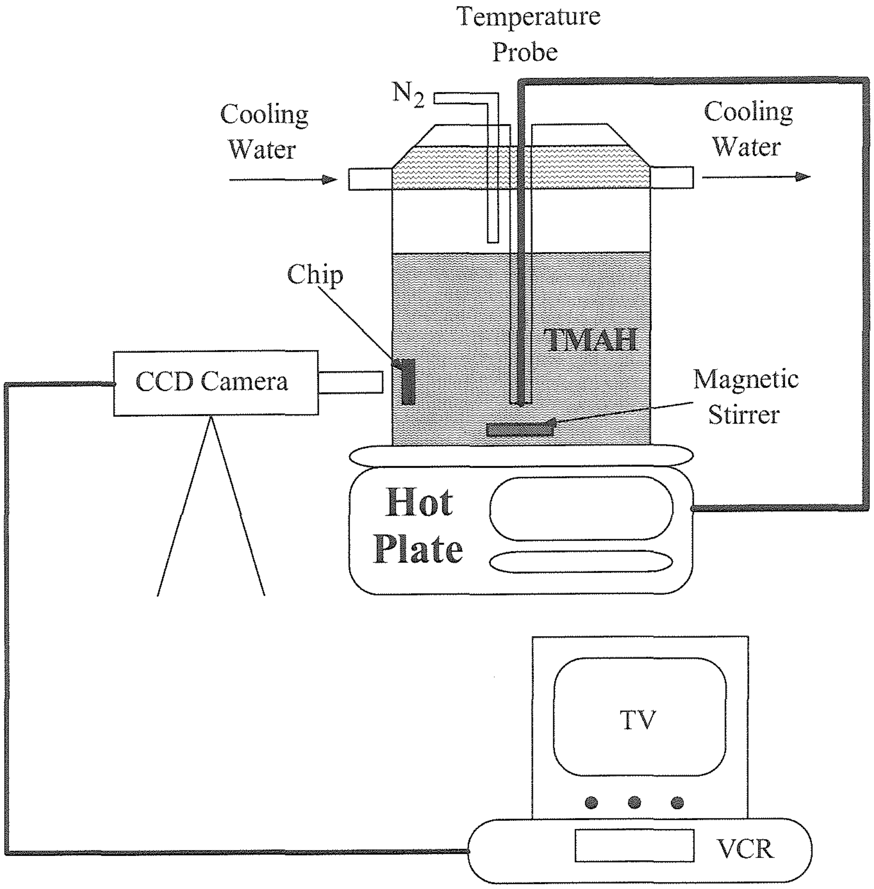

Figure 4-2 Polysilicon Etching *In situ* Study Experiment Setup

All the etching activities were recorded using a CCD camera and a VCR. The etching length was measured using an on-chip ruler.

The etching experiments were performed under two different TMAH concentrations (10% and 15% by weight) and two different temperatures (80 °C and 90 °C). In all cases, 200 rpm stirring was used. The measured etching distance as a function of the etching time for straight channels and circular membranes is plotted in Figure 4-3, and Figure 4-4 shows a picture of etched channels. First, in the case of straight channels, the etching rate is not sensitive to the channel width. All the channels with different widths have the same etch rate. Second, it can be seen from the two curves that, unlike PSG etching which has decreased etch rate as etch distance increases, polysilicon etching has a constant etch rate up to 600 μm. The etch rates of polysilicon

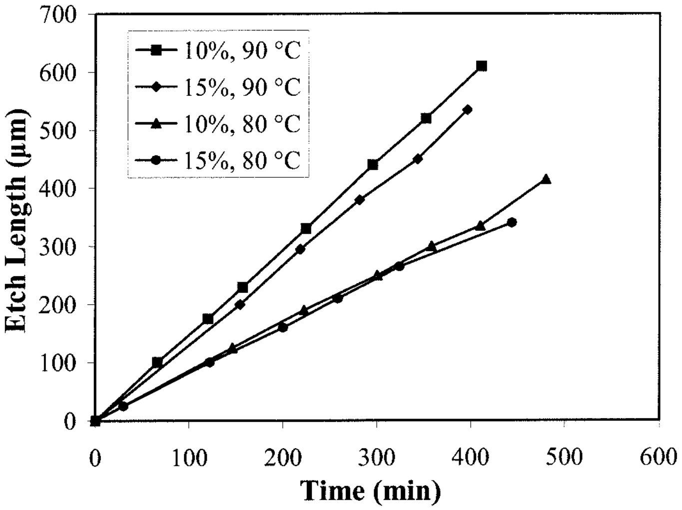

(a) Straight Channels

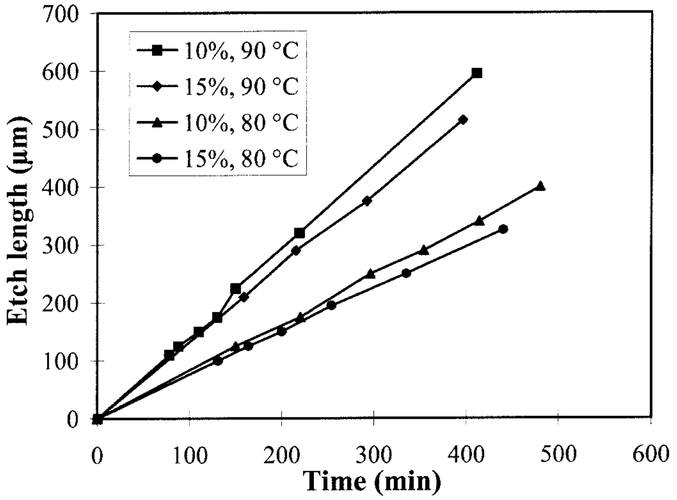

(b) Circular Membranes

Figure 4-3 Etch Rate of Polysilicon in TMAH

and masking materials such as silicon nitride and silicon oxide under different etching conditions are shown in Table 4-1. It can be seen that TMAH has extremely high etching selectivities of polysilicon over silicon nitride or silicon oxide. Compared to high concentration HF, TMAH solution etches silicon nitride very slowly. This means large structures can be micromachined using this etching scheme. From the etch rates of

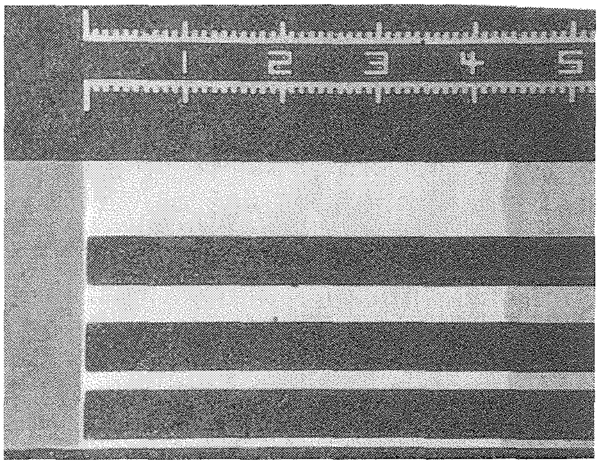

Figure 4-4 Picture of Etched Channels

Table 4-1 Etch Rate of Polysilicon, SiN and SiO_2 in TMAH

Etching Condition	Polysilicon Etch Rate (μm/min)	SiN Etch Rate (Å/min)	SiO_2 Etch Rate (Å/min)
10%, 90 °C	1.48	0.47	2.1
15%, 90 °C	1.34	0.68	2.1
10%, 80 °C	0.84	0.43	0.97
15%, 80 °C	0.78	negligible	0.38

polysilicon under different conditions, the etching activation energy can be calculated using the Arrhenius equation.

$$R(T) = R_0 e^{-\frac{E_a}{kT}} \tag{4-1}$$

where

$R(T)$: etch rate at temperature T,

R_0: constant,

E_a: activation energy,

k: Boltzmann constant, 8.6×10^{-5} eV/ °K, T: temperature in °K.

The activation energy of polysilicon etching in 10% TMAH solution was found to be 0.62 eV and in 15%, it was 0.6 eV. These are similar to the ones for bulk silicon etching [9]. These results suggest that the etching process is dominated by the chemical reaction, not by the diffusion of fresh etchant from the bulk to the etching front. It was observed from the etching process that hydrogen bubbles were generated constantly as a byproduct of the etching. These bubbles were not released from the structure smoothly. They first accumulated in the etched structures, then suddenly exhausted from the etching windows. It is suggested that these bubbles are responsible for transporting fresh etching solution to the etching front. Also, the constant accumulation and releasing of these bubbles caused the deformation and oscillation of the released structures. Although this is a serious problem for bulk silicon etching [10], all the structures in these experiments survived probably because the cross section of the etching front was very small and the amount of generated hydrogen bubbles was small. Finally, it is found that the etching fronts in the straight channels have a triangular shape (Figure 4-4). Although no effort has been made to study this phenomenon, it is suspected the stress relaxation in the silicon nitride layer might be responsible.

4.2.3 Boron Doped Polysilicon Etch Stop

Heavily boron doped bulk silicon shows very small etch rate in EDP, KOH, and TMAH solutions. Because of this, it is widely used as an etch stop in bulk micromachining. The polysilicon sacrificial layer heavily doped with boron is proposed to have similar etch stop characteristics. The potential advantage of this technique is that by selectively doping the structural anchoring region of the sacrificial layer, the structure does not have a step at the anchor after being released (Figure 4-5). The strength of the structure is greatly improved as shown in Section 4-4.

To demonstrate this technique, an array of hexagonal surface micromachined membranes was fabricated. The fabrication process is shown in Figure 4-5. First, a layer of 0.2 μm LPCVD silicon nitride was deposited on the substrate. This silicon nitride layer

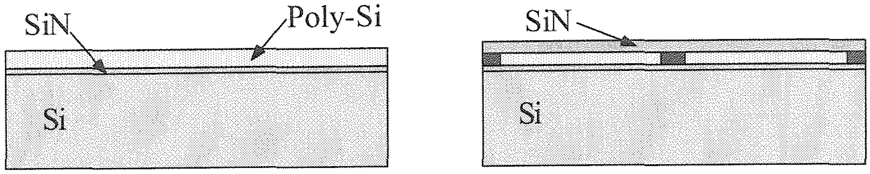

(a) SiN and Poly-Si Deposition

(c) Oxide Stripping, Nitride Deposition and Annealing

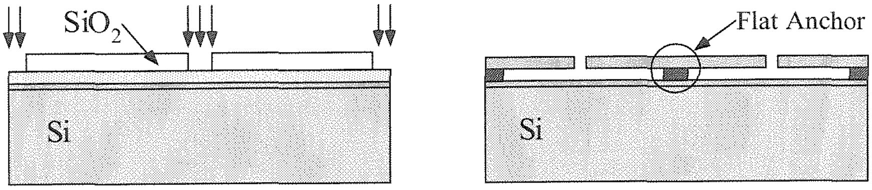

(b) Thermal Oxidation, Oxide Patterning and Ion Implantation

(d) Nitride Patterning and Poly-Si Etching in TMAH

Figure 4-5 Test Structure Fabrication Process

served as the passivation layer for the substrate during the final TMAH etching. Then, a layer of 1 μm thick LPCVD polysilicon was deposited at 620 °C. After that, the wafers were put into the thermal oxidation furnace. At 1050 °C for 4 hours, 0.5 μm thick of the polysilicon layer was converted into 1 μm thick silicon oxide. The thermal oxide layer was then patterned and etched to open the windows for ion implantation. Boron ion implantation was performed at the energy of 80 KeV with dosage of $10^{16}/cm^2$ and $4\times10^{16}/cm^2$ on two sets of wafers. The doping concentration was calculated to be $2\times10^{20}/cm^3$ and $8\times10^{20}/cm^3$ respectively. The thermal oxide layer was stripped using buffered HF followed by deposition of a 0.6 μm thick LPCVD silicon nitride at 850 °C with a $SiH_2Cl_2:NH_3$ gas flow ratio of 4:1 to achieve low stress [8]. The wafers were then annealed at 1100 °C for 30 minutes to drive in and activate the boron dopants. Finally, etching windows were opened in the structural silicon nitride layer using SF_6/O_2 plasma and the surface micromachined membranes were released in a 10% TMAH solution at 90 °C.

Part of the layout of the hexagonal membrane array is shown in Figure 4-6. Figure 4-7 is a picture of the membranes after ion implantation. Basically, the white area is the anchor region and was doped with boron while the black area was covered with silicon oxide mask layer. Between the membranes, there are many etch holes. Shown in Figure

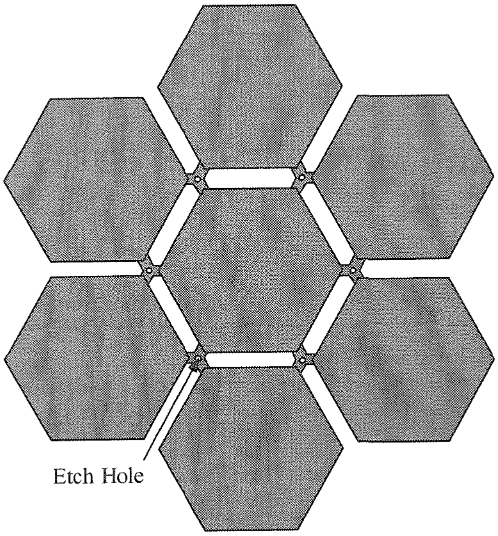

Figure 4-6 Layout of Hexagonal Membrane Array

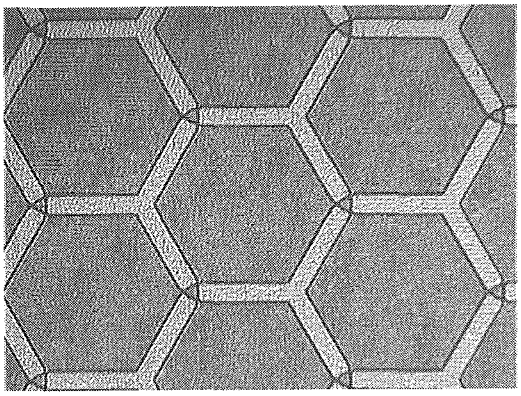

Figure 4-7 Picture of Membranes after Ion Implantation

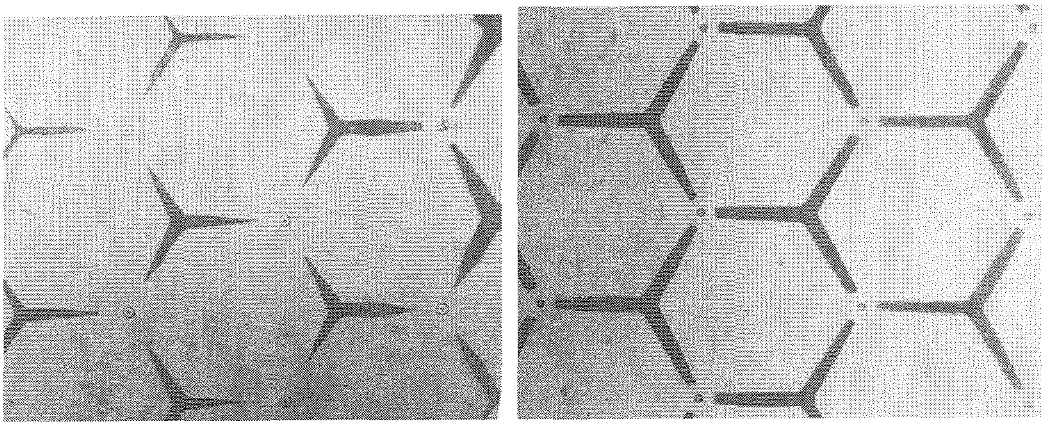

(a) $2\times10^{20}/cm^3$

(b) $8\times10^{20}/cm^3$

Figure 4-8 Pictures of Membranes Fabricated with Polysilicon Boron Doped Etch Stop

4-8 are the structures with different doping concentrations after TMAH etching. It can be seen that in Figure 4-8 (a) where doping concentration of $2\times10^{20}/cm^3$ was used, most of the structures were etched away by TMAH, while in Figure 4-8 (b), with doping concentration of $8\times10^{20}/cm^3$, the membrane structures were successfully made.

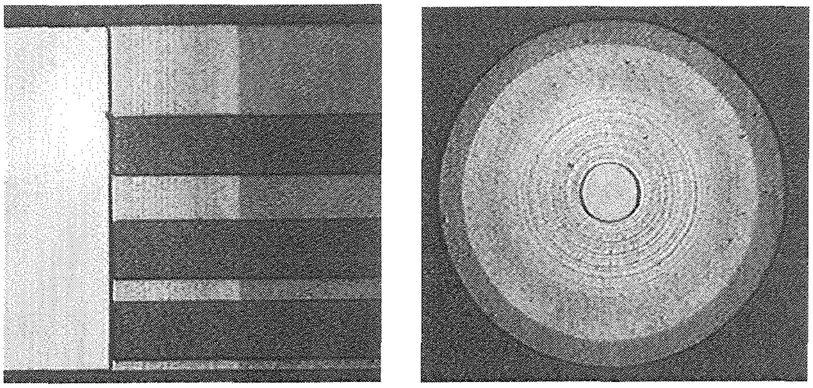

(a) Straight Channels (b) Circular Membranes

Figure 4-9 Polysilicon Sacrificial Etching Using BrF_3

4.2.4 Polysilicon Sacrificial Etching Using Bromine Trifluoride (BrF_3)

At room temperature, BrF_3 is in the form of a colorless to yellowish liquid with a vapor pressure of approximately 7.0 Torr. It was reported [11] that BrF_3 will spontaneously etch silicon in the vapor phase at room temperature. Compared to wet chemical etching, this process is completely dry and hence avoids structure stiction caused by surface tension force.

The polysilicon sacrificial etching using BrF_3 vapor was performed on the same testing structures. Figure 4-9 shows straight channels and circular membrane successfully released by BrF_3 vapor etching. A total length of 300 μm polysilicon sacrificial layer was etched away.

4.3 Cracking of Surface Micromachined Structures

With surface micromachining technology, many complex microstructures have been developed. However, it was found that sometimes during the final sacrificial layer etching, structures tend to crack. Because of this cracking, the yield of the fabrication is reduced dramatically, sometimes even to zero. Several possible mechanisms responsible for the cracking have been proposed. They are: (1) stress relaxation in the structural layer

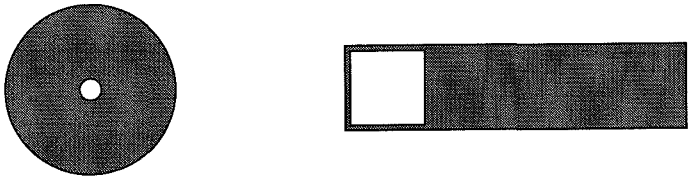

Type 1
Circular Membrane
Etched From the Center

Type 3
Straight Channel

Type 2
Circular Membrane
Etched From the Edge

Type 4
Square Membrane
Etched From the Corners

Figure 4-10 Cracking Test Structures

during the etching, (2) damage of the structural layer during the etching, and (3) sharp corners formed during the etching, which provide high stress concentration. A study of cracking of surface micromachined structures has been performed to find out which one of the three reasons is dominant so that guidelines can be drawn to help develop successful MEMS devices.

4.3.1 Design and Fabrication of Test Structures

Four types of test structures shown in Figure 4-10 have been designed and fabricated. Type 1 and Type 2 are circular membranes. Type 1 has the etching window in the center while the etching window of type 2 is on the periphery. The diameter of the circular membranes varies from 300 μm to 1 mm. Type 3 is a long straight channel with the etching window at one end. The width of the channel varies from 10 μm to 1 mm. Type 4 is a square membrane with etching windows on the corners. The side length of the square membrane varies from 300 μm to 1mm. The structures were fabricated using surface micromachining process. Silicon nitride was used as the structural layer while both PSG and polysilicon were used as the sacrificial layer with high concentration HF and TMAH as the corresponding etchants. In both cases, a 1 μm thick sacrificial layer was used. In order to find out how the thickness of the structural layer affects the cracking behavior, 0.5 μm and 1 μm thick structural layer were tried. In the case of PSG sacrificial layer, after the PSG layer was patterned, half of the wafers were annealed at 1050 °C for one hour to smooth the sharp corners formed during the PSG patterning process. Their cracking behavior was compared with one of the wafers without PSG annealing.

4.3.2 Experiments and Results

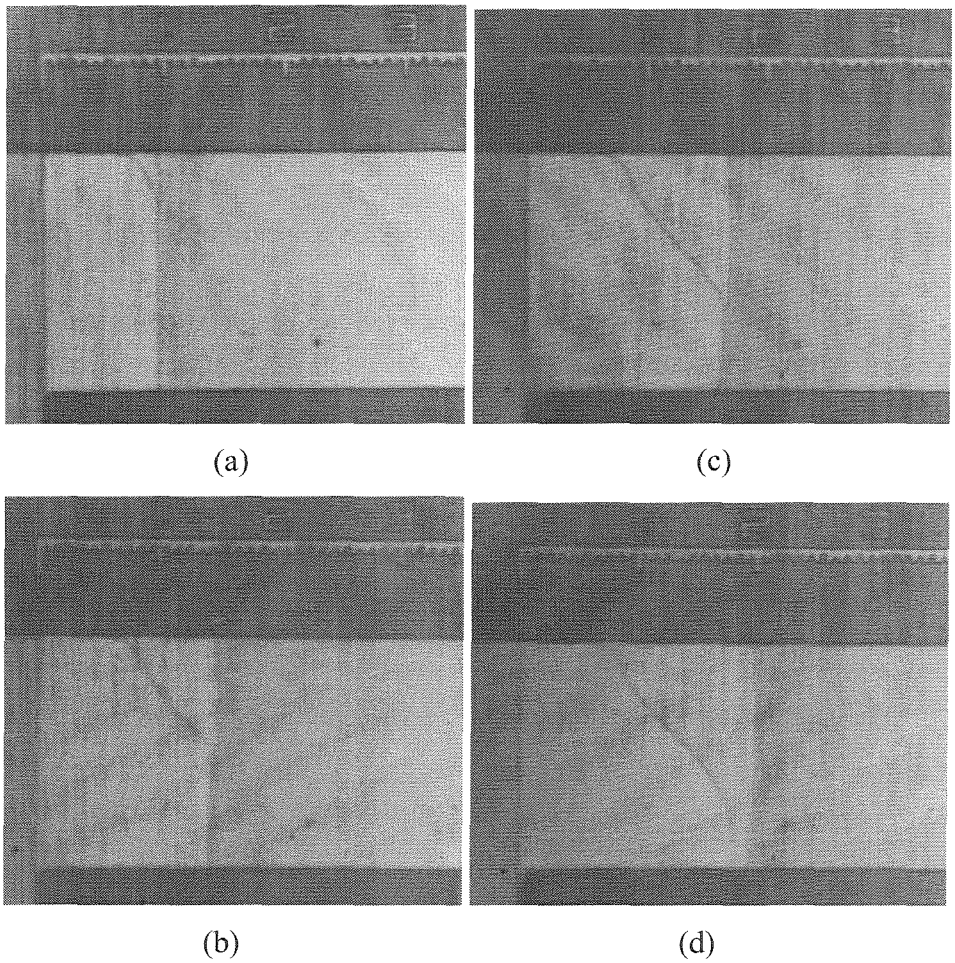
(a) (c)

(b) (d)

Figure 4-11 Sequential Pictures of Crack Propagation in a Channel

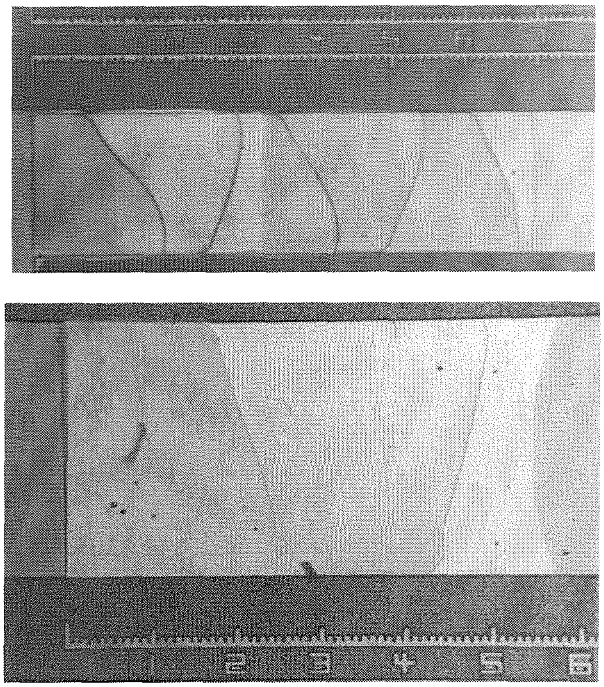

Figure 4-12 Pictures of Periodic Cracking Patterns in Straight Channels

In situ study of cracking of structures with polysilicon sacrificial layer was performed using the same setup shown in Figure 4-2. In the case of structures with PSG sacrificial layer, a container with transparent plastic cover was used to hold the HF solution. The samples were immersed in the solution and the container was put under microscope for observation. In both cases, the whole etching and structure cracking process were captured using a CCD camera and recorded using a VCR.

Experimentally, it was found that first, structures with polysilicon sacrificial layer etched by TMAH and structures with PSG sacrificial layer etched by HF had the same cracking behavior. Also, structures with annealed PSG layer and structures with unannealed PSG layer cracked in the same manner. Second, very few structures with 0.5 μm thick structural layer cracked. Third, all the circular membranes with diameters up to 1 mm did not crack no matter whether they were etched from the center (Type 1) or the periphery (Type 2). Straight channels (Type 3) with width smaller than 200 μm did not crack while channels wider than 200 μm cracked. Shown in Figure 4-11 are the sequential pictures of the crack propagation process in a straight channel. Usually, the

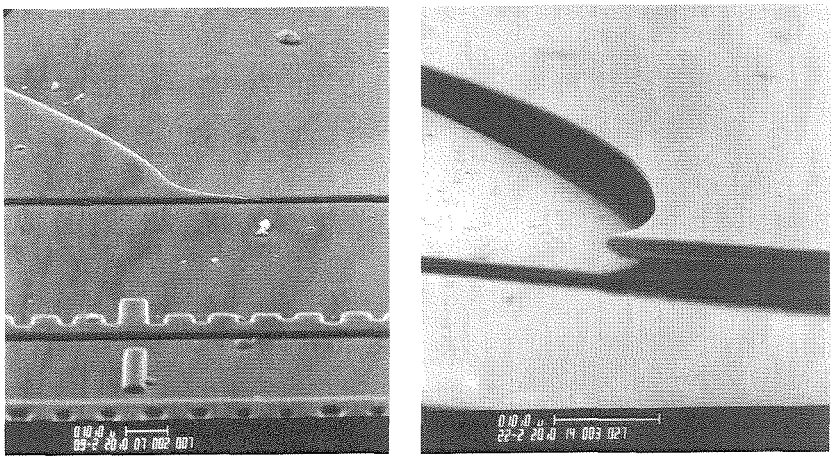

(a) (b)

Figure 4-13 Cracks at the Edge of the Channel

crack initiated at the edge of the channel (Figure 4-11 (a)) after a certain length of sacrificial layer was etched away. Then, the crack followed the etching front (Figure 4-11 (b)), propagated across the channel (Figure 4-11 (c)) and ended at the other edge (Figure 4-11 (d)) of the channel. After another certain length of etching, another crack started and propagated across the channel. Periodic cracking patterns formed when this etching and cracking process repeated. Figure 4-12 shows the periodic cracking patterns in straight channels. All the channels with a width from 200 μm to 1 mm had the similar periodic cracking pattern. Figure 4-13 shows the crack at the edge of the channel and that the cracked part of the channel was completely free from the substrate. All the square membranes (Type 4) cracked as shown in Figure 4-14. Similar cracking phenomena were observed during the square membrane etching. Cracks initiated at the edge of the membrane and followed the etching front. The sequential pictures of square membrane cracking are shown in Figure 4-15.

Finally, in the case of PSG etching, HF with different concentrations was also tried. Although the general cracking phenomena were the same, i.e., all the circular membranes did not crack and straight channels and square membranes cracked, the periodic cracking patterns were different. Many experiments with HF at concentrations of 10%, 20%, 30%, 40%, and 49% by weight were performed. Figure 4-16 shows some of

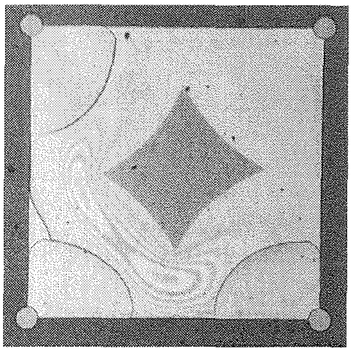

Figure 4-14 Cracking Patterns in a Square Membrane

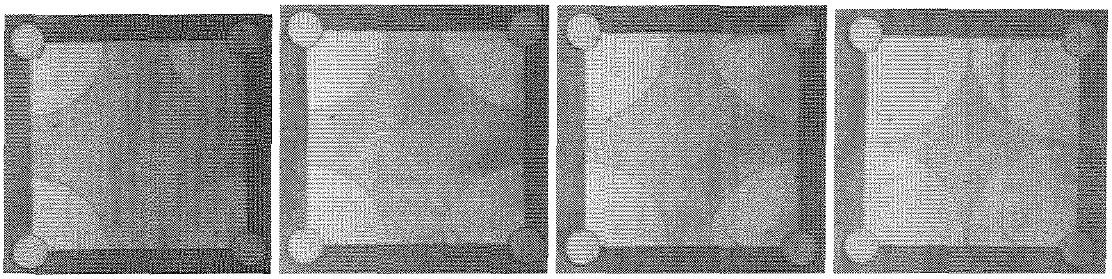

(a) (b) (c) (d)

Figure 4-15 Sequential Pictures of Crack Propagation in a Square Membrane

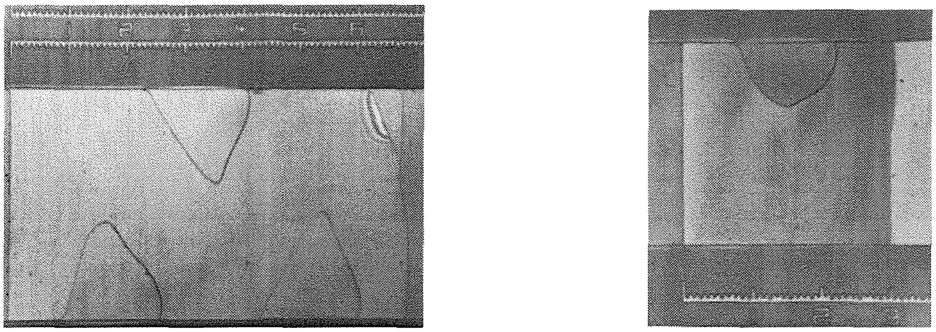

Figure 4-16 Cracking Patterns in Channels Etched Using Various HF Concentrations

the different cracking patterns produced at concentrations lower than 49%. From the experiments, it does not seem that there was a one-to-one corresponding relationship between a certain pattern and a certain HF concentration.

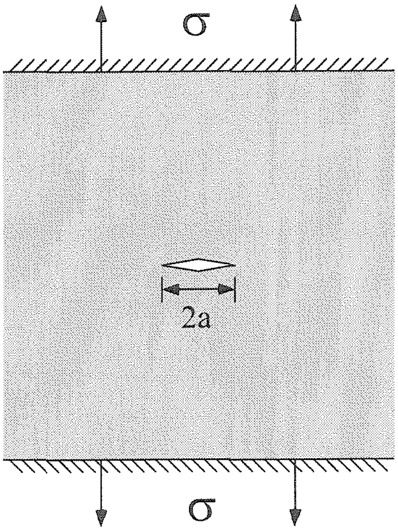

Figure 4-17 Griffith Criterion for Crack Growth

4.3.3 Explanation and Discussion

Some conclusions can be made based on the above experimental results. First, since annealing of the PSG sacrificial layer does not change the cracking behavior of the structures, high stress concentration around the sharp edge caused by the PSG patterning is not responsible for the cracking. Second, although high concentration HF etches silicon nitride at a nontrivial 50 – 60 Å/min, the fact that the cracking behavior does not depend on what sacrificial layer the structure uses excludes the possibility of cracking caused by HF etching of the silicon nitride layer.

It is generally accepted that LPCVD low-stress silicon-rich silicon nitride is a brittle material. The fracture mechanics of brittle materials was established by A. A. Griffith in 1921 [12,13]. Consider an infinite cracked plate of unit thickness with a central transverse crack of length 2a as shown in Figure 4-17. The plate is stressed to a stress, σ, and fixed at its ends. If the crack extends over a length da, the stiffness of the plate will drop and some load will be relaxed since the ends of the plate are fixed. Griffith pointed out that crack propagation would occur if the energy released upon crack growth is sufficient to provide all the energy that is required for crack growth. The condition for crack growth can be expressed as

$$\frac{dU}{da} = \frac{dW}{da} \qquad (4\text{-}2)$$

where

U: elastic energy,

W: energy required for crack growth.

In brittle material, W is simply the energy needed to create new surfaces. It should be noted that this energy criterion is only a necessary criterion for crack extension. In other words, even if sufficient energy for crack propagation can be provided, the crack will not propagate unless the material at the crack tip is ready to fail.

The cracking behavior in channels and square membranes can be qualitatively explained using this criterion. Consider the situation in long channels. As the etching progressed, the sacrificial layer was etched away and more and more strain energy stored in silicon nitride layer due to the residual stress from the deposition process became available to the crack extension. Using the wafer curvature technique, the stress in silicon nitride layer was measured to be tensile, 220 ± 40 MPa. After a certain length of etching, the available strain energy accumulated to such a critical value that the crack extension was thermodynamically favored. From the point of view of stress, the stress was relaxed in the free part of the structural layer during the etching. When the stress at some high concentration point, such as the edge of the channel, was large enough that the material was ready to fail, crack initiated. After the crack extended, the strain energy in the free part of the structural material was partially released. As the etching continued, the accumulation of the available strain energy started again. This accumulation and releasing process of strain energy in the structural layer was responsible for the periodic cracking patterns that were formed in the above channels. In the case of the circular membranes with etching windows at the center, although available strain energy also accumulated and crack extension was favored, the stress concentration at the etching window was not high enough to initiate the crack. We can conclude that it is the relaxation of residual stress in the structural layer that causes the cracking of channels and square membranes.

Based on the above qualitative explanation, several guidelines can be made to help fabricate surface micromachined devices. First, structures with small stress relaxation should be used to avoid the stress to exceed the fracture strength of the structural material. For example, instead of square membranes, circular ones or octagonal shaped ones should be used. In the case of channels, small step heights at the channel edge or even planarized channels should be used. Second, the strain energy in the structure layer should be reduced so that cracking is not thermodynamically favored. For example, the residual stress in structural material should be reduced as low as possible. As in the case of silicon nitride, increasing SiH_2Cl_2/NH_3 gas flow ratio and deposition temperature could reduce the tensile residual stress [8]. Third, since the strain energy in the structure is related to the volume and the shape of the structural layer, structures with less stored strain energy should be used. For example, several narrow channels should be used to replace a wide channel if this is allowed.

4.4 Strength of Surface Micromachined Membranes

Surface micromachined membranes have become one of the most important components in today's MEMS devices. The mechanical behavior of these membranes directly affects the performance of the MEMS devices. Of particular interest is their strength. For many applications such as pressure sensors, valves, and pumps, it is necessary to know how much pressure the membrane can sustain without bursting. Plate bending analysis [14] or finite element method is often used to solve this problem. Unfortunately, with standard surface micromachining fabrication processes, the membrane has step-up anchors at the edge. Several research groups [1,15] have reported that it is not accurate to model this step-up anchor as a "fixed" boundary condition. Efforts have been made to theoretically model such a boundary condition [16,17]. Also, L. V. Ngo [18] proposed a simple mask modification technique to minimize this step-up effect. Here, a new technique [19,20] which does not require a change of mask design or fabrication process is proposed to improve the step-up boundary condition. The strength of surface micromachined membranes with different boundary conditions has been experimentally studied and

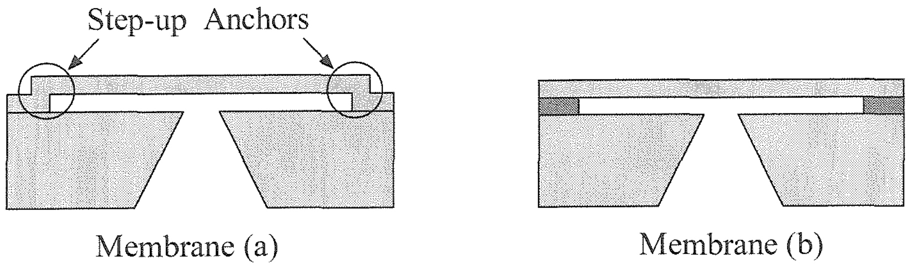

(a) Common surface micromachined membranes have step-up anchors.

(b) Step-up anchors can be eliminated if the sacrificial layer is not patterned.

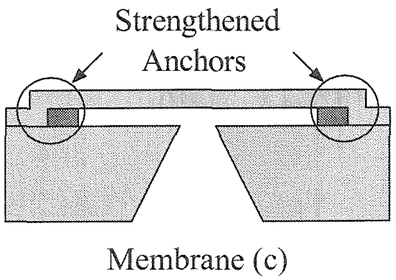

(c) The anchors can be strengthened with an extra sacrificial rim.

Figure 4-18 Surface Micromachined Membranes with Various Boundary Conditions

compared using burst pressure testing. This technique can be applied to other surface micromachined structures.

4.4.1 Design and Fabrication of Test Structures

As shown in Figure 4-18 (a), the typical surface micromachined membrane has a step-up anchor at the boundary. When load is applied to the membrane, the step-up anchor becomes the high stress concentration point and significantly affects the strength of the membrane. Such a membrane usually bursts at low load. To improve the membrane strength, the effect of the step-up boundary condition has to be minimized. One way to achieve this is shown in Figure 4-18 (b). In order to avoid the step-up boundary, the sacrificial layer is not patterned. The size of the membrane is determined by the final sacrificial layer etching process. Unfortunately, many other surface micromachined structures can not be fabricated using this method. The application of such membranes is limited. Here, a new technique, which does not require changes in the mask or the fabrication process, is proposed. As shown in Figure 4-18 (c), instead of etching the sacrificial layer completely, a sacrificial layer rim with certain width is left unetched on purpose. In this way, the step-up boundary condition will be modified to approach the ideal boundary condition. The membrane should be able to stand higher pressure compared to the membrane with the step-up boundary condition. Since there is no major change in the fabrication process, it is still feasible to fabricate most surface micromachined structures in this manner.

Circular membranes with diameters of 200 μm, 300 μm, 400 μm, 500 μm, 600 μm, and 800 μm and three different boundary conditions have been designed and fabricated using surface micromachining technology. LPCVD low-stress, silicon-rich silicon nitride has been chosen as the structural material. Both phosphosilicate glass (PSG) and polysilicon have been tried as the sacrificial layer with high concentration hydrofluoric acid (HF) and tetramethylammonium hydroxide (TMAH) as the corresponding etchants. However, it is found that the polysilicon/TMAH scheme is more favorable for the reasons mentioned in Section 4.3. First, TMAH has an extremely low etch rate of silicon nitride while 49% HF etches silicon nitride at the rate of 50-60 Å/min. When etching for extended periods of time, a significant amount of silicon nitride will be etched away. Second, in the case of PSG, in order to achieve the boundary condition in Figure 4-18 (c), the PSG etching process has to be timed [5] so that a PSG rim with certain width is left at the edge. This process can be tedious and the etching uniformity is difficult to control. For polysilicon, polysilicon heavily doped with boron can be an etch stop in TMAH. By using boron doped polysilicon as the sacrificial rim, the proposed boundary conditions can be easily achieved and the releasing process is greatly simplified.

The fabrication process started with the deposition and patterning of a 1 μm thick sacrificial layer (PSG or polysilicon). Then, in the case of PSG, the PSG layer was reflowed at 1050 °C for 1 hour to smooth the sharp etched corners. In the case of polysilicon, a layer of 1 μm LPCVD silicon oxide was deposited and patterned, followed by boron ion implantation with a dose of $4 \times 10^{16}/\text{cm}^2$ and 30 minutes annealing at

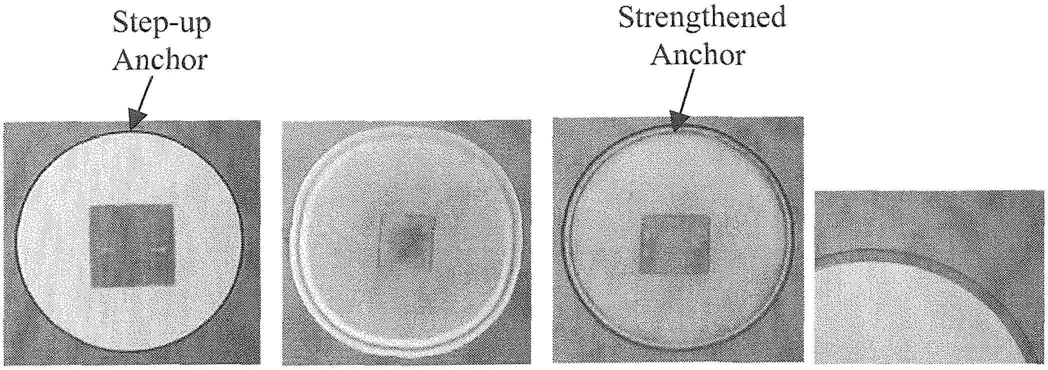

Membrane (a) Membrane (b) Membrane (c)

Figure 4-19 Pictures of Fabricated Membranes with Various Boundary Conditions

1100 °C to activate and drive in the dopants. The silicon oxide serves as the ion implantation mask and was removed afterwards. After that, a 1 μm thick LPCVD silicon nitride layer was deposited. Windows on the wafer back side are opened and the wafers were etched in KOH to create the back holes. Finally, the wafers were immersed in HF (49%) or TMAH (10%, 90 °C) to etch away the sacrificial layer and free the membranes. The membrane with the proposed boundary condition (membrane (c) in Figure 4-18) was fabricated in a similar way except that the final PSG etching was timed to form an extra 20 μm wide PSG rim. The third membrane (membrane (b) in Figure 4-18) was also fabricated in the similar way except there was no patterning of the sacrificial layer. Shown in Figure 4-19 were pictures of the fabricated membranes.

4.4.2 Testing

The strength of the membranes was measured using burst pressure testing. Pneumatic pressure was applied to the membrane from the back side of the chip. The pressure was increased slowly until the membrane bursts. The pressure at the burst point was recorded from the pressure gauge. The burst was monitored under the microscope. It was found that membranes (b) and (c) can stand higher pressure than membrane (a). No appreciable difference in burst pressure between membrane (b) and membrane (c) has been found.

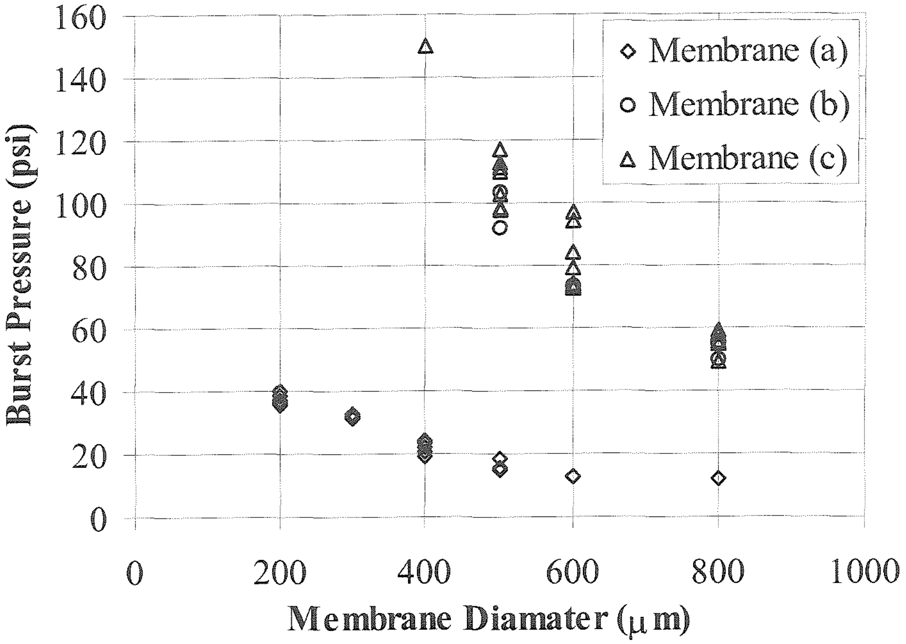

Figure 4-20 Burst Testing Results

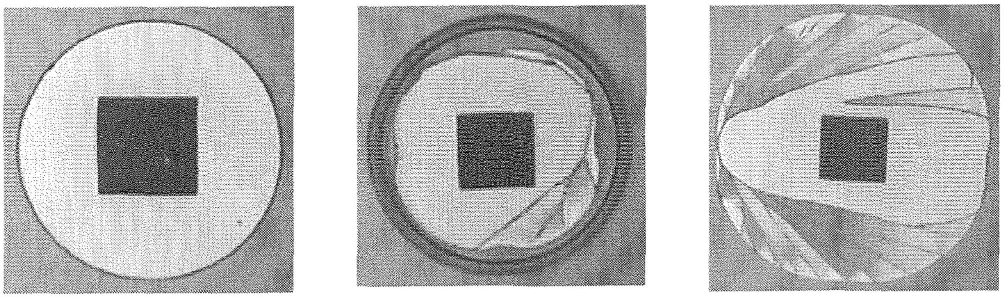

Membrane (a)

Membrane (b)

Membrane (c)

Figure 4-21 Pictures of Burst Membranes

Figure 4-20 shows the testing results. Membrane (a) with a diameter of 400 μm bursts in the range from 19 psi to 24.1 psi, but membranes (b) or (c) with the same size do not burst, even at 150 psi which is the pressure limit of our testing setup. We can not burst any membrane (b) or (c) with diameters smaller than 400 μm because of this limit.

The burst patterns of the membranes are shown in Figure 4-21. As expected, it clearly shows that membrane (a) bursts at the step-up boundary because of its high stress concentration. With the new boundary conditions, the burst patterns suggest that the membrane (b) and (c) burst somewhere from the center of the membrane, which has the highest stress. This is in agreement with plate stress analysis using ideal fixed boundary conditions [14].

4.4.3 Applications

This technique can be applied to improve the boundary conditions of other surface micromachined structures. For example, with the new boundary conditions, the strength of the cantilever or double support beams (Figure 4-22) can be improved and modeling of the mechanical performance can be more accurate [18]. This technique is also used to develop surface micromachined bellows which will be described in Chapter 5.

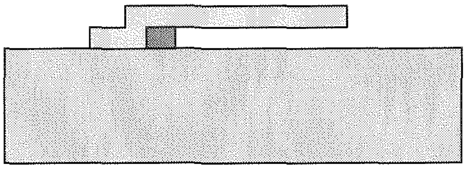

Figure 4-22 Cantilever Beam with Strengthened Anchors

4.5 Conclusion

Three key technologies for microbellows design and fabrication have been studied. First, LPCVD polysilicon has been explored as the sacrificial layer for surface micromachined process. Channels and membranes have been designed and fabricated, and etch rates of the polysilicon sacrificial layer in TMAH under various conditions have been calibrated. Etch stop characteristics of heavily boron doped polysilicon in TMAH has also been explored. Good etch stop has been achieved with a boron doping concentration of $8\times10^{20}/\text{cm}^3$. Polysilicon sacrificial layer etching using gas-phase BrF_3 has also been tried. This vapor etching is tension free and hence completely avoids the problem of structure stiction. Second, the cracking of surface micromachined structures during the final freeing process has been studied. Straight channels and circular and square membranes have been designed, fabricated, and tested. The cracking behavior can be qualitatively explained using the Griffith criterion. It is found that relaxation of residual stress in the structural layer is responsible for the structure cracking. Several guidelines for successful MEMS devices design and fabrication are provided based on this analysis. Finally, the strength of surface micromachined membranes is experimentally studied. It is found that the membrane strength strongly depends on the membrane boundary conditions. A new fabrication technique that does not requires changing the existing mask and fabrication process is proposed to improve the common step-up boundary condition. Membranes with diameters from 200 μm to 800 μm and three different boundary conditions have been fabricated and tested. The application of this technique to other surface micromachined structures such as cantilever beams is also described.

Bibliography

[1] R. T. Howe and R. S. Muller, "Polycrystalline Silicon Micromechanical Beams," Journal of Electrochemical Society, Vol. 130, pp. 1420-1423, 1983.

[2] L. S. Fan, Y. C. Tai, and R. S. Muller, "Integrated Movable Micromechanical Structures for Sensors and Actuators," IEEE Transactions on Electron Devices, Vol. ED-35 (6), pp. 724-730, June 1988.

[3] Y. C. Tai, *IC-Processed Polysilicon Micromechanics: Technology, Materials and Devices*, Ph.D. Thesis, University of California, Berkeley, 1989.

[4] W. C. Tang, T.-C. H. Nguyen, and R. T. Howe, "Laterally Driven Polysilicon Resonant Microstructures," Proceedings of IEEE Workshop on Micro Electro Mechanical Systems (MEMS'89), pp. 53-59, Salt Lake City, USA, February 1989.

[5] J. Q. Liu, Y. C. Tai, J. Lee, K. C. Pong, Y. Zohar, and C. M. Ho, "*In Situ* Monitoring and Universal Modeling of Sacrificial PSG Etching Using Hydrofluoric Acid," Proceedings of IEEE Workshop on Micro Electro Mechanical Systems (MEMS '93), pp. 71-76, Fort Lauderdale, USA, February 1993.

[6] C. H. Mastrangelo and C. H. Hsu, "Mechanical Stability and Adhesion of Microstructures under Capillary Forces – Part I, II," Journal of Microelectromechanical Systems, Vol. 2, pp. 30-55, 1993.

[7] O. Tabata, H. Funabashi, K. Shimaoka, R. Asahi, and S. Sugiyama, "Surface Micromachining Using Polysilicon Sacrificial Layer," Proceedings of International Symposium on Micromachine and Human Science, pp. 163-172, Nagoya, Japan, October 1991.

[8] M. Sekimoto, H. Yoshihara, and T. Ohkubo, "Silicon Nitride Single-Layer X-Ray Mask," Journal of Vacuum Science and Technology, Vol. 21(4), pp. 1017-1021, November/December 1982.

[9] O. Tabata, R. Asahi, H. Funabashi, K. Shimaoka, and S. Sugiyama, "Anisotropic Etching of Silicon in TMAH Solutions," Sensors and Actuators (A: Physical), Vol. 34, pp. 51-57, 1992.

[10] S. Sugiyama, T. Suzuki, K. Kawahata, K. Shimaoka, M. Takigawa, and I. Igarashi, "Micro-Diaphragm Pressure Sensor," Proceedings of IEEE International Electron Devices Meeting, pp. 184-187, Los Angeles, USA, December 1986.

[11] X. Q. Wang, X. Yang, K. Walsh, and Y. C. Tai, "Gas Phase Silicon Etching with Bromine Trifluoride," Technical Digest, International Conference on Solid-State Sensors and Actuators (Transducers'97), Vol. 2, pp. 1046-1415, Chicago, USA, June 1997.

[12] A. A. Griffith, "The Phenomena of Rupture and Flow in Solids," Philosophical Transactions of the Royal Society Of London, A 221, pp. 163-197, 1921.

[13] A. A. Griffith, "The Theory of Rupture," Proceedings of 1st International Congress Applied Mechanics, pp. 55-63, 1925.

[14] S. Timoshenko and S. Woinowsky-Krieger, *Theory of Plates and Shells*, McGraw-Hill, New York, 1959.

[15] H. Guckel, T. Randazzo, and D. W. Burns, "A Simple Technique For the Determination of Mechanical Strain in Thin-Films with Applications to Polysilicon," Journal of Applied Physics, 57, 1671 (1985).

[16] R. L. Mullen, M. Mehregany, M. P. Omar, and W. H. Ko, "Theoretical Modeling of Boundary Conditions in Microfabricated Beams," Proceedings of IEEE Workshop on Micro Electro Mechanical Systems (MEMS'91), pp. 154-159, Nara, Japan, February 1991.

[17] Q. Meng, M. Mehregany, and R. L. Mullen, "Analytical Modeling of Step-up Supports in Surface-Micromachined Beams," Technical Digest, International Conference on Solid-State Sensors and Actuators (Transducers'93), pp. 779-782, Yokohama, Japan, June 1993.

[18] L. V. Ngo, P. Nelson, and C.-J. Kim, "Surface-Micromachined Beams Without Spring Effect of Anchor Step-up," Technical Digest, Solid-State Sensor and Actuator Workshop (Hilton Head'96), pp. 140-143, Hilton Head Island, South Carolina, USA, June 1996.

[19] X. Yang and Y. C. Tai, “Improved Boundary Conditions of Surface Micromachined Diaphragms,” Micromachining Workshop III, Southern California Chapter of American Vacuum Society, Anaheim, California, USA, September 1996.

[20] X. Yang, F. M. Siu, and Y. C. Tai, "Strength of Surface Micromachined Diaphragms," MRS Spring Meeting, Symposium N: Microelectromechanical Structures for Material Research, San Francisco, California, USA, April 1998.

Chapter 5

Microbellow Actuator

5.1 Introduction

Silicon membranes are widely used as the actuator structure in many MEMS devices. In many applications such as in valves and pumps [1], large deflection is desired. However, as pointed out in Chapter 3, flat silicon membranes have limited realizable deflections which restricts most microvalves to low flow applications. To achieve large deflections then requires large membrane sizes. For many applications, it is advantageous to have large deflections and small size at the same time. Efforts have been made to achieve this. For example, corrugated membrane structures have been studied to improve the large deflection performance [2]. Here, a new micromachined mechanical structure, the microbellow actuator, is proposed to achieve small size and large deflection simultaneously. Figure 5-1 shows a conceptual 3-D cross-sectional view of a microbellow actuator. Basically, the microbellow is a multi-layer mechanical structure. When it is actuated, every layer in the microbellow moves upward and the total deflection of the microbellow will be much larger than the deflection of a single flat membrane with the same dimensions.

5.2 First Generation Microbellows

There are many possible ways to fabricate microbellows. Among them, surface micromachining technology is chosen for two reasons. At the time this device was developed, surface micromachining had been well studied. More importantly, the thin

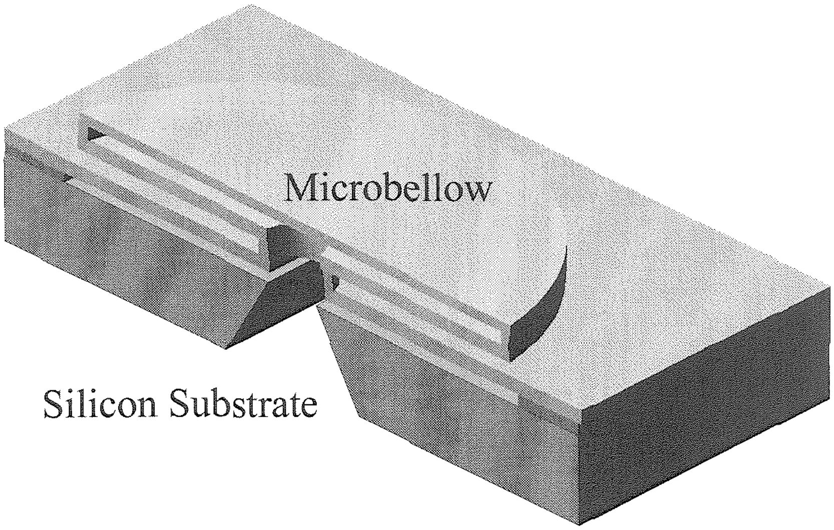

Figure 5-1 Conceptual 3-D Cross-Sectional View of Microbellows

film materials involved in the surface micromachining process, such as polysilicon and silicon nitride, were found to have excellent mechanical properties. For microbellows, both polysilicon and silicon nitride can be used as the structural layer while PSG is the sacrificial layer. It was reported [3] that polysilicon has a Young's modulus of ~130 GPa and fracture strain of ~1%. Although, compared to polysilicon, silicon nitride is much stiffer and has a Young's modulus of ~350 GPa, it is supposed to have much higher fracture strain, which means structures made of silicon nitride should be much stronger than the ones made of polysilicon. For this reason, silicon nitride was chosen to be the structural material for microbellows. In the first attempt, two-layer microbellows were designed and fabricated to study the feasibility of microbellows. Also, in the same design, bridge-slider structures were designed, fabricated, and tested to measure the fracture strain of silicon nitride.

5.2.1 Fracture Strain of Silicon Nitride

By using a bridge-slider structure, Y. C. Tai developed a novel and convenient method to study the ultimate fracture strain of polysilicon [4]. The same method is applied here to

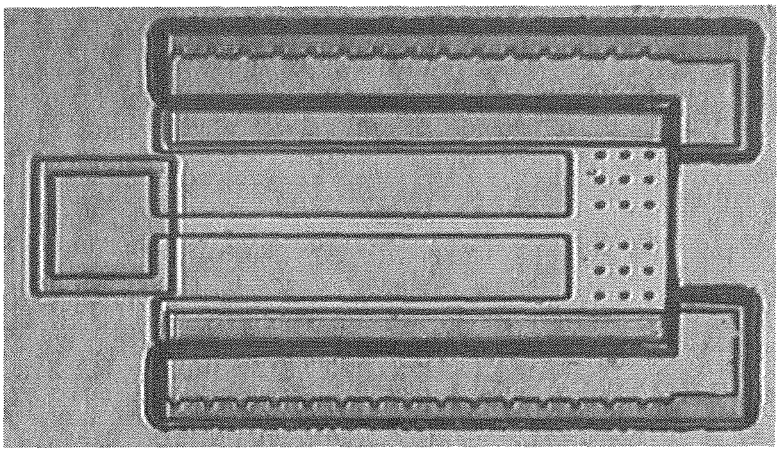

Figure 5-2 Picture of a Bridge-Slider Structure for Fracture Strain Measurement

LPCVD low stress silicon nitride. Shown in Figure 5-2 is a picture of a fabricated bridge-slider structure. The fabrication process will be described in the following Section 5.2.2. Basically, the free-standing bridge has two ends. The right end is anchored to the silicon substrate, while the left end is connected to a sliding plate guided by two flanges. The outer edge of the slider flanges are sawtooth shaped to provide scales for locating the end of the slider during the experiments.

Figure 5-3 demonstrates the experiment. By pushing the slider with a mechanical

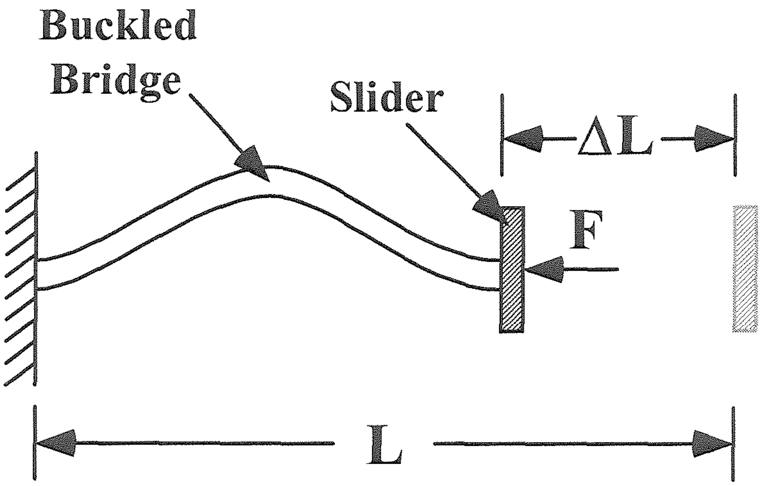

Figure 5-3 Schematic Side View of a Bridge-Slider for Fracture Strain Measurement Experiment

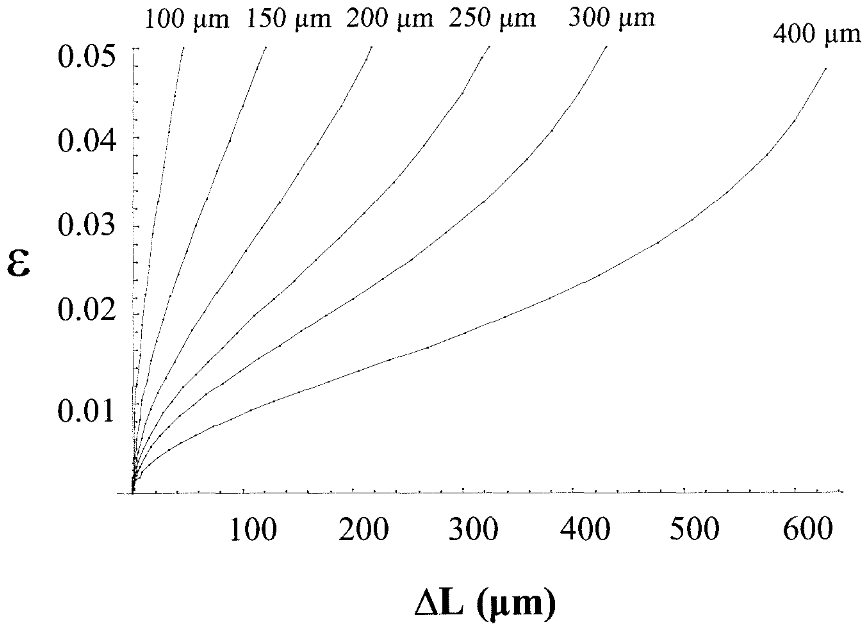

Figure 5-4 Theoretical Calculations of ε(ΔL)

probe, an initially straight bridge became increasingly buckled and eventually it fractured. Pushing was done on a probe station under an optical microscope and the whole procedure was video-taped to provide a record. Since the edges of the flanges were shaped with sawtooth scales, the maximum distance ΔL that the slider could be pushed was easily measured. It was shown in [4] that by using nonlinear beam bending theory, the relationship between ε and ΔL can be obtained by solving the following two equations.

$$\varepsilon = 4pK(p)\frac{t}{L} - \frac{4}{3}K^2(p)\left(\frac{t}{L}\right)^2 \tag{5-1}$$

$$\frac{L-\Delta L}{L} = \frac{L}{4}\left[\frac{2E(p)}{K(p)} - 1\right] \tag{5-2}$$

Where

ε: fracture strain,

p: dummy variable,

Table 5-1 Experimental Results

L/*w*/*t* (μm/μm/μm)	ΔL (μm)	ε (%)
100/6/1.2	25, 31, 31,	3.5, 4.0, 4.0,
150/6/1.2	73, 66, 61, 61,	3.5, 3.3, 3.1,
200/6/1.2	118, 111, 111, 105	3.0, 2.9, 2.9, 2.8,
250/6/1.2	170, 164,	2.7, 2.6,
300/6/1.2	234, 254,	2.5, 2.6,
100/10/1.2	31, 31, 31, 31,	4.0, 4.0, 4.0, 4.0,
150/10/1.2	46,	1.6,
200/10/1.2	118, 118, 98,	3.0, 3.0, 2.7,
250/10/1.2	168, 170, 183,	2.6, 2.7, 2.8,
300/10/1.2	268, 240, 248,	2.8, 2.5, 2.6,
100/20/1.2	25, 31, 31, 31, 31,	3.5, 4.0, 4.0, 4.0, 4.0,
150/20/1.2	66, 79, 61, 79, 61,	3.3, 3.7, 3.1, 3.7, 3.3,
200/20/1.2	118, 111, 111, 98,	3.0, 2.9, 2.9, 2.7,
250/20/1.2	181, 201, 162,	2.8, 3.0, 2.6,
300/20/1.2	281, 254, 163,	2.9, 2.6, 2.6,

t: thickness of the bridge,

L: length of the bridge,

ΔL: the maximum distance the bridge can be pushed before the bridge fractures.

And, K(p) and E(p) are complete elliptic integrals of the first and second kind respectively. They are defined as follows.

$$K(p) = \int_0^{\pi/2} (1 - p^2 \sin^2 \phi)^{-1/2} d\phi \tag{5-3}$$

$$E(p) = \int_0^{\pi/2} (1 - p^2 \sin^2 \phi)^{1/2} \, d\phi \tag{5-4}$$

Bridges with widths of 6 μm, 10 μm, and 20 μm and lengths of 100 μm, 150 μm, 200 μm, 250 μm, 300 μm, and 400 μm were designed, fabricated, and tested. All the bridges are 1.2 μm thick. Theoretically, $\varepsilon(\Delta L)$ should be independent of the bridge width. By changing the bridge length, $\varepsilon(\Delta L)$ calculated from Equation (5-1) and (5-2) are plotted in Figure 5-4. The experimental results are shown in Table 5-1. First, the 400 μm long bridge did not fracture. Second, it is true that $\varepsilon(\Delta L)$ is not a function of bridge width. Third, the average of all the measurements in Table 5-1 is ~ 2.8%. This is almost three times of fracture strain of polysilicon. This confirms that silicon nitride is a much stronger material than polysilicon and it is chosen as the structural material for the microbellows.

5.2.2 Two-Layer Microbellows

Two-layer microbellows were fabricated using surface micromachining technology with

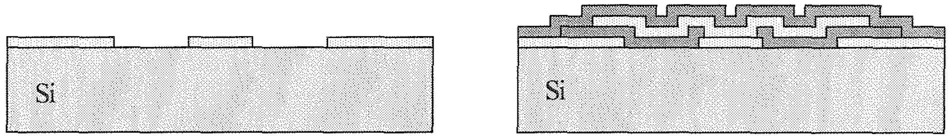

(a) 1st PSG Deposition and Patterning

(d) 2nd SiN Deposition

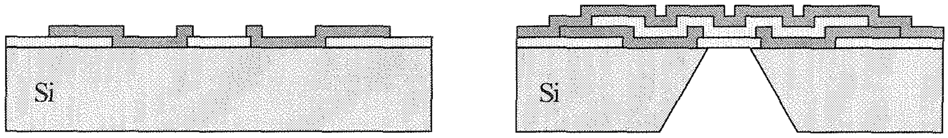

(b) 1st SiN Deposition and Patterning

(e) Back Side KOH Etching

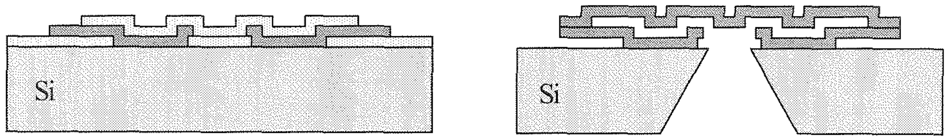

(c) 2nd PSG Deposition and Patterning

(f) 2nd SiN Patterning and HF Releasing

Figure 5-5 Two-Layer Microbellows Fabrication Process

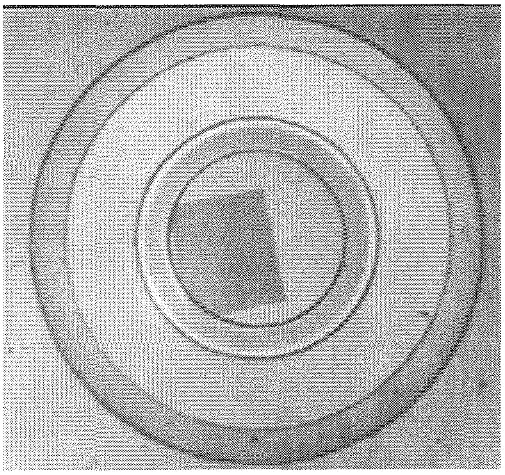

Figure 5-6 Picture of Fabricated Two-Layer Microbellows

silicon nitride as structural layer and PSG as sacrificial layer. The fabrication process is shown in Figure 5-5. First, a layer of 1 μm thick LPCVD PSG was deposited at 450 °C and patterned to define the sacrificial layer between the first structural layer and the substrate. The wafers were then annealed at 1050 °C for 1 hour to smooth the sharp corners in PSG layer formed during the PSG patterning process. A layer of 1.2 μm thick LPCVD silicon nitride was deposited at 820 °C with SiH_2Cl_2/NH_3 gas flow ratio 4/1 and patterned to define the first structural layer in the microbellows. After that, another layer of 1 μm thick PSG was deposited under the same condition and patterned, followed by the same annealing step as above. This PSG layer served as the sacrificial layer between the first and second structural layer in the microbellows. A final layer of 1.2 μm thick silicon nitride was deposited under the same conditions. Etching windows were opened on the back side of the wafers using SF_6/O_2 plasma and the wafers were then put into the KOH solution to create access holes to the microbellows on the front side of the wafers. After that, the second layer of silicon nitride on the front side was patterned. Finally, the microbellows were freed by etching away the PSG sacrificial layer in high concentration HF.

Shown in Figure 5-6 is a fabricated two-layer microbellow with diameter of 400 μm. The square access hole from back side is off-centered due to misalignment between front side and back side of the wafer. During the final HF freeing process, it was

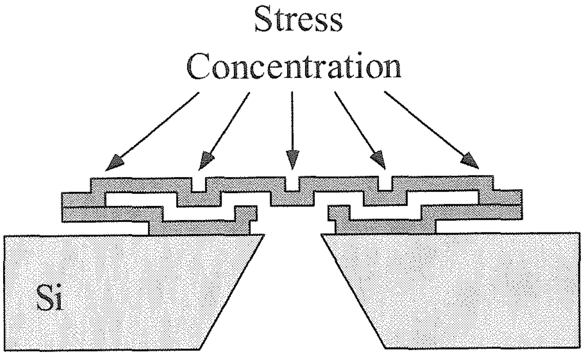

Figure 5-7 Stress Concentration in Two-Layer Microbellows

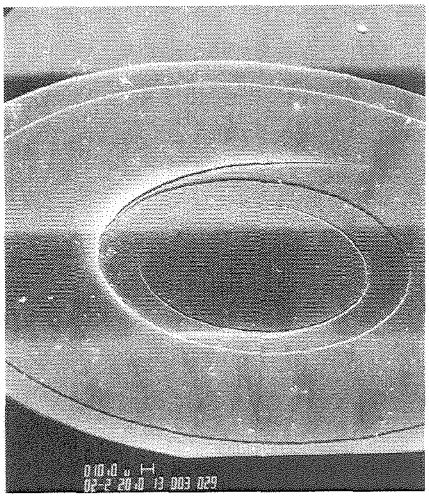

Figure 5-8 SEM Picture of Cracked Microbellows

found that most of the microbellows cracked and the yield of the process was very low. The cracked microbellows were extensively studied under microscope and SEM. The results showed that most of them cracked from the center of the top silicon nitride layer which has many step-up anchors as can be seen from Figure 5-7 and 5-8. As explained in Chapter 4, two mechanisms were responsible for the cracking. First, there was high residual stress in the silicon nitride layer. Second, the step-up anchors in the top silicon nitride created high stress concentration after the structure was freed. To solve these problems, high silicon nitride deposition temperature should be used to reduce the residual stress [5] and new strengthened or planarized anchors should be made to reduce stress concentration.

5.3 Second Generation Microbellows

In order to achieve higher deflection, a three-layer structure was used for the second generation microbellows. The microbellows were also fabricated using surface micromachining technology. LPCVD low-stress silicon-rich silicon nitride was still the

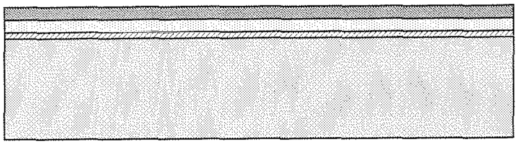

(a) Thermal Oxidation, Deposition of 1st Poly-Si and 1st SiN

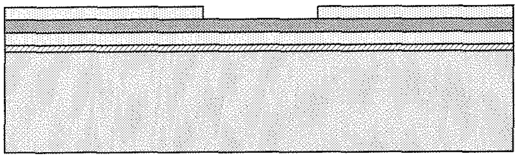

(b) Deposition and Patterning of 2nd Poly-Si

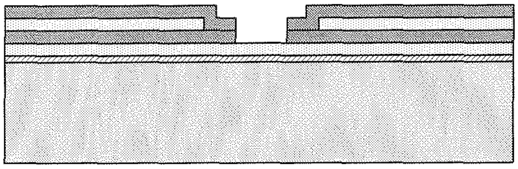

(c) Deposition and Patterning of 2nd SiN

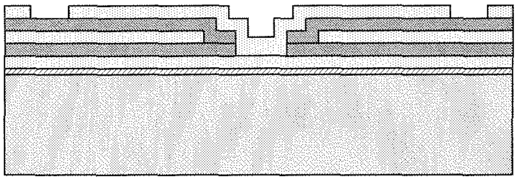

(d) Deposition and Patterning of 3rd Poly-Si

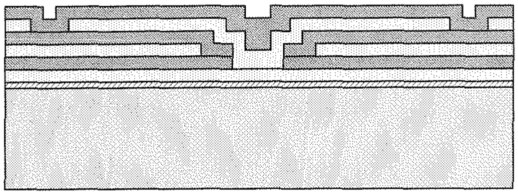

(e) Deposition of 3rd SiN

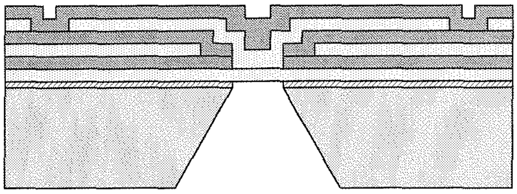

(f) Back Side KOH Etching

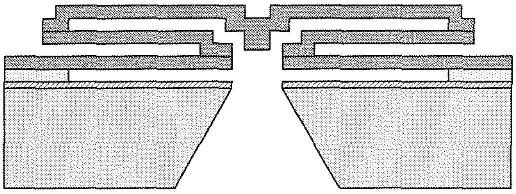

(g) 3rd SiN Patterning and Final TMAH Releasing

Figure 5-9 Three-Layer Microbellows Fabrication Process

structural layer. However, undoped LPCVD polysilicon was chosen to be the sacrificial layer for the reasons mentioned in Chapter 4.

5.3.1 Three-Layer Microbellows

Three-layer microbellows with diameters of 400 μm, 600 μm, and 800 μm have been designed and fabricated. The fabrication process is shown in Figure 5-9. First, a layer of 0.5 μm thick thermal oxide was grown on the silicon substrate to protect it from the later sacrificial TMAH etching. Then, the first 1 μm thick LPCVD undoped polysilicon sacrificial layer was deposited at 624 °C followed by 1.2 μm thick LPCVD silicon nitride structural layer deposited at 850 °C with SiH_2Cl_2/NH_3 gas flow ratio 4/1. The second

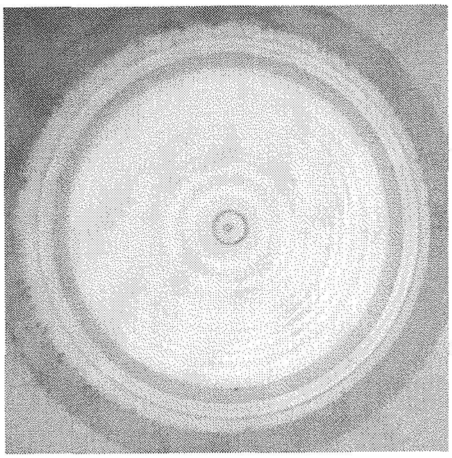

Figure 5-10 Picture of a Fabricated Three-Layer Microbellows

1 μm thick polysilicon layer was deposited and patterned to open the contact windows between the first and second layer of the microbellow. After that, the second 1.2 μm thick silicon nitride layer was deposited and patterned to define the second layer of the microbellow. The same process was then repeated for the third layer of the microbellows. After the microbellow was defined, windows were then opened on the back side of the wafers by KOH etching. Finally, wafers were immersed into 10% TMAH solution at 90 °C to etch away the polysilicon sacrificial layers to free the microbellows.

Figure 5-10 shows the top view of a fabricated 600 μm diameter three-layer microbellow.

5.3.2 Strength of Microbellows

One of the most important performance parameters of microbellows is their strength. Burst pressure experiments were performed on many microbellows to find out how much pressure microbellows can sustain before they fail. The experimental setup is shown in Figure 5-12. Pneumatic pressure was applied to the microbellow from the back side of the chip. The pressure was increased slowly until the microbellow burst. The pressure at the burst point was recorded from the pressure gauge. The whole burst process was monitored under the microscope. It is found from the experiments that these

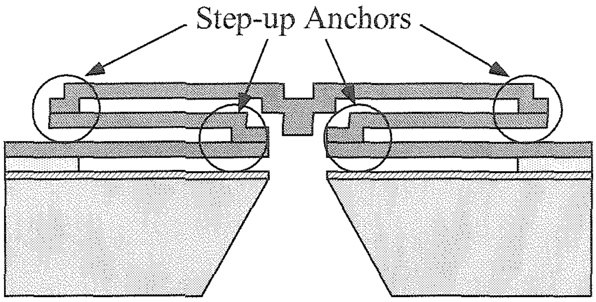

(a) Microbellow with Step-up Anchors

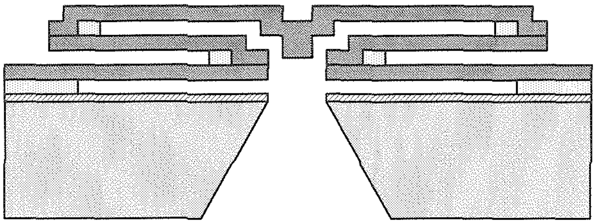

(b) Microbellow with Strengthened Anchors

Figure 5-11 Anchor Structures of Microbellows

microbellows have rather low burst pressures (Table 5-2). The reason is that the completely freed microbellow has step-up anchors at the places where the structural layers join each other (Figure 5-11(a)). When pressure load is applied to the microbellow, these step-up anchors become stress concentration points and the microbellow tends to burst there. As described in Chapter 4, the step-up anchors can be strengthened by leaving a block of sacrificial layer near the edges where the two structural layers are joined together (Figure 5-11(b)). To achieve this in fabrication, either timed etching of polysilicon or boron doped polysilicon etch stop can be used. In the timed etching process, it was found that, although there is constant generation of hydrogen bubbles during the etching, the etching fronts are still circular if the etching windows are small and circular. The etching process was monitored and precisely time-controlled so that a 20 μm wide sacrificial layer rim was left at all joints. Compared to the timed etching process, the boron doped polysilicon process described in Section 4-2-3 is more reliable and easier to control and it can produce the same anchor structure in Figure 5-11(b). The

Table 5-2 Burst Pressure of Microbellows and Membranes

Diameter (μm)	400	600	800
Single Flat Membrane	150 psi	75 psi	57 psi
Microbellow with Step-up Anchors	23 psi	14 psi	12 psi
Microbellows with Strengthened Anchors	130 psi	72 psi	53 psi

microbellow shown in Figure 5-10 has the strengthened anchor structures fabricated using the boron doped etch stop process. Experimentally, the strength of microbellows with the strengthened anchors was tested. In comparison, the strength of a flat membrane was also tested. Table 5-2 shows the burst pressure of both kinds of microbellows with and without strengthened anchors and the strength of flat silicon nitride membranes. It shows that the microbellows with strengthened anchors have almost the same strength as the flat membranes and they burst at 5 times higher pressure than the microbellows without strengthened anchors. It is believed that the joints with the polysilicon rims have greatly reduced stress concentration. The results show that the new anchor structure can greatly improve the strength of the microbellow without changing its dimensions and affecting its deflection performance.

5.3.3 Load-Deflection Testing of Microbellows

Load-deflection tests were then performed on the microbellows with the testing setup shown in Figure 5-12. The microbellows were actuated pneumatically by applying pressure from the back side windows and the corresponding deflections were measured

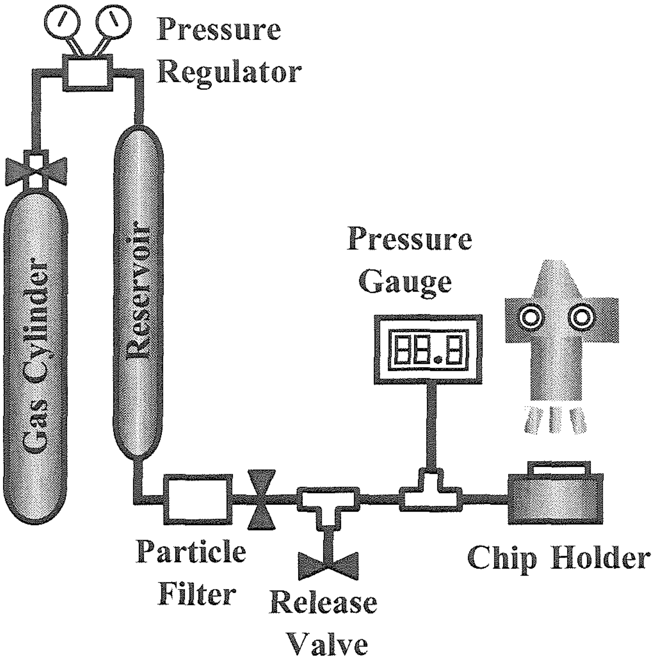

Figure 5-12 Load-Deflection Testing Setup

under an optical microscope with a calibrated focus adjustment. The microbellow to be tested was mounted and sealed on a special chip holder and was then placed on the x-y stage of an optical microscope with z-direction focus adjustment calibrated in 1 μm increments. Compressed nitrogen was used as the pressure source. The pressure level was controlled by the regulator and monitored by the commercial pressure gauge (Omega HHP 4100). By adjusting the input pressure and focus position, the center deflection of the microbellow was measured with ±1 μm resolution. Figure 5-13 shows the center deflections of microbellows with diameters of 400 μm, 600 μm, and 800 μm under various pressure loads. With about 20 psi pressure input, they deflect about 20 μm, 41 μm, and 53 μm respectively.

In order to compare the deflections of the membrane with the deflections of the three-layer microbellow, plotted in Figure 5-13 are *three times* the deflection of the circular flat membranes with the same dimensions calculated by the following equation [6]:

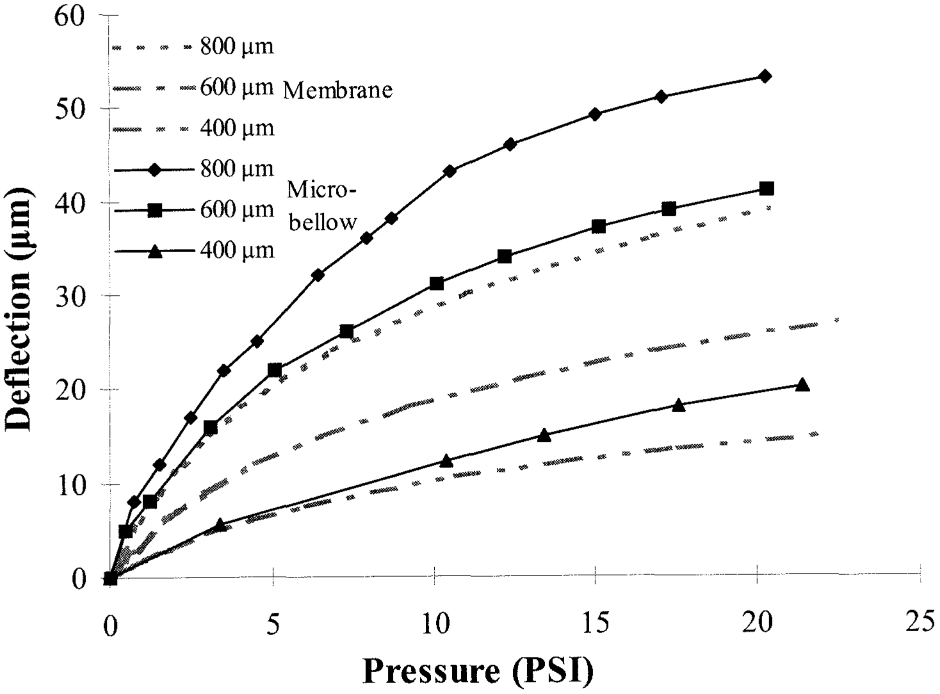

Figure 5-13 Deflections of Microbellows and Membranes

Note: Measured deflections of three-layer microbellows are plotted in solid lines. Three times of the theoretical deflections of single-layer flat membranes are plotted in dotted lines for comparison.

$$P = \frac{C_1 t\sigma}{a^2} d + \frac{C_2 f(\nu) t}{a^4} \frac{E}{1-\nu} d^3 \qquad (5\text{-}5)$$

where

P: applied pressure,

d: center deflection,

E: Young's modulus of silicon nitride, assume 300 GPa,

σ: residual stress in silicon nitride layer, assume 100 MPa,

ν: Poisson's ratio of silicon nitride, assume 0.25,

a: radius of the membrane,

t: thickness of the membrane.

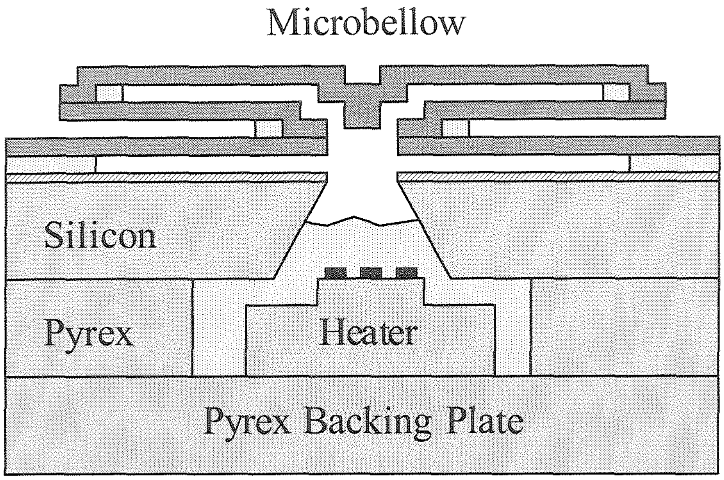

Figure 5-14 Cross-Sectional View of a Thermopneumatic Microbellow Actuator

For circular membranes,
$C_1 = 4.0$,
$C_2 = 2.67$,
$f(\nu) = (1.026 + 0.233\nu)^{-1}$.

It is clear that three-layer microbellows can deliver more than three times the deflection of simple flat membranes with the same constructions. This can be explained by the fact that, compared to the flat membranes, the residual stress in the three layers of microbellow is partially released and also the second and the third layer of the microbellow do not have the rigid boundary conditions. The load-deflection testing confirms that microbellows can achieve large deflections and small dimensions at the same time.

5.3.3 Thermopneumatic Actuation of Microbellows

Microbellows were also used to build thermopneumatic actuators. Thermopneumatic actuation was chosen to operate the microbellows because it can generate large forces with large deflections [7]. As shown in Figure 5-14, the thermopneumatic actuator

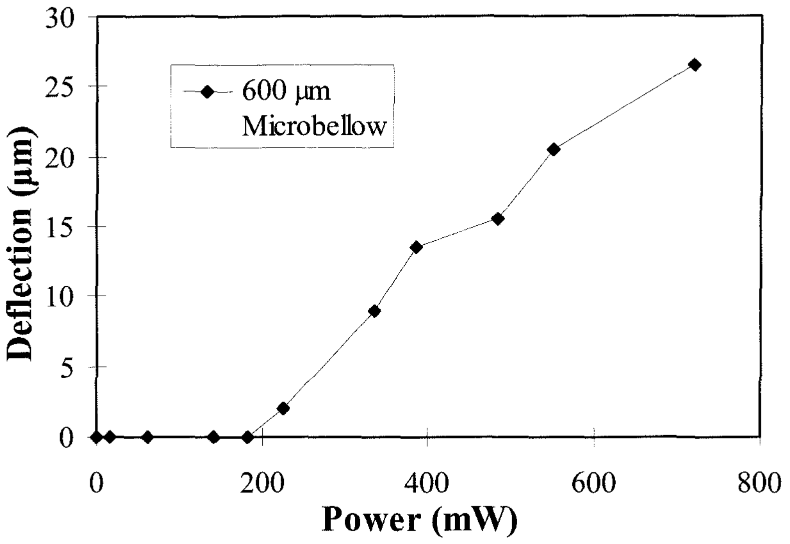

Figure 5-15 Thermopneumatic Actuation of Microbellows

consists of a resistive heater in a liquid chamber and a microbellow. The resistive heater was fabricated by evaporating and patterning a layer of 50 Å Cr/5000 Å Au on Pyrex glass to form a 2 Ω resistor. Two holes for liquid filling are drilled into the glass substrate. Then, the heater chip is glued to the back window of the microbellow actuator with epoxy. After the epoxy cures, the cavity is filled with water and sealed with a Pyrex backing plate. Actuation was tested by applying power to the heater and measuring the deflection of the microbellow actuator from its rest position using the calibrated microscope focusing method. The thermopneumatic actuation testing result of a 600 μm microbellow is shown in Figure 5-15. The microbellow actuator deflects 27 μm with 720 mW power input. Such high power consumption is required due to the extremely low thermal efficiency of the glass substrate heater. Computer simulation shows that 98% of the heat generated by the heater is lost through the glass substrate and the surrounding silicon [8]. This problem and the ways to solve them will be discussed more in detail in Chapter 7. Even though power consumption is high, the functionality of the microbellow actuator is, nevertheless, demonstrated.

5.4 Conclusion

Two generations of microbellow actuators have been successfully developed using surface micromachining technology. With polysilicon as sacrificial layer, the structure of the microbellows has been optimized to achieve large deflection and high strength. Experimentally, it has been shown that the microbellow can deliver more than three times the deflection of a flat membrane of the same size. Also, thermopneumatic actuators using the microbellows have been demonstrated. The microbellow actuators are very promising and suitable for microvalve and micropump applications.

Bibliography

[1] P. W. Barth, “Silicon Microvalve for Gas Flow Control,” Technical Digest, International Conference on Solid-State Sensors and Actuators (Transducers'95), Vol. 2, pp. 276-279, Stockholm, Sweden, June 1995.

[2] C. J. Van Mullem, K. J. Gabriel, and H. Fujita, “Large Deflection Performance of Surface Micromachined Corrugated Diaphragms,” Technical Digest, International Conference on Solid-State Sensors and Actuators (Transducers'91), pp. 1014-1017, San Francisco, USA, June 1991.

[3] Y. C. Tai, *IC-Processed Polysilicon Micromechanics: Technology, Materials and Devices*, Ph.D. Thesis, University of California, Berkeley, 1989.

[4] Y. C. Tai, and R. S. Muller, “Fracture Strain of LPCVD Polysilicon,” Technical Digest, IEEE Solid-State Sensor and Actuator Workshop (Hilton Head’88), pp. 88-91, Hilton Head Island, South Carolina, USA, June 1988.

[5] M. Sekimoto, H. Yoshihara, and T. Ohkubo, “Silicon Nitride Single-Layer X-Ray Mask,” Journal of Vacuum Science and Technology, Vol. 21(4), pp. 1017-1021, November/December 1982.

[6] J. Pan, P. Lin, F. Maseeh, and S. Senturia, “Verification of FEM Analysis of Load-Deflection Methods for Measuring Mechanical Properties of Thin Films,” Technical Digest, IEEE Solid State Sensor and Actuator Workshop (Hilton Head’90), pp. 70-73, Hilton Head Island, South Carolina, USA, June 1990.

[7] M. J. Zdeblick, *A Planar Process for an Electric-to-Fluidic Valve*, Ph.D. Dissertation, Stanford University, 1988.

[8] P. L. Bergstrom, J. Ji, Y.-N. Liu, M. Kaviany, and K. D. Wise, “Thermally Driven Phase-Change Microactuation,” Journal of Microelectromechanical Systems, Vol. 4-1, pp. 10-17, 1995.

[9] X. Yang, Y. C. Tai, and C. M. Ho, “Micro Bellow Actuator,” Technical Digest, International Conference on Solid-State Sensors and Actuators (Transducers '97), Vol. 1, pp. 45-48, Chicago, USA, June 1997.

Chapter 6

Silicone Rubber Membrane Valve

6.1 Introduction

As mentioned in Chapter 3, large actuation deflection is the key to a high performance MEMS valve. To achieve large deflection, a new actuator structure, the microbellows, has been demonstrated in Chapter 5. Another approach is to use low modulus materials in the mechanical structures.

One possible material is silicone rubber [1,2]. Silicones are organosilicon polymers in which the silicon atoms are bound to each other through oxygen atoms, the silicon valences not taken up by oxygen being saturated by at least one organic group. The prototype for the simple linear polymers is built up according to the following scheme:

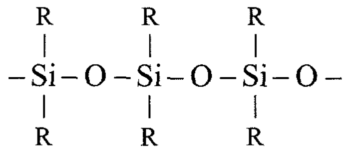

$$-\overset{\displaystyle R}{\underset{\displaystyle R}{Si}}-O-\overset{\displaystyle R}{\underset{\displaystyle R}{Si}}-O-\overset{\displaystyle R}{\underset{\displaystyle R}{Si}}-O- \qquad (R_2SiO)_n \qquad (6\text{-}1)$$

where R is an organic radical. Generally speaking, silicones are characterized according to the following structure principles:

a. Silicones are polymeric. They thus possess the typical structural features of organic macromolecules.

b. They contain silicon-oxygen bonds, and are thus fundamentally identical with the units forming the structure of silicic acids and silicates.

c. They contain hydrocarbon radicals combined directly with silicon and, therefore, structural units and bonds relate them to organic and, particularly, organometallic and organosilicon chemistry.

Silicones, therefore, occupy an intermediate position between organic and inorganic compounds, and in particular between silicates and organic polymers.

It is generally accepted that silicon rubber denotes high-molecular-weight linear polydiorganosiloxanes that can be converted from the highly viscous plastic state into the predominantly elastic state by cross-linking. This cross-linking step, also called “vulcanization” or “curing,” is very important to silicone rubber and can be achieved in various ways, such as cross-linking with organic peroxides at elevated temperatures, or cross-linking with organometallic and organic silicon compounds at room temperature or at only slightly elevated temperatures. Although there are many kinds of silicone rubber available, the basic skeleton is the same, a polydimethylsiloxane (PDMS) chain. Depending on their chemical and physical structures, with special substituents, it is possible to produce silicone rubbers which have similar basic properties but differ from one another in certain special characteristics. Generally speaking, the heat-vulcanizable types are characterized by extremely high molecular weights, while room-temperature-vulcanizable (RTV) types, since they must generally be suitable for dipping and spreading processes, are adjusted to a lower molecular weight and to a low viscosity.

The excellent mechanical properties of silicone rubber, such as a very low modulus, high elongation, and good sealing on rough surfaces, etc., make it very attractive for valve applications. In this chapter, silicone rubber MRTV 1 from American Safety Technologies, Inc., [3] is explored as a valve membrane material. The processing of this material and the valves developed using this material are described in detail in the following sections.

6.2 Silicone Rubber MRTV 1

MRTV 1 is an addition cure mold making RTV silicone rubber. It was chosen as the valve membrane material for two reasons. First, it can sustain elongation as high as

Table 6-1 Physical Properties of MRTV 1

Mixed Viscosity, cps	60,000
Hardness, Durometer	Shore A 24
Tensile Strength, psi	500
Tear Strength, Die B lb/in	125
Tensile Elongation, %	1,000
Temperature Range, °C	-55 to 200
Thermal Conductivity, W/cm-°C	0.002
Dielectric Strength, Volts/mil	550
Volume Resistivity, ohm-cm	1.6×10^{15}

1,000%, which means very large deflection can be achieved in valve membranes. Second, sealing of this material on rough surfaces can be very good due to its very low durometer (Shore A 24). This could be advantageous for valves. In valves made of conventional membrane material, the unavoidable particles in the flow could get stuck around the valve seat area and cause a non-trivial leak when the valve is supposed to be closed. With MRTV 1, it is possible that the material can completely encapsulate the particles and seal the valve seat. Other physical properties of this rubber are listed in Table 6-1.

The manufacturer suggests the following preparation procedure for MRTV 1.

a. Premix MRTV 1 base and curing agent before use to make sure all the filler is reincorporated.
b. Weigh out amount of base component required, then weigh into the base one part of catalyst for each 10 parts of MRTV 1 base.
c. Mix thoroughly.

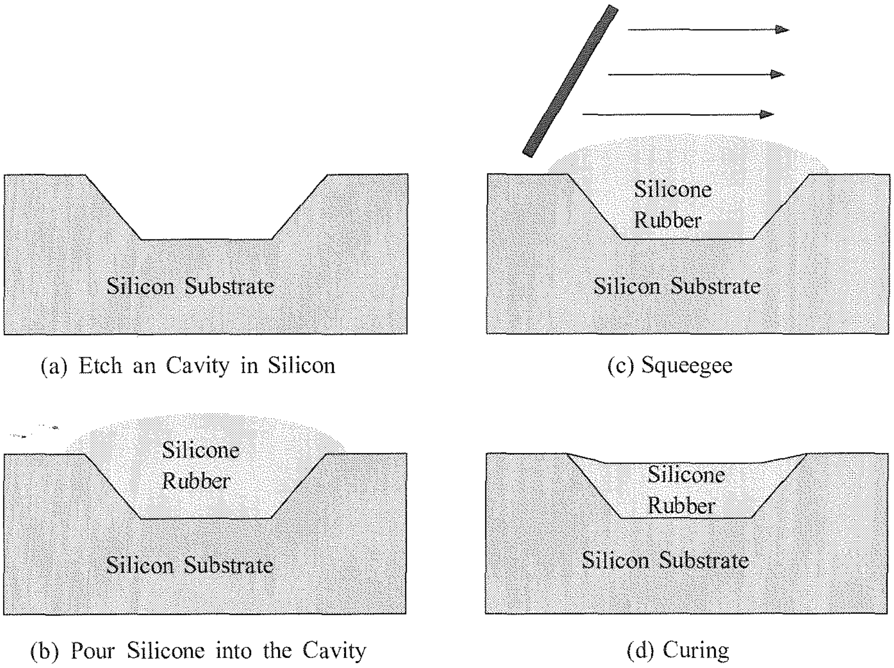

(a) Etch an Cavity in Silicon

(c) Squeegee

(b) Pour Silicone into the Cavity

(d) Curing

Figure 6-1 Squeegee Coating of Silicone Rubber

d. Place in a vacuum chamber to draw about 29 inches of mercury. The mixture will rise to about 3-4 times its original volume, then collapse. Hold the vacuum for another minute or two and release.

To coat the wafers with silicone rubber, it is most convenient to do spin coating as most silicone rubbers are too viscous to spray. However, MRTV1 is sufficiently viscous at 60,000 cps that uniform spin-coating can only be achieved at a very narrow range of spin rates. Experimentally, we find spin coating at the rate of 1000 rpm for 80 seconds gives 132±1 μm thick uniform layers of MRTV1 on silicon wafers. Slower speeds result in uneven films while higher speeds streak, bubble, and redistribute fillers non-uniformly. Other silicones such as GE RTV615 spin coat very well, but lack the properties of MRTV 1.

Another way to apply silicone rubber film on a silicon wafer is squeegee coating, which is shown in Figure 6-1. First, cavities with a certain depth are etched into the silicon substrate. Premixed MRTV1 is then poured onto the cavities. By scraping a piece of glass that has a flat smooth edge across the wafer, extra silicone rubber is taken away

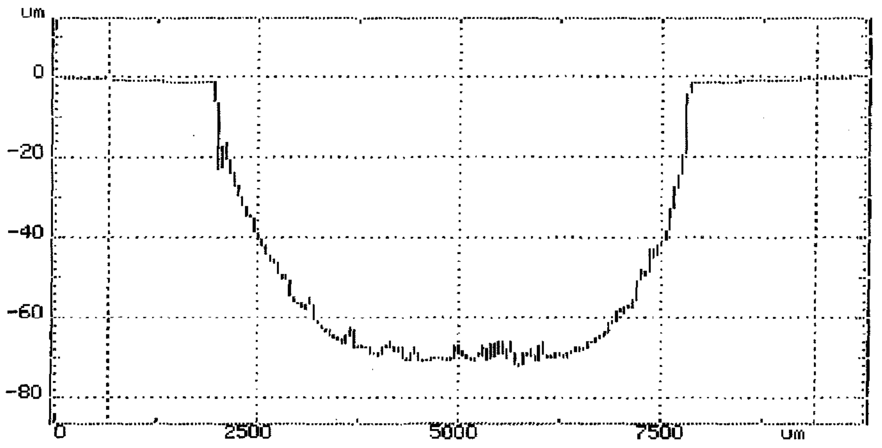

Figure 6-2 Surface Profile of a Cured Silicone Rubber Membrane

and a layer of silicone rubber film is left in the cavity. The squeegee coating technique works very well and produces uniform films from die to die. Compared to spin coating, squeegee coating can produce uniform films with various thicknesses by changing the depth of the cavity in the substrate. Also, by using this technique, only part of the wafer will be coated with silicone rubber film while the rest of the wafer is exposed. This has the advantage that other fabrication processes such as bonding can still be achieved on the areas without silicone rubber film. One thing that we notice is there is a recess at the center of the film, due to surface tension at the corners of the cavity, gravity force, and the shrinkage of the film after curing. Figure 6-2 shows the profile of the silicone rubber layer along the 5.8 mm dimension of the cavity. In this case, the recess is 70 μm. As we show later, this recess serves perfectly as the gap between the valve seat and membrane, which simplifies valve seat fabrication.

Various processing experiments have been done on MRTV 1. It was found that MRTV 1 exhibits excellent adhesion to silicon, silicon oxide, silicon nitride, and metals due to the presence of silane groups in the formulation. Cured films tend to tear before peeling. MRTV1 is resistant to buffered hydrofluoric acid, positive photoresist developer, isopropyl alcohol, and oxygen plasma for short periods of time (< 30 minutes). Long term exposure to strong acids, organic solvents such as acetone, xylene, benzene, and strong alkalis will destroy the films. The etch rate in CF_4 plasma is similar to silicon

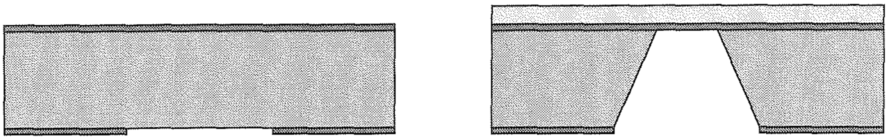

(a) Silicon Nitride Deposition and Patterning

(c) Silicone Rubber Spin Coating

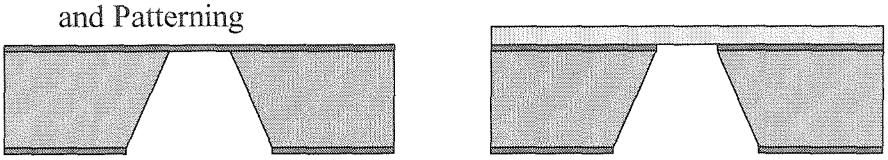

(b) Silicon Etching in KOH

(d) Silicon Nitride Removal

Figure 6-3 Fabrication Process for Spin Coated Silicone Rubber Membrane

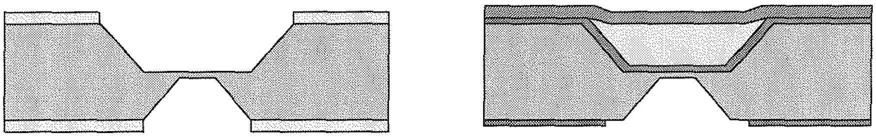

(a) KOH Etching

(d) Back Side Patterning

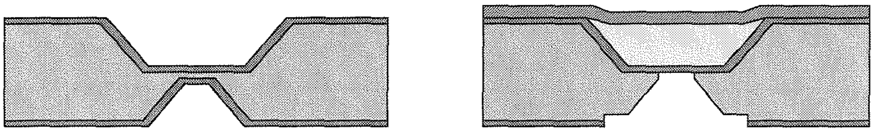

(b) Silicon Nitride Deposition

(e) BrF_3 Releasing

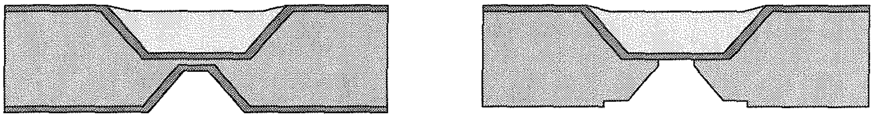

(c) Silicone Rubber Squeegee Coating

(f) Silicon Nitride Removal

Figure 6-4 Fabrication Process for Squeegee Coated Silicone Rubber Membrane

dioxide which is to be expected. Adhesion to photoresist and most glues is very poor. Thin silicone rubber films are permeable to chemical vapors and absorb some liquids.

6.3 Silicone Rubber Membrane Fabrication

To determine the mechanical properties of the silicone rubber, a simple membrane chip was fabricated as shown in Figure 6-3. The chip was fabricated on a 500 μm thick <100>

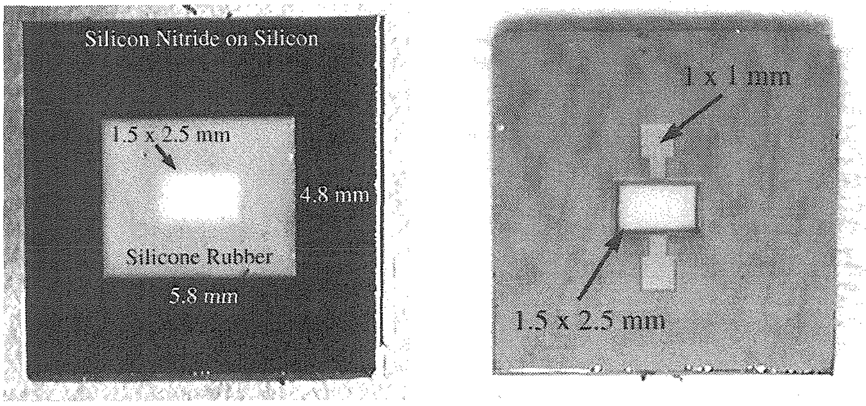

(a) Top of the Membrane (b) Bottom of the Membrane

Figure 6-5 Pictures of a Fabricated Silicone Rubber Membrane

wafer. First, a layer of 1 μm thick low-stress LPCVD silicon nitride was deposited. The back side was patterned with 3 mm × 3 mm windows using SF_6/O_2 plasma. KOH was then used to etch the silicon to the front side nitride forming 2.3 mm × 2.3 mm membranes. MRTV1 silicone was spin coated on the front side forming a 132 μm silicone rubber layer. The silicone rubber was then cured at room temperature for 24 hours. Finally, the nitride membranes were removed using SF_6/O_2 plasma from back side leaving free silicone rubber membranes.

By using squeegee coating, second generation silicone rubber membrane was developed as shown in Figure 6-4. A <100> wafer was oxidized and patterned on both sides and etched in KOH to form two cavities. The top cavity was 4.8 mm × 5.8 mm and served as a mold for the silicone rubber. The bottom cavity served as the reservoir for the fluid and defined the dimensions of the silicone membrane which is 1.5 mm × 2.5 mm. The 520 μm thick wafer was etched 235 μm in KOH on each side leaving a 50 μm thick silicon membrane. A layer of 0.5 μm thick low-stress silicon nitride was deposited on both sides and MRTV 1 silicone rubber was molded into the top cavity by squeegee coating. The back side nitride was patterned using SF_6/O_2 plasma to remove the nitride over the silicon membrane and define two openings that provided clearance when adding liquid to the assembled valve. The 50 μm silicon membrane and the openings were

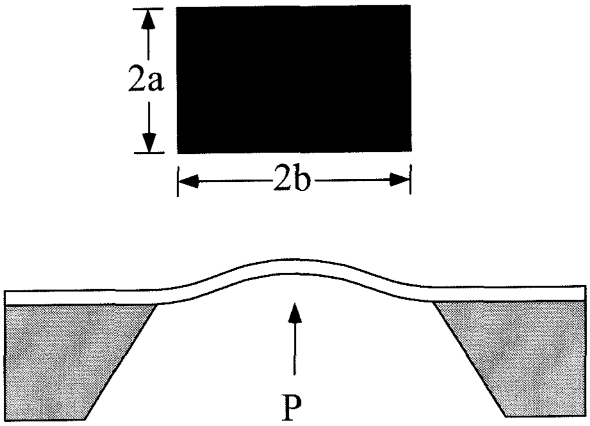

Figure 6-6 Load-Deflection Testing of Membranes

etched using BrF_3 vapor [4] while the remainder of the wafer was protected with photoresist and silicon nitride. Finally, the silicon nitride underneath the silicone rubber membrane was stripped from the back side.

Figure 6-5 shows the front side and back side of the membrane fabricated using squeegee coating.

6.4 Silicone Rubber Membrane Testing

Load-deflection tests were performed on the simple silicone rubber membranes to measure Young's modulus, E, and residual stress, σ. The silicone rubber membrane chip was mounted and sealed on a special holder and was then placed on the x-y stage of an optical microscope with z-direction focus adjustment calibrated in 1 μm increments. Pneumatic pressure was applied from the back side windows. By adjusting the input pressure and focus position, the center deflection of the membrane was measured with ±1 μm resolution. It was shown [5] that for a rectangular membrane shown in Figure 6-6, the load-deflection relationship of the rectangular membrane can be expressed as

$$P = \frac{C_1 \sigma t h}{a^2} + \frac{C_2 E t h^3}{a^4} \tag{6-2}$$

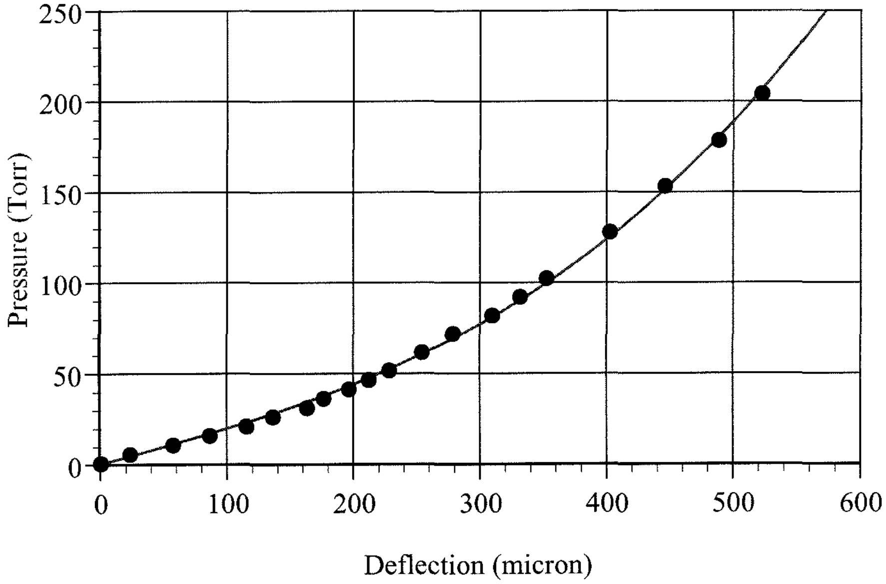

Figure 6-7 Load-Deflection Testing Results and Theoretical Fitting

where

$$C_1 = \frac{\pi^4 (1+n^2)}{64}$$

$$C_2 = \frac{\pi^6}{32(1-\nu^2)}\{\frac{9+2n^2+9n^4}{256} - \frac{[4+n+n^2+4n^3-3n\nu(1+n)]^2}{2[81\pi^2(1+n^2)+128n+\nu(128-9\pi^2(1+n^2))]}\}$$

P: applied pressure,

E: Young's modulus of the membrane material,

σ: residual stress in the membrane,

ν: Poisson's ratio of the membrane material,

t: thickness of the membrane,

h: deflection of the membrane,

n: a/b.

For square membranes, C_1 and C_2 are calculated to be 3.04 and 1.83 respectively assuming Poisson's ratio is 0.25. Since Young's modulus, E, and residual stress, σ,

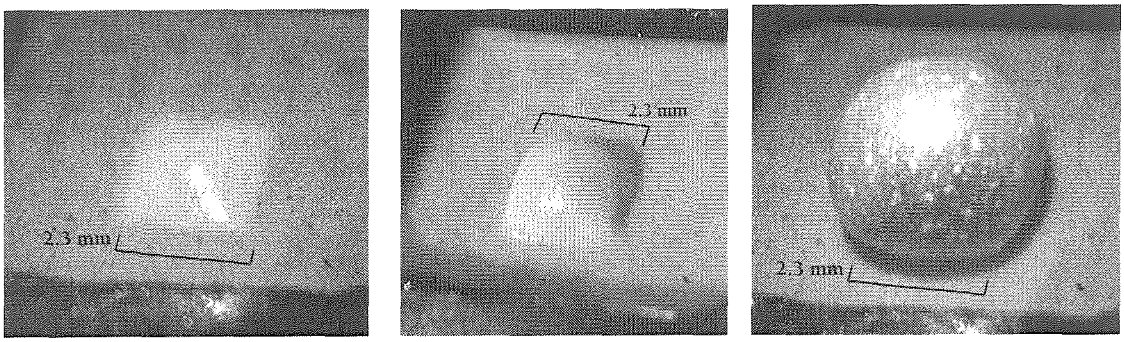

(a) 0 psi (b) 6.0 psi (c) 14.6 psi

Figure 6-8 Membrane Deflection

independently appear in the linear term and the cubic term of Equation (6-2), they can be determined by fitting the experimental data with Equation (6-2).

Figure 6-7 shows the measurement data and the fitting curve for a 2.3 mm × 2.3 mm × 132 μm membrane. The fitting results give the following corresponding formula for the curve.

$$P = 0.188h + 7.538 \times 10^{-7} h^3 \tag{6-3}$$

Assuming the Poisson's ratio of silicone rubber is 0.5, C_1 and C_2 in Equation (6-2) are calculated to be 3.04 and 2.55. From the coefficients of the Equation (6-3), the Young's modulus and residual stress of silicon rubber can easily be determined.

$$E = 0.51 \text{ MPa} \tag{6-4}$$

$$\sigma = 0.08 \text{ MPa} \tag{6-5}$$

Figure 6-8 shows the membrane at (a) 0 psi, (b) 6.0 psi, and (c) 14.6 psi. At 6.0 PSI, the membrane deflects 900 μm. At 14.6 PSI, the membrane deflects 1.54 mm which corresponds approximately to a 115% increase in volume and a 100% increase in surface area. Figure 6-9 shows the side view of the membrane at (a) 1 psi, (b) 5 psi, (c) 10 psi, and (d) 15 psi.

Shown in Figure 6-10 are the same results as in Figure 6-7 but are plotted in a larger pressure and deflection range. It can be seen that if pressure larger than 5.0 psi is

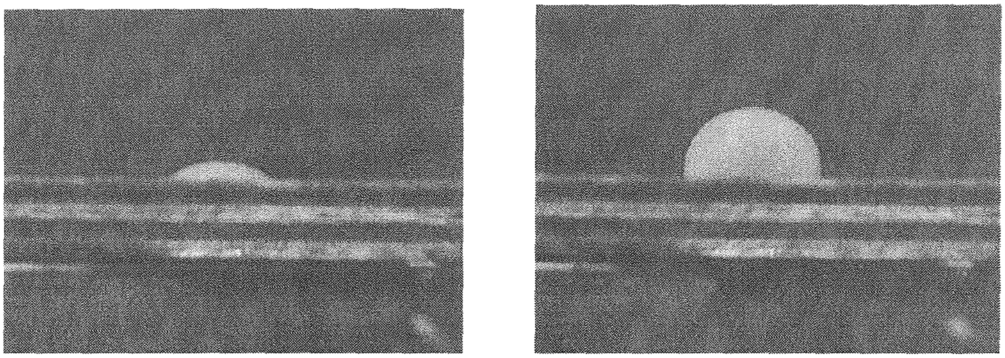

(a) 1psi (c) 10 psi

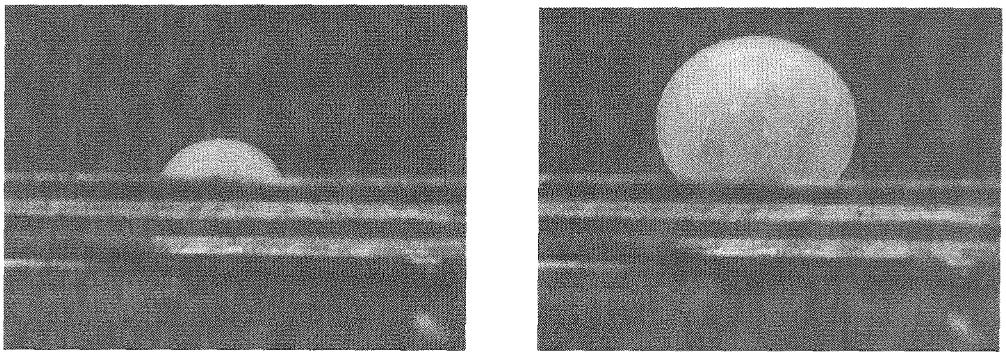

(b) 5 psi (d) 15 psi

Figure 6-9 Side View of Membrane Deflection

applied to the membrane, the deflection data starts to deviate from the theoretical model. Experimentally, we find that the membrane is plastically deformed in this pressure range. In other words, the membrane will not go back to the original flat position once the pressure is released. However, plastic deformation is not a concern to the valve because the design goal for the gap in the valve is less than 100 μm.

6.5 Thermopneumatic Actuation

A resistive heater was fabricated on a Pyrex glass substrate by evaporating and patterning a layer of 100 Å Cr/7000 Å Au. Two holes for liquid filling were mechanically drilled through the substrate. The fabricated glass heater is shown in Figure 6-11. A simple thermopneumatic actuator was assembled by gluing the heater to the back side of the

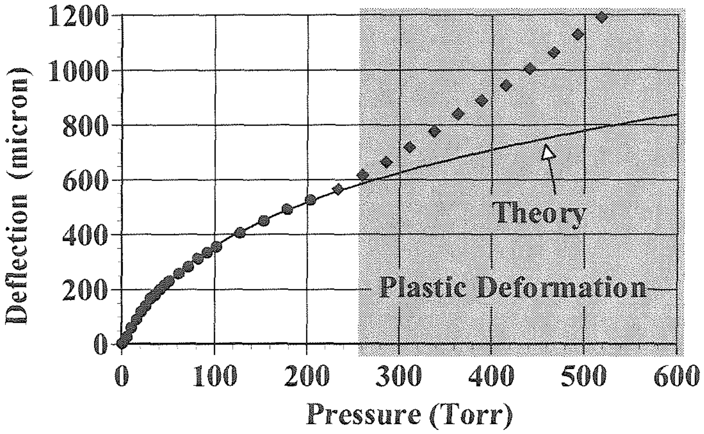

Figure 6-10 Membrane Plastic Deformation

membrane using epoxy as shown in Figure 6-12. A calibrated microscope was used to measure vertical displacement. Since the volume of the heater/membrane assembly changes significantly during operation, we chose a gas/liquid system for thermopneumatic actuation due to its greater efficiency [6]. The liquid chosen had to be compatible with silicone rubber and the resistive heater. Isopropyl alcohol and 3M Performance Fluids (industrial versions of Fluorinert^{TM}) were used, due to their greater vapor pressure *vs*. temperature as compared to water. The cavity formed by the simple membrane and heater dice was filled with a small amount of liquid (10 to 20%) and sealed. Actuation was observed by applying a fixed amount of power and measuring deflection of the membrane from its rest position. Figure 6-13 shows the results for (a) isopropyl alcohol and (b) 3M PF5060 as the working liquid. With isopropyl alcohol as the working liquid, the membrane deflected 620 μm at 0.87 W power input which corresponds to 5 psi. Using 3M PF5060, the membrane deflected 860 μm at 0.94 W power input which corresponds to 7 psi. These results confirm that silicone rubber membranes with a liquid/gas system can deliver large deflection with reasonable power.

One problem with this actuator is the relatively high power consumption due to its low thermal efficiency. Computer simulation shows that 98% of the heat generated by the heater is lost through the glass substrate and the surrounding silicon [7]. To remedy this problem, vacuum insulated heaters were developed. By fabricating the heaters on top of

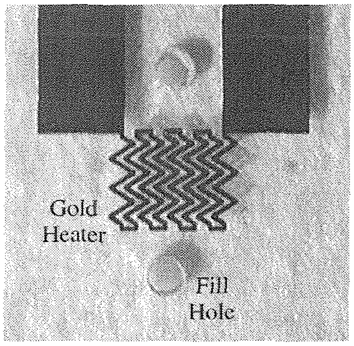

Figure 6-11 Fabricated Glass Heater

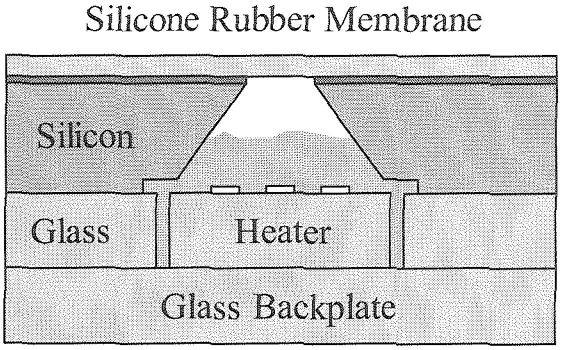

Figure 6-12 Thermopneumatic Actuator

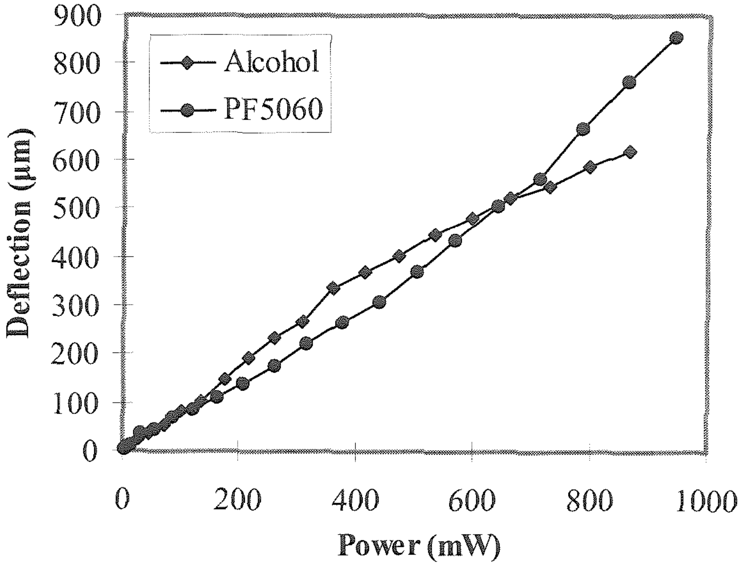

Figure 6-13 Thermopneumatic Actuation

an array of vacuum cavities, the heat loss should be significantly reduced because the vacuum and the vacuum cavity membrane material, which is silicon nitride here, have very low thermal conductivity.

The fabrication process for the vacuum insulated heaters is shown in Figure 6-14. First, a layer of 0.2 μm thick silicon nitride was deposited and patterned. A 0.55 μm deep recess was etched into the silicon substrate using SF_6/O_2 plasma. Then, a layer of 1 μm thick thermal oxide was grown only in the recess area because the rest of the area was covered with silicon nitride mask. After this, the silicon nitride mask was stripped.

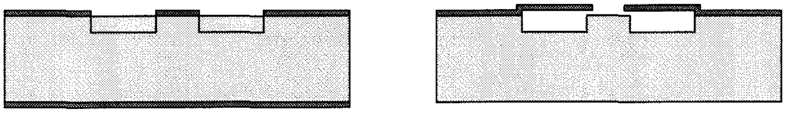

(a) Fully Recessed LOCOS

(d) HF Releasing

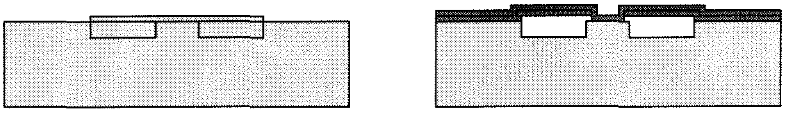

(b) PSG Deposition and Patterning

(e) Sealing with Silicon Nitride Deposition

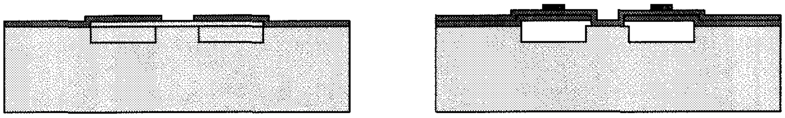

(c) Silicon Nitride Deposition and Patterning

(f) Cr/Au Deposition and Patterning

Figure 6-14 Fabrication Process for Vacuum Insulated Heater

Because of the initial recess in the silicon substrate, the final silicon oxide layer formed a planar surface with the silicon substrate. This is defined as fully recessed LOCOS (LOCal Oxidation of Silicon) process. Then, a layer of 0.3 μm thick LPCVD PSG layer was deposited at 450 °C and patterned, followed by a layer of 0.5 μm thick LPCVD low stress silicon nitride deposition. Etch holes were opened in the silicon nitride layer. The sacrificial thermal oxide/PSG layer was then etched away in high concentration HF to free the cavities. After this, the cavities were sealed with a layer of 0.5 μm thick silicon nitride. Because the deposition was done in low pressure (~300 mTorr), an array of vacuum cavities was formed. Finally, a layer of 100 Å Cr/7000 Å Au was evaporated and patterned to define the heaters. One problem encountered in this process is that a lot of cavities cracked during the HF releasing process as shown in Figure 6-15. It is suspected that the "bird's beak" in the LOCOS layer caused the cracking. The surface profile across the vacuum cavity area shows a 0.6 to 0.7 μm high "bird's beak," which became high stress concentration points when the cavities were free. Due to this problem, the yield of this process was very low. Figure 6-16 shows the vacuum cavity array that survived this process. The Newton rings in Figure 6-16 (a) are the indication of vacuum inside the cavity because the pressure difference across the membrane causes the bending of the

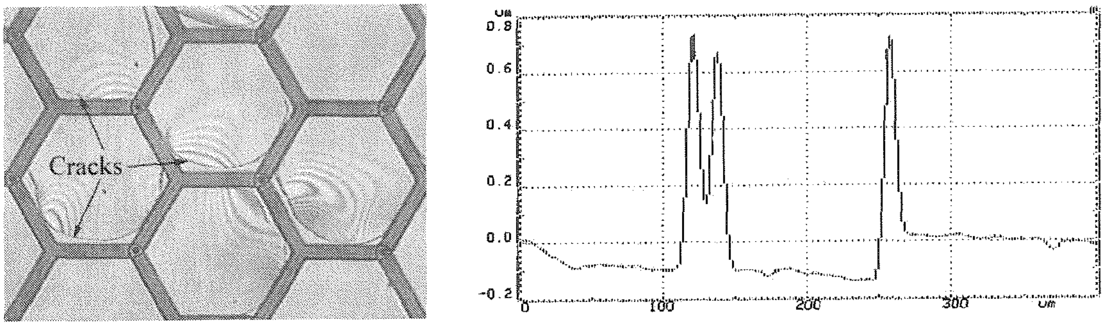

(a) Cracks around Bird's Beak

(b) Surface Profile of Bird's Beak

Figure 6-15 Cavity Membrane Cracking Due to Bird's Beak

cavity membrane. The fabricated heater is shown in Figure 6-16 (b). The heater has a large circular gold pad in the center of every vacuum cavity. Such a heater design will help achieve uniform heating on the surface.

Unfortunately, experiments show that this heater has similar thermopneumatic actuation performance as the glass heater. It is believed that the heat dissipates to the substrate through the anchor region of every vacuum cavity. In the future, this could be solved by stacking more layers of vacuum cavities to avoid a direct contact of the heater to the substrate. Also, a new process is needed to solve the problem of cracking and

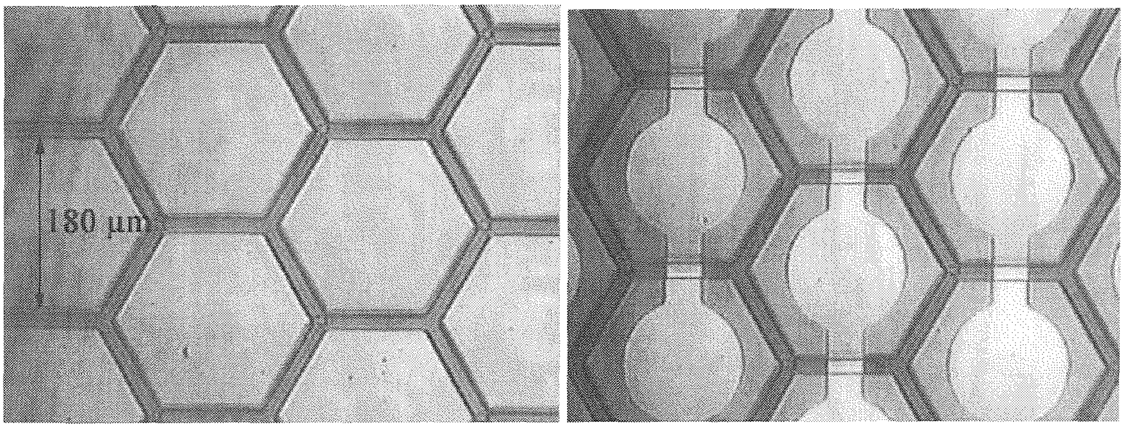

(a) Fabricated Vacuum Cavities

(b) Au Heater on Vacuum Cavities

Figure 6-16 Pictures of Fabricated Heaters on Vacuum Cavity Array

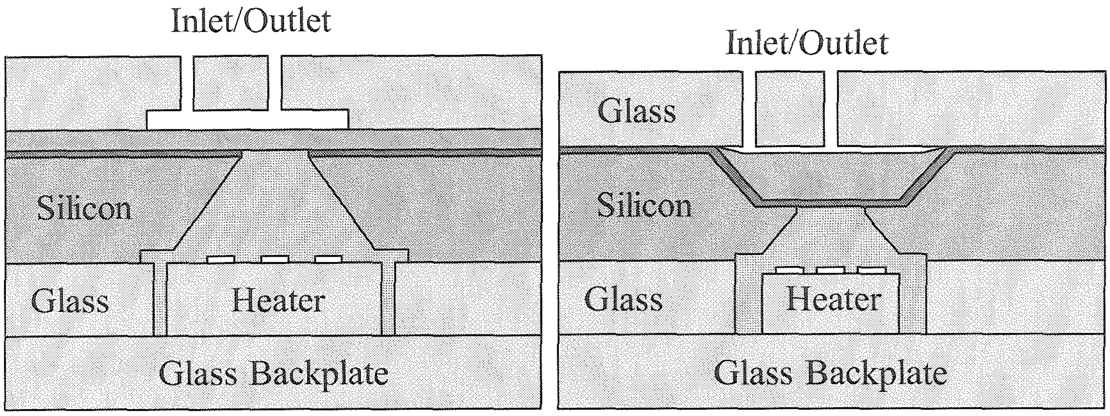

(a) First Generation Valve (b) Second Generation Valve

Figure 6-17 Cross-sectional View of Valves

increase the process yield.

6.6 Valve Performance

Two generations of the valve have been developed. As shown in Figure 6-17 (a), the first generation valve was assembled by gluing the heater chip (Figure 6-11), the simple silicone rubber membrane chip, and a valve seat chip together. The valve seat was fabricated on a Corning 2947 glass substrate with a 100 μm deep cavity etched on the front side and mechanically drilled inlet/outlet holes. The first generation valve had several disadvantages. First, gluing the valve seat to the membrane is difficult since the adhesion of most glues to silicone rubber is poor. Second, deep etching into the glass substrate makes the fabrication complicated. Third, the cavity underneath the silicone rubber membrane is too large.

The second generation valve (Figure 6-17 (b)) was developed by taking advantage of the recess of the cured silicone rubber membrane fabricated by using squeegee coating. The valve seat was simpler. It was fabricated on Corning 2947 glass substrate. Inlet and outlet holes were mechanically drilled and 500 μm i.d. fused silica capillaries were glued to the glass with epoxy. Since the gap between the valve inlet chip and the membrane

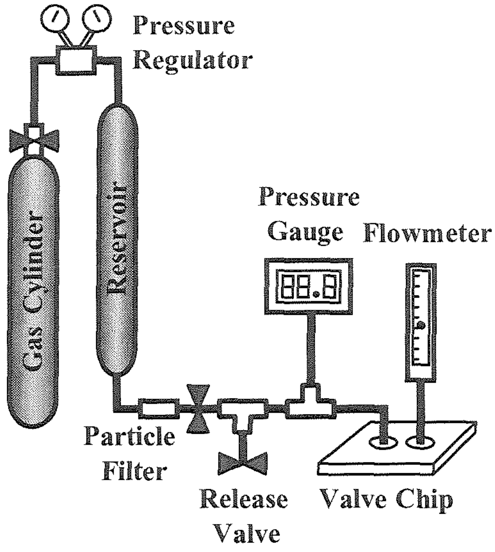

Figure 6-18 Valve Testing Setup

was defined by the curvature of the cured silicone rubber film and was 60 to 70 μm, there was no need for substrate etching. The valve was assembled by gluing the valve seat and heater chips to the membrane chip with epoxy. The recessed nature of the silicone rubber membrane allowed the use of standard glues as the valve seat only contacted the silicon surface. After the epoxy cured, the cavity was filled with an appropriate liquid and sealed with a back plate.

The valves were tested using the setup shown in Figure 6-18. A pressure sensor was used to measure inlet pressure and a flow meter was used to measure the output flow. A reservoir and pressure regulator provide a reasonably constant flow of compressed air to the valve inlet. The valve was tested at two different inlet pressures. One minute was given between successive data points to allow the valve to warm up or cool down. The valve tested used 3M PF5060 as the working fluid. Since the maximum deflection of the membrane is limited to 70 μm by the mechanical design, large displacements are not necessary. As the volume of the cavity/membrane system does not change significantly, the cavity is filled (80 to 90%) with liquid for better performance [6]. It should be noted that at room temperature, 3M PF5060 has a vapor pressure of 4 psi which results in the requirement that the inlet pressure be higher than 3 psi for proper valve operation as 1 psi

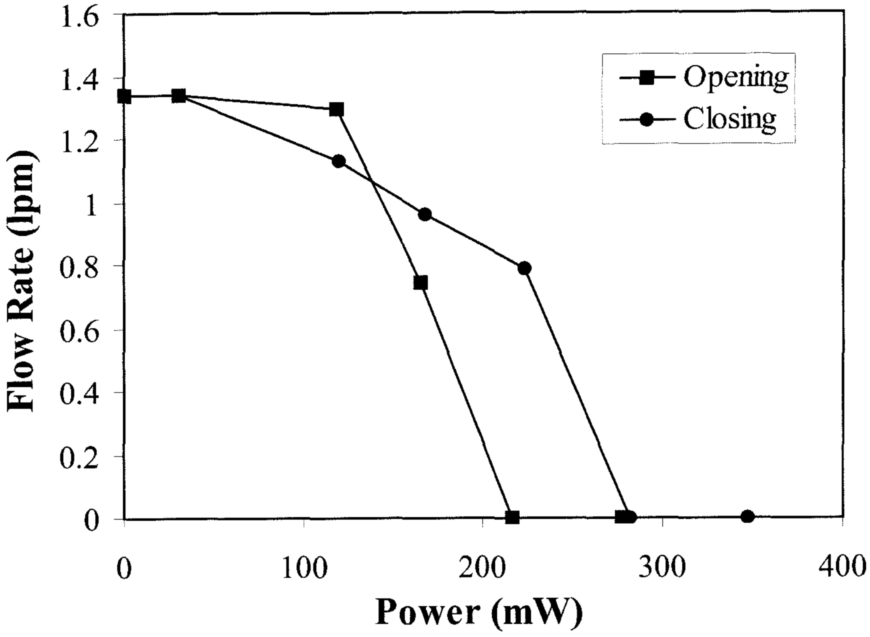

Figure 6-19 Valve Performance at Inlet Pressure of 20 psi

is required to deflect the membrane to the valve seat. Figure 6-19 shows valve operation at 20 psi inlet pressure. With a power input of 280 mW, the valve shuts off a flow of 1.34 lpm. Figure 6-20 shows the same valve operated at 30 psi. In this case, the valve shuts off the flow of 1.79 lpm with 650 mW power input. It can be seen from both figures that the valve shows a certain degree of hysteresis, which is what we expect. The most likely cause of this is the need to heat up the substrate when closing the valve. Once up to temperature, it takes less power to keep the membrane deflected and the heat storage of the substrate keeps the valve closed longer. Further work is necessary to investigate alternative substrates with lower thermal conductivity to improve performance.

Experimentally, it was observed that most of the liquids used for thermopneumatic actuation escaped from a sealed valve or actuator as vapor in a matter of days. While this is endemic of silicone in general, it is further exacerbated by the use of thin layers. The solution is the use of a composite membrane with a sealing film between the liquid and silicone rubber.

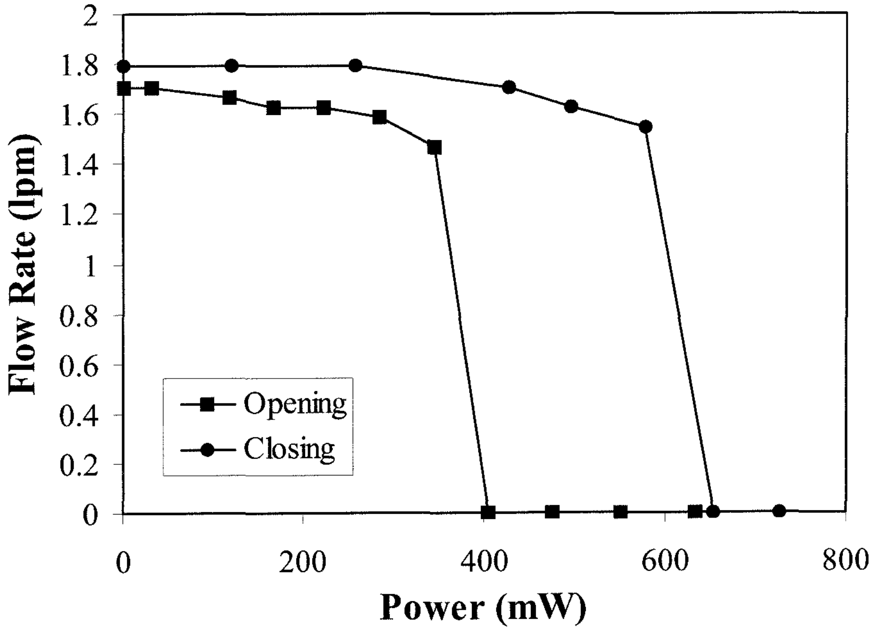

Figure 6-20 Valve Performance at Inlet Pressure of 30 psi

6.7 Conclusion

Several methods for fabricating silicone rubber membranes and integrating them with micromachined components to make actuators and valves have been developed. The silicone rubber has been characterized and has been found to have many desirable properties including high elongation, good sealing, low modulus of elasticity, and compatibility with IC processes. A thermopneumatically actuated valve has been successfully demonstrated. It was shown that 280 mW will close a 1.34 lpm air flow at 20 psi. Although this technology is promising, several problems such as high power consumption, working liquid leakage, etc., remain unsolved and require more work.

Bibliography

[1] C. Vieider, O. Ohman, and H. Elderstig, “A Pneumatically Actuated Microvalve with a Silicone Rubber Membrane for Integration with Fluid Handling Systems,” Technical Digest, International Conference on Solid-State Sensors and Actuators (Transducers’95), Vol. 2, pp. 284-286, Stockholm, Sweden, June 1995.

[2] L. Bousse, E. Dijkstra, and O. Guenat, “High-density Arrays of Valves and Interconnects for Liquid Switching,” Technical Digest, Solid State Sensor and Actuator Workshop (Hilton Head ’96), pp. 272-275, Hilton Head Island, South Carolina, USA, June 1996.

[3] American Safety Technologies, Inc., 565 Eagle Rock Avenue, Roseland, NJ 070668.

[4] X. Q. Wang, X. Yang, K. Walsh, and Y. C. Tai, “Gas Phase Silicon Etching with Bromine Trifluoride,” Technical Digest, International Conference on Solid-State Sensors and Actuators (Transducers’97), Vol. 2, pp. 1505-1508, Chicago, June 1997.

[5] O. Tabata, K. Kawahata, S. Sugiyama, and I. Igarashi, “Mechanical Property Measurements of Thin Films Using Load Deflection of Composite Rectangular Membranes,” Sensors and Actuators A, 20, pp. 135-141, 1989.

[6] M. Zdeblick, R. Anderson, J. Janskowski, B. Kline-Schoder, L. Christel, R. Miles, and W. Weber, “Thermopneumatically Actuated Microvalves and Integrated Electro-fluidic Circuits,” Technical Digest, Solid State Sensor and Actuator Workshop (Hilton Head ’94), pp. 251-255, Hilton Head Island, South Carolina, USA, June 1994.

[7] P. L. Bergstrom, J. Ji, Y.-N. Liu, M. Kaviany, and K. D. Wise, “Thermally Driven Phase-Change Microactuation,” Journal of Microelectromechanical Systems, Vol. 4-1, pp. 10-17, 1995.

[8] X. Yang, C. Grosjean, Y. C. Tai, and C. M. Ho, “A MEMS Thermopneumatic Silicone Membrane Valve,” Proceedings of IEEE Workshop on Micro Electro Mechanical Systems (MEMS’97), pp. 114-118, Nagoya, Japan, January 1997.

[9] X. Yang, C. Grosjean, Y. C. Tai, and C. M. Ho, “A MEMS Thermopneumatic Silicone Rubber Membrane Valve,” Sensors and Actuators A, 64, pp. 101-108, 1998.

Chapter 7

Silicone Rubber/Parylene Membrane Valve

7.1 Introduction

In Chapter 6, a thermopneumatic valve [1,2] with silicone rubber as membrane material has been developed. The valve consists of a cavity filled with a working fluid and sealed with a glass substrate heater on one side and a silicone membrane on the other. It was demonstrated that silicone rubber has a low Young's modulus (0.51 MPa) and high elongation (~1,000%). Also, technologies have been developed to fabricate silicone rubber membranes on silicon substrates. Using thermopneumatic actuation, larger deflections are obtained compared to devices using silicon membranes. Although good valve performance was achieved, there were several problems that remained unsolved. First, it was found that the working fluid would leak through the permeable silicone membrane in a matter of days rendering the valves unusable. Second, the power consumption of the valve was high, and in part due to the design of the heater as a gold resistor on a glass substrate. A large portion of the input power would go into heating the substrate rather than the working fluid, and computer simulation shows that 98% of the heat generated by a heater can be lost through the glass substrate [3]. Third, the valve seat was fabricated on a glass substrate using conventional mechanical drilling. This was a tedious process and created a lot of debris around the inlet and outlet areas. Efforts have been made to solve these problems and here are the corresponding solutions. To prevent the working liquid from leaking through the silicone rubber membrane, a vapor barrier layer is sandwiched between the flexible silicon rubber layer and the working liquid. Most IC compatible materials that are impermeable to the chosen working liquids have very high modulus which defeats the purpose of a silicone membrane valve. It was found that Parylene, which has a fairly low modulus C, is an effective barrier. To reduce the valve power consumption, a gold resistive heater on a thin silicon nitride membrane is suspended in the working liquid. Because of the small cross section of the membrane and the inherent low thermal conductivity of SiN, the heat lost to the substrate and the environment is minimized. Finally, a corrugated valve seat optimized for the compliant silicone membrane has been bulk-micromachined on a silicon substrate. The outlet hole is surrounded by concentric grooves to create redundant seals and reduce the chance of a leak due to particles. In the following sections, the composite silicone rubber/Parylene membrane, free-standing silicon nitride membrane heater, and novel valve seat will be described in detail. Also, the steady state and transient performance of thermopneumatic actuation and the valve performance will be presented.

7.2 Silicone Rubber/Parylene Composite Membrane

Although in Chapter 6 it was demonstrated that silicone rubber has many advantages, the slow leakage of the working liquid for the thermopneumatic actuation through the silicone rubber membrane destroys the valve in a few days. The proposed solution to this problem is to use a vapor barrier layer between the working liquid and the silicone rubber. Not only does this layer have to be impermeable to the working liquids, but it also has to be flexible. Before processing technologies are developed to integrate it with the

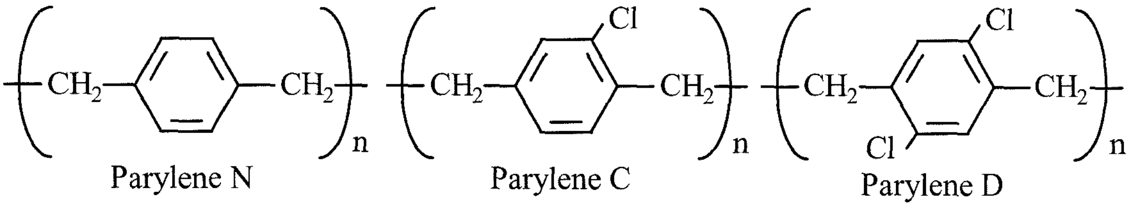

Parylene N Parylene C Parylene D

Figure 7-1 Chemical Structures of Parylene N, C, and D silicone rubber layer, mechanical properties of the vapor barrier layer have to be studied to ensure it has a low Young's modulus.

7.2.1 Parylene

Parylene [3] is the generic name for members of a unique family of thermoplastic polymers. Three forms of this polymer as shown in Figure 7-1 are currently available, each with unique properties that suit it to particular applications. The basic member of the series, Parylene N, is poly-para-xylylene, a completely linear, highly crystalline material. It exhibits a very low dissipation factor, high dielectric strength, a dielectric constant invariant with frequency and it is widely used as a dielectric material. Parylene C, the second member of the series, is produced from the same monomer modified only by the substitution of a chlorine atom for one of the aromatic hydrogens. Parylene C has a useful combination of electrical and physical properties. The important one to valve applications is its very low permeability to moisture and gases. Parylene C is a popular

Table 7-1 Properties of Parylene

Properties	Parylene N	Parylene C	Parylene D
Tensile Strength (psi)	6,000-11,000	10,000	11,000
Elongation to Break (%)	20-250	200	10
Water Absorption (% after 24 hours)	Less than 0.1	Less than 0.1	Less than 0.1
Melting Point (°C)	420	290	380
Thermal Conductivity at 25 °C (W/m °C)	0.126	0.084	unavailable
Moisture Transmission at 90% RH, 37 °C (g-mil/100 $in^2 \cdot d$)	1.5	0.21	0.25

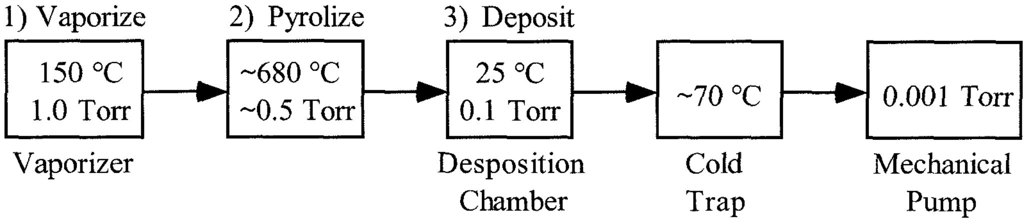

Figure 7-2 Parylene Deposition Process

material of choice for coating critical electrical assemblies. Parylene D, the third member of the series, is produced from the same monomer modified by the substitution of the chlorine atom for two of the aromatic hydrogens. Parylene D is similar in properties to Parylene C with improved thermal stability and superior physical and electrical properties at high temperature. The common physical properties [3] of Parylene N, C, and D are listed in Table 7-1.

The Parylene deposition process was developed by William F. Gorham in the early 1950s. Based on an earlier discovery of the polymer, Dr. Gorham patented a particularly advantageous vapor deposition method that used the dimer of para-xylylene (di-para-xylylene, or DPX) as a starting material to produce the polymer Parylene (poly-para-xylylene or DPXN). Parylene vapor deposition is performed at roughly 0.1 Torr and room temperature. Under these conditions the mean free path of the gas molecules in the deposition chambers is in the order of 0.1 cm. Therefore, the deposition is not of line of sight, and all sides of an object to be deposited are uniformly impinged by the gaseous monomer. Because of this, the deposition is truly conformal. The deposition process consists of three steps as shown in Figure 7-2 for Parylene N. It starts with vaporization of the solid dimer at approximately 150 °C. Then, the quantitative cleavage (pyrolysis) of the dimer at the two methy-lene-methylene bonds at about 680 °C yields the stable monomeric diradical, para-xylylene. Finally, the monomer enters the room temperature deposition chamber where it simultaneously adsorbs and polymerizes on the substrate. The substrate temperature never rises more than a few degrees above ambient during the whole deposition process. A necessary fourth component in this system is the mechanical vacuum pump and associated protective traps. For Parylene C, it is typically deposited at

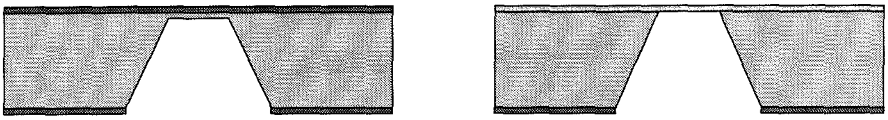

(a) Thermal Oxidation, Patterning, and KOH Etching

(c) BrF_3 Vapor Etching

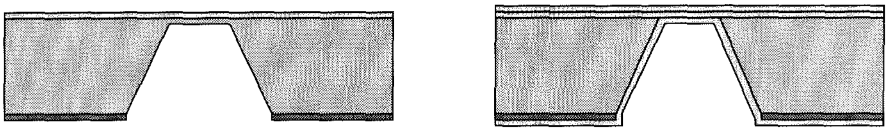

(b) 1st Parylene C Deposition

(d) 2nd Parylene C Deposition

Figure 7-3 Parylene Membrane Fabrication Process

about 0.2 μm per minute. Parylene deposition materials, systems, and services are available from Specialty Coating Systems, Inc. (SCS). All the depositions in this thesis were performed on a portable Parylene deposition system model PDS 2010 LABCOTER® 1 from SCS.

During the last decade, Parylene has been explored as passivation material or dielectric material between multilevel metallization for the IC industry. Because of its superb electrical and mechanical properties, Parylene will find many applications in MEMS.

7.2.2 Mechanical Properties of Parylene C

To measure the mechanical properties of Parylene C, square Parylene membranes have been fabricated using the process shown in Figure 7-3. First, a layer of 2 μm thick silicon oxide was thermally grown on the wafers at 1050 °C and patterned to open the windows at the wafer back side. Then, the wafers were etched from back side in a 10 % KOH solution at 58 °C until only 20 μm thick silicon layer was left. The thermal oxide at the front side was stripped and a layer of 2 μm thick Parylene C was deposited on the wafers. A–174 adhesion promoter for the Parylene was applied to the wafers before the Parylene deposition. After that, the Parylene layer was etched way using oxygen plasma at 400 mTorr pressure and 400 W power while the wafer front side was protected with photoresist. The 20 μm thick silicon layer was then etched way in a BrF_3 vapor [4] from

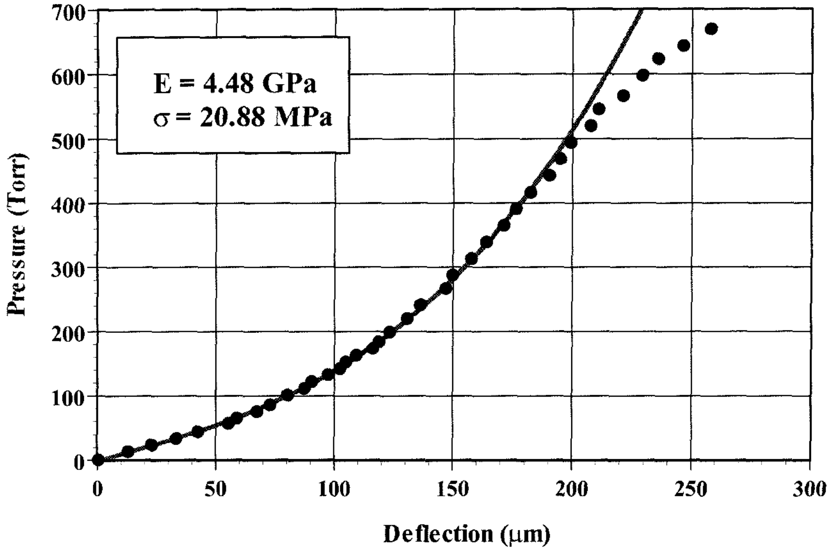

Figure 7-4 Load-Deflection Testing of Parylene Membrane

the wafer back side and a free-standing Parylene membrane was formed at the front side. Finally, another layer of 2 μm thick Parylene layer was deposited on the wafer from both sides. This layer of Parylene strengthened the anchor region of the membrane as indicated in Figure 7-3.

Similar load-deflection tests [5] as described in Section 6.4 were performed on these Parylene membranes. Figure 7-4 shows testing results for a 3.66 mm × 3.76 mm membrane. The Parylene thickness is 6.87 μm. By using the following equation to fit the experimental data [5],

$$P = \frac{C_1 \sigma t h}{a^2} + \frac{C_2 E t h^3}{a^4} \tag{7-1}$$

where

a, b: membrane dimensions,

P: applied pressure,

E: Young's modulus of the membrane material,

σ: residual stress in the membrane,

ν: Poisson's ratio of the membrane material, assumed to be 0.25 for Parylene,

t: thickness of the membrane,

h: deflection of the membrane,

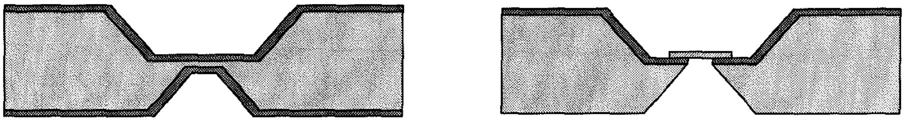

(a) KOH Etching and Silicon Nitride Deposition

(d) Back Side Silicon Nitride Etching

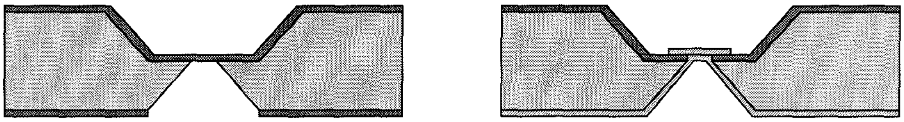

(b) Back Side Silicon Nitride and Silicon Etching

(e) 2nd Parylene Deposition

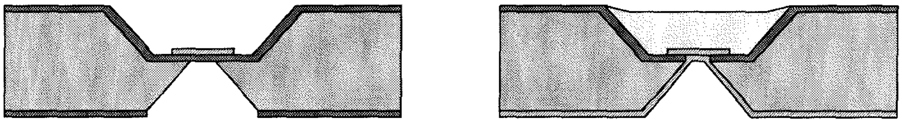

(c) 1st Parylene Deposition and Patterning

(f) Squeegee Coating of Silicone Rubber

Figure 7-5 Composite Silicone Rubber/Parylene Fabrication Process

n: a/b,

and for this membrane,

C_1=3.126,

C_2=1.929,

Young's modulus and residual stress of the Parylene film are found to be 4.48 GPa and 20.88 MPa.

7.2.3 Composite Silicone Rubber/Parylene Membrane

Load deflection tests show that both MRTV1 silicone rubber and Parylene C have a Young's modulus that is orders of magnitude lower than silicon. This suggests that it is possible to fabricate a fairly soft composite membrane in which Parylene serves as a vapor barrier and the silicone rubber layer provides good sealing and thermal insulation. This will be shown in Section 7.4 and 7.5.

Composite membranes were fabricated using a process similar to the squeegee coating process in Chapter 6 which is shown in Figure 7-5. To keep the membranes soft, a very thin layer of Parylene was used compared to the silicone thickness. As it was suspected that silicone absorbed the working liquid, Fluorinert™, the Parylene layer was sandwiched between the silicone rubber layer and the liquid. The process started with thermal oxidation of the wafers for 8 hours at 1050 °C. Then, the wafers were patterned to open up etching windows on both front and back sides. The wafers were then time etched in a 10% KOH solution at 58 °C to form two cavities. The top cavity was 5 mm x 5 mm and served as a mold for the silicone rubber. The bottom cavity served as the reservoir for the working fluid and defines the dimensions of the final composite membrane which was 2.7 mm x 2.7 mm. The 520 μm thick wafer was etched 235 μm on each side in KOH leaving a 50 μm thick silicon membrane. A layer of 0.5 μm thick low-stress silicon nitride film was deposited on both sides and the silicon nitride on the back side was removed using SF_6/O_2 plasma. The wafers were put back into KOH to etch away the silicon layer and a free-standing silicon nitride membrane was formed. Then, the wafers were put into a reactive ion etching chamber to roughen the surface with SF_6/Ar plasma at 60 mTorr pressure and 1000 W power followed by priming of A-174 Parylene adhesion promoter. A layer of 2 μm thick Parylene C was deposited and patterned at the bottom of the top cavity. Then, a layer of MRTV1 silicone rubber was squeegee molded into the top cavity. On the back side, silicon nitride was patterned using SF_6/O_2 plasma to free the membrane. Finally, another layer of 2 μm thick Parylene C was deposited on the back side to strengthen the edge of the membrane while the front side of the membrane was protected with dummy wafers in the deposition chamber. Due to the poor adhesion between silicone rubber and Parylene, the Parylene layer at the bottom of the top cavity has to be patterned to open the region for the silicone rubber to anchor to on the silicon nitride surface. Figure 7-6 is a SEM cross-section of the fabricated composite membrane. The membrane is about 180 μm thick.

A load deflection test was performed on the composite membrane and the result is shown in Figure 7-7. This confirms that the composite membrane is still very flexible. For example, the membrane deflects 134 μm at a pressure input of 4.1 psi. The deflections are more than what are needed for the valve applications as it will be shown later in Section 7.6.

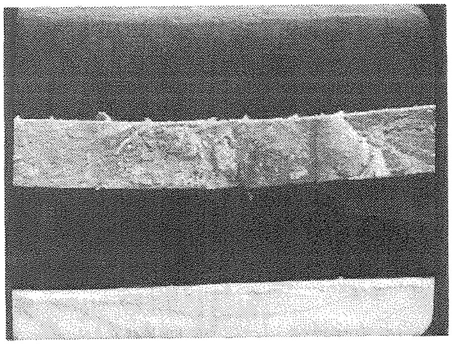

Figure 7-6 SEM Cross-Sectional View of a Composite Membrane

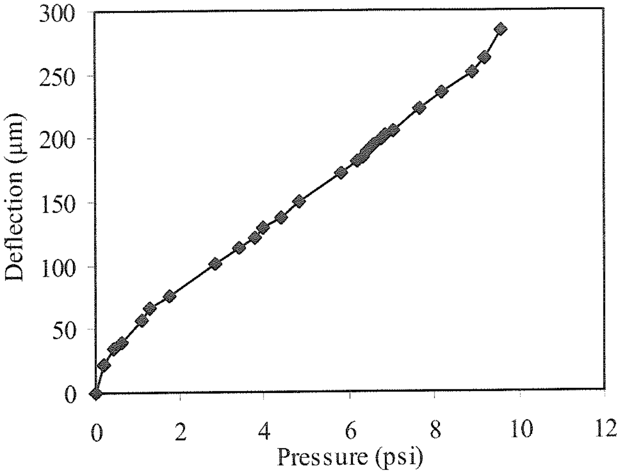

Figure 7-7 Load-Deflection Testing of a Composite Membrane

7.3 Free-Standing Silicon Nitride Membrane Heater

In order to reduce the power consumption of the valve, the thermal isolation of the valve structure must be improved. The previous valve had a heater sitting on a thick glass substrate. Because the thermal conductivity of glass is almost 20 times higher than the thermal conductivity of the working liquid, most of the heat went through the glass substrate rather than heating up the liquid. Here, a free-standing silicon nitride membrane heater is proposed. The gold heater would be fabricated on a thin silicon nitride membrane which would be suspended in the liquid. Due to the thin membrane and low thermal conductivity of silicon nitride, the heat loss would be significantly reduced. Gold is chosen as the heater material, not only because it has a high resistance to oxidation, but it also has the lowest thermal mismatch with silicon nitride among all the available metals in the lab. This is important as large thermal mismatch could potentially cause the heater to fracture when the temperature at the surface of the heater gets high.

The fabrication process for the silicon nitride membrane heater is shown in Figure 7.8. First, a layer of 0.5 µm thick LPCVD low stress silicon nitride was deposited

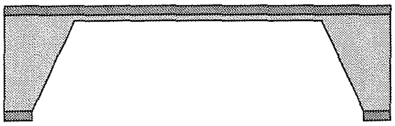

(a) SiN Deposition and Si Etching

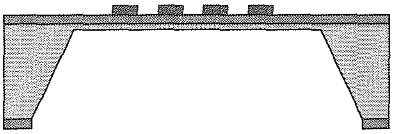

(b) Cr/Au Evaporation and Patterning

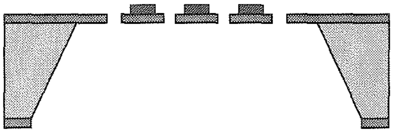

(c) SiN Etching, Dicing, and Releasing

Figure 7-8 Silicon Nitride Membrane Heater Fabrication Process

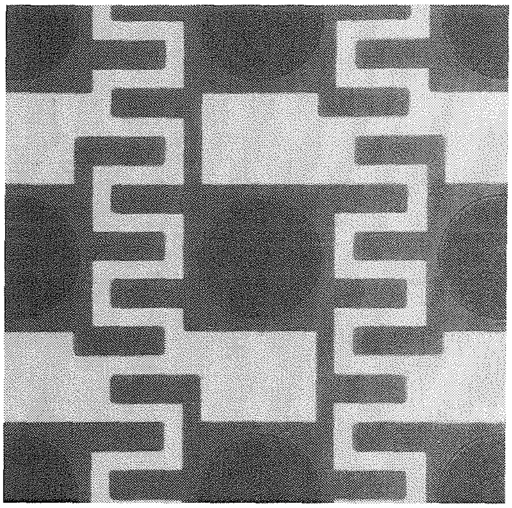

Figure 7-9 Picture of a Fabricated Heater

on the wafers at 850 °C with a SiH_2Cl_2/NH_3 gas flow ratio of 4/1. Then, the silicon nitride layer on the back side was patterned to open up the etching windows. The wafers were etched in a 10% KOH solution at 58 °C from the back side until only a 20 μm thick silicon layer was left. After that, a layer of 100 Å Cr/5000 Å Au was evaporated and patterned to define the heater. An array of 200 μm diameter holes was etched in the silicon nitride membrane using SF_6/O_2 plasma. Finally, the wafers were diced and put back into KOH solution to remove the 20 μm silicon layer to free the membranes. The reason that the membranes were freed after dicing is to avoid the potential damage of the membranes during dicing.

Figure 7-9 shows a fabricated heater. The array of holes equalizes the pressure across the membrane during the valve operation. Also, the gold square blocks between holes increase the heat conduction area and improve the frequency response of the thermopneumatic actuation.

The thermal performance of the silicon nitride membrane heater and glass substrate heater was studied and compared using an infrared thermal imager. Figure 7.10 shows two-dimensional temperature distribution on the heater surfaces. It can be seen that the silicon nitride membrane heater surface reached 200 °C with only 52.2 mW

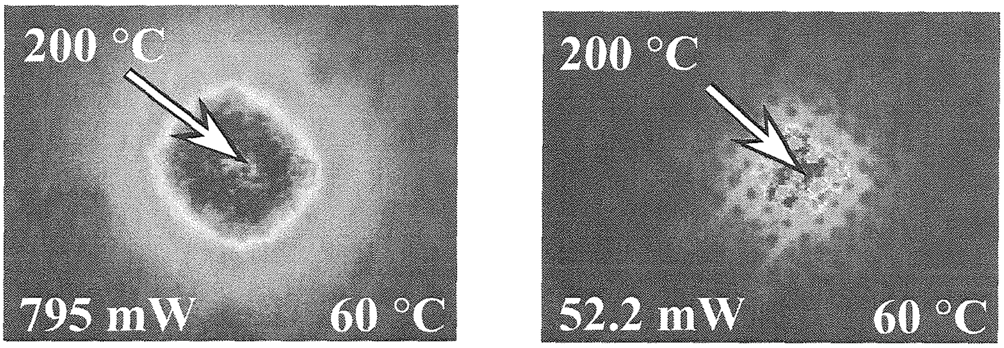

(a) Glass Heater (b) SiN Membrane heater

Figure 7-10 2-D Temperature Profile Measured Under Infrared Thermal Imager

power input while the glass heater required 795 mW power input for the same temperature. It should also be noted that the hot points on the silicon nitride membrane heaters are very localized. This confirms that the free-standing silicon nitride membrane provides better thermal insulation than the glass substrate.

7.4 Corrugated Valve Seat

A serious problem with today's micromachined valves is the non-trivial leak rate when the valve is supposed to be closed. This is caused by the stiction of the inevitable particles in the fluids around the inlet/outlet area. The previous valve had a valve seat that was fabricated on glass substrate using conventional mechanical drilling. The disadvantage of such an approach is that mechanical drilling is not a batch fabrication process, and it also creates debris around inlet/outlet area which makes the leakage problem worse. To address this problem, a novel bulk micromachined valve seat is proposed here. As shown in Figure 7-11, instead of two simple holes for the inlet/outlet, an array of 30 μm wide and 20 μm deep concentric grooves was etched into the silicon substrate by RIE with SF_6/O_2 plasma. These grooves reduce the chance of the particles sticking near the inlet/outlet. Also, by taking advantage of the elastomeric properties of silicone rubber, these grooves serve as redundant sealing rings so that even when there are particles, the silicone rubber should be able to fully encapsulate the particles without

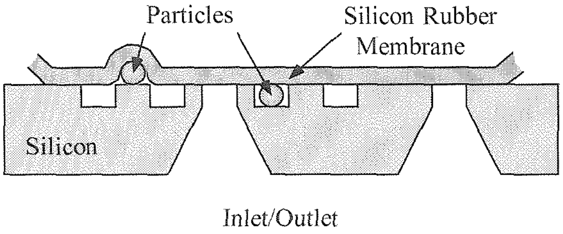

Figure 7-11 New Valve Seat Design

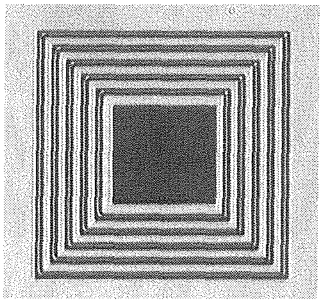

Figure 7-12 Picture of a Fabricated Valve Seat

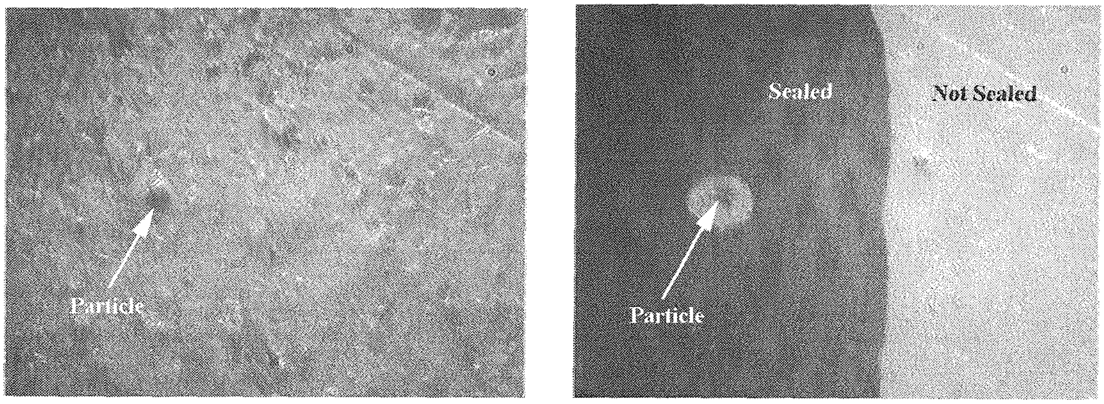

(a)

(b)

Figure 7-13 Good Sealing Achieved with Silicone Rubber Membrane

compromising the performance of the valve. Valve seats with 400 μm and 600 μm square inlet/outlet were fabricated using bulk micromachining. Figure 7-12 shows a fabricated valve seat.

The good sealing properties of silicone rubber on rough surfaces or surfaces stuck with particles were demonstrated in Figure 7-13. In this experiment, a piece of glass was mounted on top of a composite membrane. Figure 7-13 (a) shows a particle stuck on the glass plate. With 2 psi pneumatic pressure load applied to the membrane from the back side, the silicone rubber membrane fully encapsulated the particle as shown in Figure 7-13 (b).

7.5 Thermopneumatic Actuation

The actuation mechanism of this valve is similar to what is described in Section 6.5. Basically, a cavity bounded by a flexible membrane on one side is sealed with fluid. When the fluid in the cavity is heated, it expands and deflects the membrane. In this section, the steady state and transient response of the thermopneumatic actuation with various working liquids are examined.

7.5.1 Temperature Coefficient of Resistance of Gold

The direct way to study thermopneumatic actuation is to measure the membrane deflection as a function of the power input to the resistive heater. However, to fully understand thermopneumatic actuation and its performance, this information itself will not offer any insight. It would be very helpful to know the temperature information inside the cavity. Although finding out the three-dimensional temperature distribution inside the cavity is very difficult, the temperature on the heater surface under different conditions can be calculated based on the fact that the resistance changes with the temperature. For conductors, the change in resistance as function of temperature is generally given by temperature coefficient of resistance (TCR), α. For moderate temperature change, for example, from 0 to 100 °C, the resistance as a function of the temperature is approximately given by the following equation,

$$R = R_0[1 + \alpha(T - T_0)] \tag{7-2}$$

where

T: temperature,

T_0: reference temperature,

R_0: the resistance at T_0,

R: the resistance at T,

α: TCR.

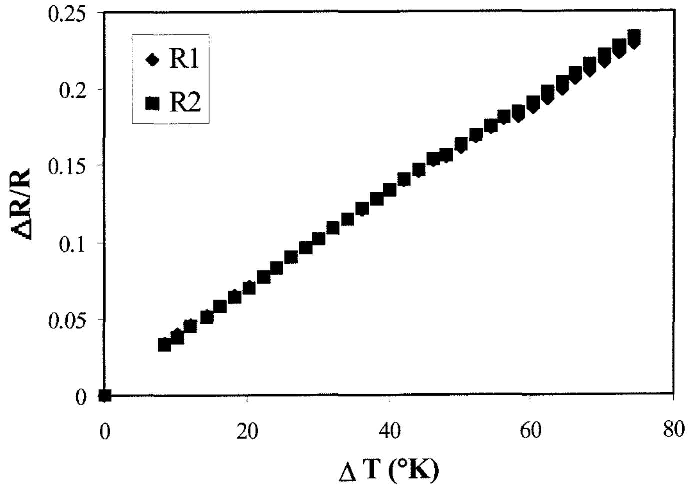

Figure 7-14 Temperature Coefficient of Resistance of Gold

It is generally accepted that between 0 and 100 °C, α is roughly constant. If the resistance and α are known, the temperature can be calculated using Equation 7-2.

To calibrate the TCR of gold which is the material for the resistive heater, two gold heaters on silicon nitride membrane with different designs were setup in a temperature controlled environment chamber. By slowly increasing the temperature and measuring the corresponding resistance change with a multimeter, the relationship between the resistance and temperature was obtained. At 25.8 °C, the resistance of R_1 and R_2 were 40.50 Ω and 31.84 Ω respectively. The resistance change was measured up to 100 °C. Plotted in Figure 7-14 is relative resistance change, $(R-R_0)/R$, as a function of temperature change, $(T-T_0)/T$. The two data series fall on a single line and the slope represents the TCR of gold. The TCR was found to be 0.003/°C. It should be noted that there are two possible errors which affect the measurement result. First, due to the thermal mismatch between silicon nitride and gold, the strain developed in the gold film as the temperature increases could change the resistance. Second, part of the resistance change was from the contact. However, since these two mechanisms will show up in real thermopneumatic actuation measurements, even though they will not behave exactly in the same way as in above calibration experiment, for first order average temperature estimation, the above measured TCR is accurate enough.

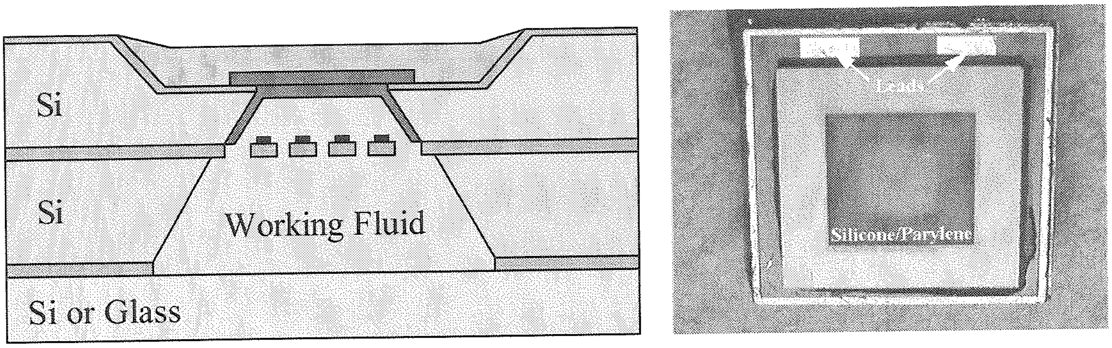

(a) Cross-Sectional View

(b) Picture

Figure 7-15 Thermopneumatic Actuator

7.5.2 Steady State Response of Thermopneumatic Actuation

To study the steady state response of thermopneumatic actuation with various working fluids, a variety of actuators were assembled by gluing the gold silicon nitride membrane heater to the bottom of the membrane chip and sealing the formed cavity with a glass backing plate. The cross section of the actuator is shown in Figure 7-15 (a) and Figure 7-15 (b) shows an assembled actuator. Actuation was observed by applying a fixed amount of power to the cavity and measuring the deflection of the membrane from its rest position under a microscope with a calibrated focus. Enough time was given between measurement points to make sure the actuator reached thermal equilibrium.

The opening at the bottom of the membrane chip is designed to be 3 mm × 3 mm. It is unknown what the optimal size of the heater should be. Obviously, the size of the heater should not be larger than 3 mm × 3 mm as otherwise the heater would directly contact the silicon membrane frame and heat would dissipate away. However, with a too small heater, it would take a long time to heat up the fluid and the frequency response would be very slow. To find out which one is better, heaters with sizes 2.9mm × 2.9mm, 2.1 mm × 2.1 mm and 1.1 mm × 1.1 mm were designed, fabricated and tested. Experimentally, it was found that heaters with an area 1.1 mm × 1.1 mm and 2.1 mm × 2.1 mm have similar steady state thermopneumatic actuation performance; however, as it was expected, it took a longer time for a 1.1 mm × 1.1 mm heater to reach thermal equilibrium between measurement data points. For the same amount of deflection, a

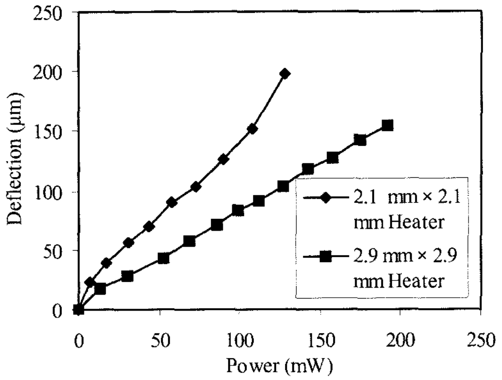

Figure 7-16 Thermopneumatic Actuation with Different Heaters

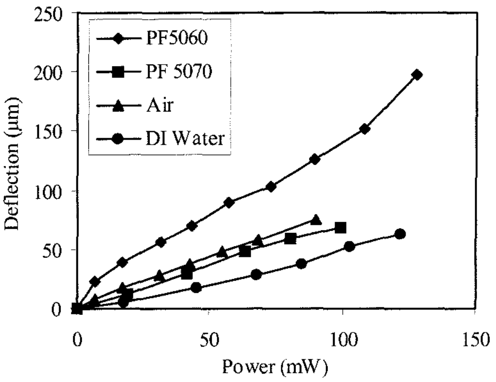

Figure 7-17 Thermopneumatic Actuation with Different Working Fluids

2.9 mm × 2.9 mm consumed more power than a 2.1 mm × 2.1 mm heater. The result is shown in Figure 7-16. This suggests that 2.1 mm × 2.1 mm heaters give better performance than the other two heaters and should be used for the valves.

Figure 7-17 shows the thermopneumatic actuation results for DI water, Fluorinert™ (PF 5060, PF 5070) and air. With the same power input to the heater, the actuator sealed with PF-5060 achieved the highest deflection among all the liquids.

By using the TCR of gold, the average temperature across the heater surface was calculated and plotted as a function of power input as shown in Figure 7-18. It should be pointed out that since the temperature across the heater surface was not uniform, the temperature plotted is average temperature. By using Fourier's law of heat conduction, equivalent thermal conductance with each fluid can be estimated even though the thermopneumatic actuator is a complicated three-dimensional structure.

$$q = G_{eq} \Delta T = \frac{kA_{eq}}{L_{eq}} \Delta T \tag{7-3}$$

where

q: power consumption,

k: thermal conductivity of working liquid,

G_{eq}: equivalent thermal conductance,

A_{eq}: equivalent surface area,

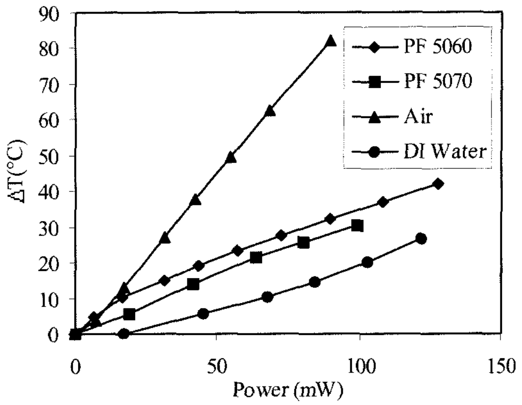

Figure 7-18 Power *Vs.* Temperature Change

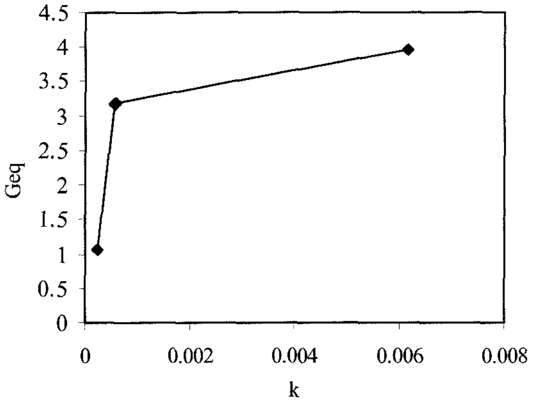

Figure 7-19 G_{eq} *Vs.* k

L_{eq}: equivalent distance,

ΔT: temperature change.

Figure 7-18 shows that power consumption is approximately a linear function of the temperature change and the slope should be the equivalent thermal conductance for different fluids. Assuming A_{eq} and L_{eq} are the same for actuators with different fluids, the thermal conductance should be a linear function of thermal conductivity as suggested in Equation (7-3). The thermal conductivities of PF 5060, PF 5070, air and DI water at room temperature were found to be 5.7×10^{-4} W/cm·°C, 6×10^{-4} W/cm·°C, 2.4×10^{4} W/cm·°C, and 6.2×10^{-3} W/cm·°C respectively. In Figure 7-19, the equivalent thermal conductance (G_{eq}) is plotted as a function of thermal conductivity (k) of various fluids, and as expected, the higher the thermal conductivity, the higher the thermal conductance. This means with the same power input, the lower the thermal conductivity of the fluid is, the higher the temperature that can be achieved. This is exactly what was observed in the experiments. In fact, tests with an air filled cavity resulted in heater damage at high power and also plastic deformation in the silicone/Parylene membrane.

Since the average temperature across the heater is known, the deflection achieved with various working fluids is plotted as a function of the temperature in Figure 7-20. Assuming the membrane is extremely soft, i.e., it requires very little force to deflect the membrane, the deflection will be a result of thermal expansion.

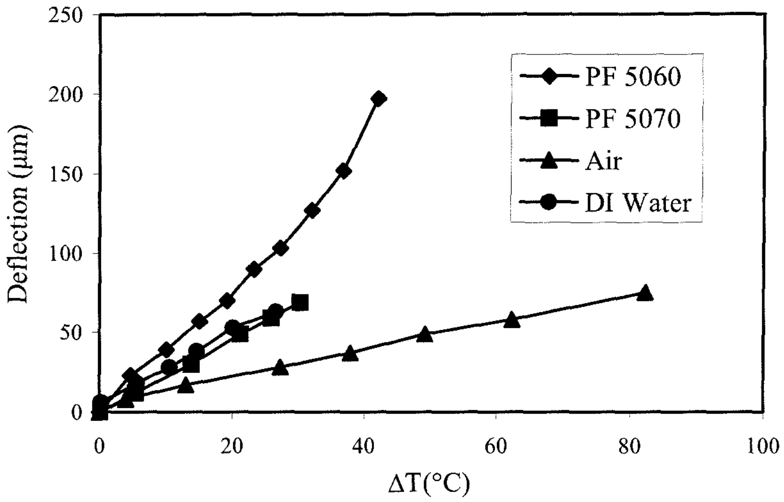

Figure 7-20 Deflection *Vs.* ΔT

$$\frac{\Delta V}{V} = \beta \Delta T \qquad (7\text{-}4)$$

where

ΔV/V: relative volume change,

β: coefficient of thermal expansion,

ΔT: temperature change.

To the first order, this agrees with the results shown in Figure 7-20. For example, at room temperature, the coefficient of thermal expansion of PF 5060 is six times greater than the one of water. Figure 7-20 shows that at the same temperature, the deflection achieved with PF 5060 was much larger than the one achieved with water, air or PF 5070.

In summary, thermal conductivity of the working fluid plays an important role in keeping power consumption low. Large deflections can be achieved with a large thermal expansion coefficient. Although air has a very low thermal conductivity, Fluorinert™ PF5060 has a very large thermal expansion coefficient and the combined contribution from both thermal conductivity and thermal expansion coefficient gives PF5060 the best steady state thermopneumatic performance.

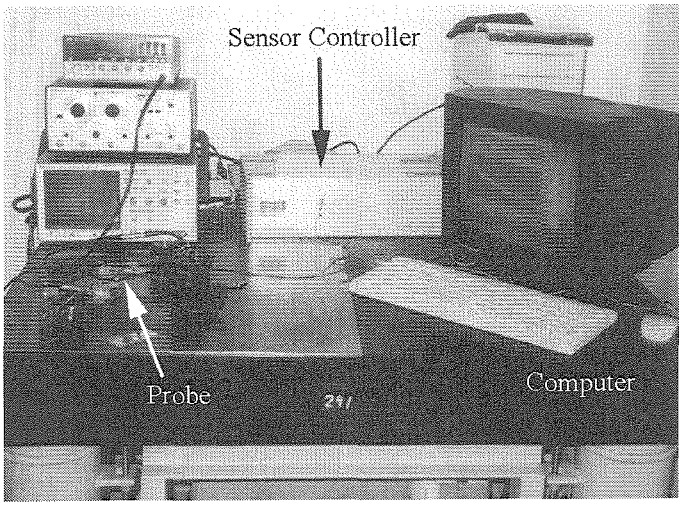

Figure 7-21 Picture of the Transient Experiment Setup

7.5.3 Transient Response of Thermopneumatic Actuation

Transient response of thermopneumatic actuation has also been studied by using the method of laser interferometry. Figure 7-21 shows the testing setup. The laser interferometer (Model PD-1000, Precision-Dynamics, Inc. [6]) uses a class IIIb laser (wave length 780nm) and consists of a probe, a sensor controller, and PC with LabVIEW to collect data. By applying a square wave to the heater of the thermopneumatic actuator, the deflection of the actuator as a function of time was measured using a laser interferometer.

In most cases, the response has two time constants, a short one which is associated with heating/cooling the working liquid in the cavity and a long one which is associated with heating/cooling the whole chip package. The heat transfer in the thermopneumatic actuator is governed by the following differential equation,

$$\frac{\partial^2 T}{\partial x^2}+\frac{\partial^2 T}{\partial y^2}+\frac{\partial^2 T}{\partial z^2}=\frac{\rho C_V}{k}\frac{\partial T}{\partial t}=\frac{1}{\alpha}\frac{\partial T}{\partial t} \tag{7-5}$$

where

T: temperature distribution,

ρ: density of the working fluid,

Table 7-2 Thermal Properties of Working Fluids and Calculated Time Constant

Fluid	Density ρ (kg/m^3)	Specific Heat C_v (J/kg ·°C)	Thermal Conductivity k (W/m·°C)	Calculated Time Constant τ (s)
PF 5060	1.68×10^3	1.046×10^3	5.7×10^{-2}	1.93
PF 5070	1.73×10^3	1.68×10^3	6×10^{-2}	1.88
Air	1.161	1.007×10^3	2.4×10^{-2}	0.43
Water	1×10^3	4.184×10^3	6.154×10^{-1}	0.003

C_V: specific heat of the working fluid,
K: thermal conductivity of the working fluid,
α: thermal diffusivity of the working fluid,
t: time.

The thermal performance of the actuator can be analyzed by solving Equation (7-5) with appropriate boundary conditions and initial conditions. However, because the actuator is a very complicated three-dimensional thermal structure, solving the equation requires finite element analysis. "Order of magnitude" estimation of the first time constant can be obtained by modeling heat conduction as an analog of electrical conduction. In a thermal system, energy is stored; in an electrical system, charge is stored. The flow of energy is called heat; the flow of charge is electrical current. The analog of electrical resistance is thermal resistance,

$$R_{th} = \frac{\Delta x}{kA} \tag{7-6}$$

where
k: thermal conductivity,
Δx: thickness,
A: area through which heat flows.

Table 7-3 Measured Time Constants Under Various Conditions

Condition	Power (mW)	Deflection (μm)	Heating Time Constants (s)	Cooling Time Constants (s)
PF 5060	42.5	45	1.7, 38.2	2.1, 37.0
PF5060 (On Heat Sink)	42.5	33	1.5, 7.1	1.8, 9.4
PF 5070	40	30	2.5, 32.0	2.7, 32.0
DI Water	93	43	1.6, 45.8	1.7, 45.8
Air	50	35	1.3, 40.7	1.2, 46.2

The analog of electrical capacitance is thermal capacitance,

$$C_{th} = \rho C_v V \tag{7-7}$$

where

ρ: density of the working fluid,

C_V: specific heat of the working fluid,

V: volume.

The thermal diffusivity of the working fluid, α, is a measure of how fast the temperature of the fluid responds to change in heat flux. To maximize the rate of change of temperature, α of the working fluid should be maximized.

The thermal properties of the working fluids and estimated first time constant for actuators with corresponding fluid (assuming a 250 μm distance) are listed in Table 7.2 while the measured time constants under various conditions are listed in Table 7.3. It can be seen from both tables that the time constants of actuators with Fluorinert^{TM} are on the order of a few seconds while the water filled actuator has time constants on the order of 1 second because water has a higher thermal conductivity. However, there is a large difference between measured time constant and estimated time constant. It is suspected that there was another very short time constant that the laser interferometer did not pick

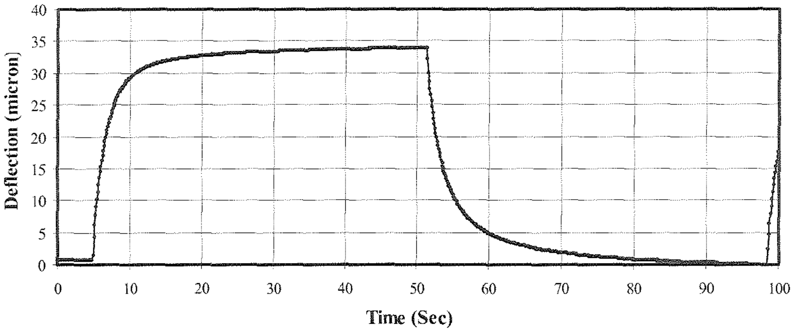

Figure 7-22 Transient Response

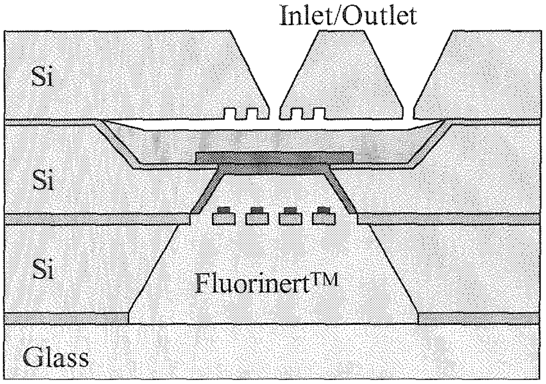

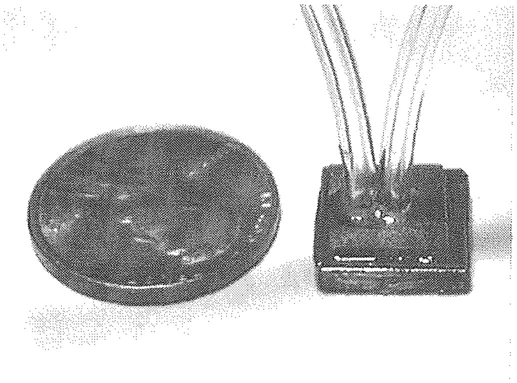

Figure 7-23 Cross Section of the Valve

Figure 7-24 Picture of a Valve

up because the laser interferometer was operating at a very low sampling rate during the expriments. Among all the actuators with different fluids, the actuators with air as the working fluid has the shortest time constant. The reason is although air has a very low thermal conductivity, its density is dramatically lower than all the other fluids.

Also, the package design of the actuators will also change the response. By using a silicon backing plate for the actuator or attaching a metal heat sink underneath the actuator, the response of the actuator will be faster. For example, as shown in Table 7-3, an actuator with PF 5060 as the working fluid has heating time constants of 1.7 sec and 38.2 sec, cooling time constants of 2.1 sec and 37.0 sec. When a metal heat sink is attached, the heating time constants become 1.5 sec and 7.1 sec and cooling time constants become 1.8 sec and 9.4 sec. The response is plotted in Figure 7-22.

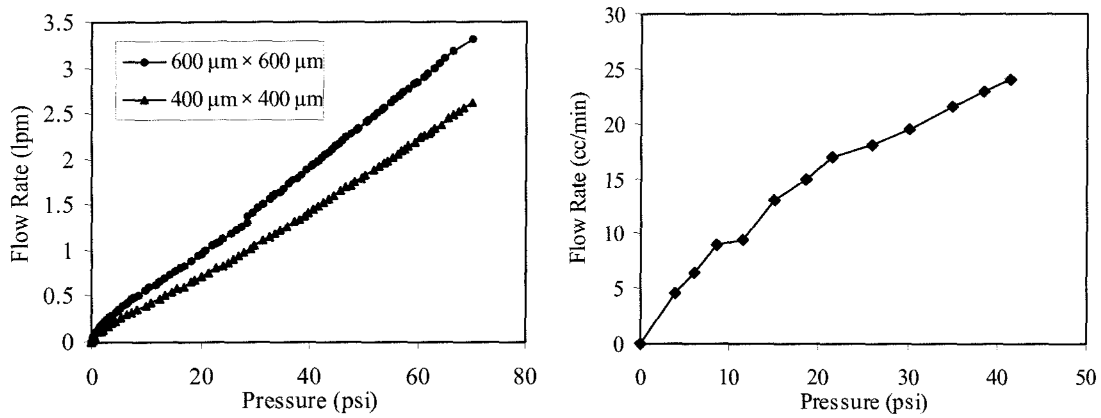

(a) Nitrogen (b) Water

Figure 7-25 Flow *Vs*. Pressure with Nitrogen and Water

The improvement of frequency response, however, is not achieved without any sacrifice. In any thermal system without active cooling, better insulation reduces power consumption, but it also slows down the frequency response. There is always a trade-off between power consumption and operation speed. This can clearly be seen from Table 7-3. By attaching a heat sink, the frequency response was improved, but at the same power consumption, the deflection was much smaller.

The goal of the work in this thesis is to develop a low power consumption MEMS valve. Time constants on the order of a few seconds are acceptable. Therefore, based on the steady state and transient experiment results, Fluorinert^{TM} PF 5060 is chosen as the working fluid for the thermopneumatic actuation.

7.6 Thermopneumatic Valve

As shown in Figure 7-23, valves were made by assembling a valve seat die, membrane chip die, heater die, and backing plate. Flexible plastic Tygon$^{®}$ tubes (i.d. 1/32 inch, o.d. 3/32 inch) were attached to valve inlet/outlet with epoxy. Figure 7-24 is a picture of a fully packaged valve. It should be noticed that the 50 to 60 µm recess of the cured silicone rubber film defined the gap between the membrane and valve seat, which simplified the fabrication of the valve seat. As suggested by the thermopneumatic actuation results, all the valves were fully filled with Fluorinert™ PF 5060.

7.6.1 Flow *Vs*. Pressure

The flow path in the valve consists of the tubing, the nozzle/diffuser shaped inlet/outlet defined by anisotropic etching and the gap between the valve chip die and the membrane. Fluid mechanics estimation using the simple equation of flow through circular pipes [7] shows that the pressure drop across the tubing is negligible. It is possible that the inlet/outlet contribute to part of the flow resistance. If that is the case, they should be designed as large as possible. But, excessively large openings would require large membrane deflections to close the valve. To find out how the opening affects flow through valve, valve seats with two different sizes of inlet/outlet holes, $400 \times 400\ \mu m^2$ and $600 \times 600\ \mu m^2$, were designed and their flow performance was tested with nitrogen and water. The testing setup will be described in detail in Section 7.6.2 and 7.6.3. Flow rate through the valve as a function of pressure drop across valve was measured. Because the valve components were aligned and assembled with epoxy manually, the results varied. Typical results were plotted in Figure 7-25. First, it can be seen that the flow rate is almost a linear function of the pressure drop, which agrees with fluid mechanics theory of laminar viscous flow through pipes or between parallel plates. Second, the results in Figure 7-25 (a) show that the size of the inlet/outlet does affect the flow rate. For example, for a flow rate of 1 liter/min, the pressure drop across a valve with $400 \times 400\ \mu m^2$ inlet/outlet is about 29 psi while the $600 \times 600\ \mu m^2$ one is only 20 psi. Third, fluid mechanics theory suggests that the flow rate is inversely proportional to the viscosity of the fluid. This was confirmed in the experiment. It is known that viscosity of water is 100 times of the viscosity of nitrogen. In Figure 7-25 (b), it shows that flow rate of water through the valve is on the order of tens of cubic centimeter per minute, which is about 100 times smaller than the flow rate of nitrogen.

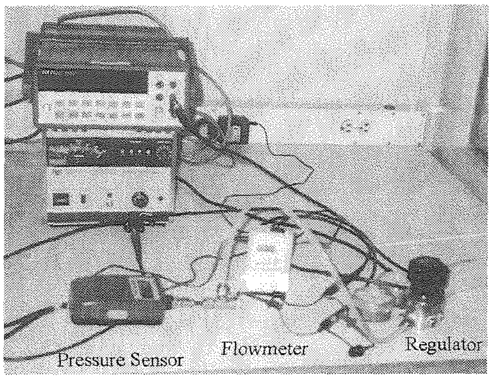

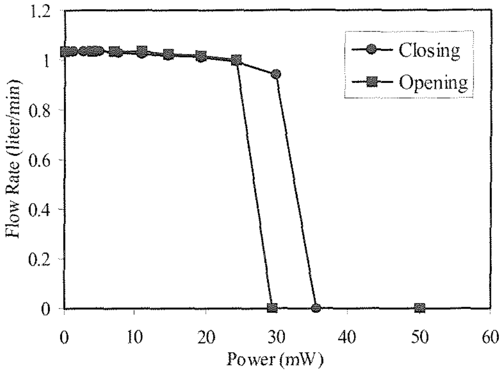

Figure 7-26 Nitrogen Test Setup

Figure 7-27 Flow Rate *Vs*. Power

7.6.2 Valve Performance with Nitrogen

Various valves were assembled and tested with the setup shown in Figure 7-26. Compressed nitrogen and a pressure regulator were used to provide flow up to 5 liter/min and pressure up to 75 psi. An HP 6115A precision power supply was connected to the heater of the valve and the current was measured with an HP 34401A multimeter. Pressure and flow rate were measured with a pressure sensor (Omega, Model HHP 4100, 0.1 psi resolution) and a flowmeter (Cole Parmer, Model 32916, 0.01 liter/min resolution).

Due to the manual alignment and assembling process, the testing results varied. Take a valve with 400 × 400 μm^2 inlet/outlet and fully filled with PF 5060 as an example. At an inlet pressure of about 30 psi and a flow rate of about 1 liter per minute, the power required to close the valve usually varied between 40 mW and 70 mW. The lowest power consumption achieved is shown in Figure 7-27. In this case, 35.5 mW was sufficient to shut off a flow of 1.04 liter per minute at the inlet pressure of 33 psi. By using the measured TCR of gold, the average temperature on the heater surface was 20 °C above room temperature. Another valve which had similar construction, except there was a 1 mm size bubble in the actuation cavity, required a power of 139 mW to close valve under the similar testing conditions. At that power input, the average temperature at the heater surface was found to be 50 °C above room temperature.

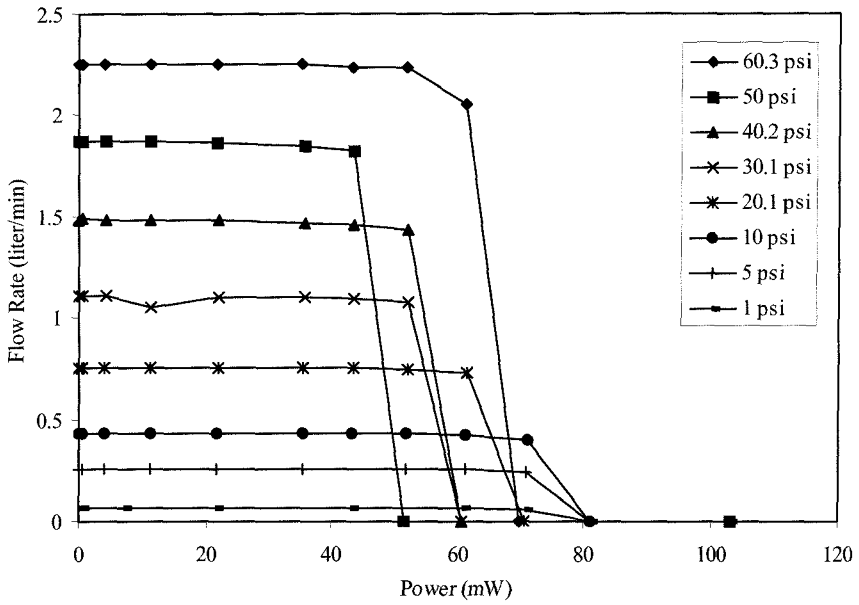

Figure 7-28 Valve Performance at Various Inlet Pressures

The valve could operate in two different modes, thermal expansion or vapor pressure change. In thermal expansion, the actuation cavity is fully filled with liquid and when the liquid is heated, the liquid expands, deflects the membrane upward, and closes the valve. But when there is a bubble in the cavity, the vapor pressure of the liquid is a strong function of temperature. When the liquid is heated to the temperature at which the vapor pressure is greater than the inlet pressure, the membrane moves upward to close the valve. The above experiment can help determine which operation mode can give better performance. From data sheet provided by Fluorinert^{TM} manufacturer 3M, the vapor pressure of PF 5060 at 45 °C and 75 °C are 11 psi and 29 psi. This showed that in above experiments, the valve fully filled with PF5060 was operated in thermal expansion mode while the valve that had a bubble was actuated based on vapor pressure change of the working liquid. The experiment results also suggest that for low power consumption, the valve should be fully filled with PF5060 and operated by thermal expansion.

It was found from experiments that although valves with 600 × 600 μm^2 inlet/outlet had lower pressure drops than the ones with 400 × 400 μm^2, they required much higher power input to close the valve. The reason for this is since the inlet/outlet were larger, higher deflections were needed in order to seal them.

In another experiment, a valve, which had 400 × 400 μm^2 inlet/outlet and was fully filled with PF 5060, was tested at inlet pressure from 1 psi to 60.3 psi. The corresponding flow rate was from 0.07 to 2.25 liter per minute. Figure 7-28 shows the testing results. At high inlet pressure and high flow rate, it took 50 to 70 mW to close the valve. However, the power consumption did not drop for low inlet pressure. For example, even at 1 psi, the valve needed 81 mW to close a flow of 0.07 liter per minute. Compared to the power consumption of higher inlet pressure, this one was at least 10 mW higher. Calculation based on gold TCR shows the average temperature on the gold surface is in the range of 53 to 62 °C corresponding to power consumption of 50 to 80 mW.

The pressure generated inside the cavity can be approximately expressed by the following equation:

$$\Delta P = E(\beta \Delta T - \frac{\Delta V}{V}) \tag{7-8}$$

where

E: bulk modulus of elasticity,

β: thermal coefficient of expansion,

ΔT: temperature increase,

$\Delta V/V$: relative volume change.

$\beta \Delta T$ represents the relative volume change due to temperature change. $\Delta V/V$ is the required volume change for the membrane to deflect and seal the valve inlet/outlet. Before the membrane touches the valve seat, $\beta \Delta T$ is smaller than $\Delta V/V$ and very little pressure is generated inside the cavity assuming the membrane is assumed to be very flexible. After the membranes touch the valve seat, $\Delta V/V$ does not increase that much because the membrane can not freely move upward. However, the liquid inside the cavity has to expand as the result of heating. When this expansion is restricted, pressure is generated inside the cavity. Because liquid generally has a very large bulk modulus, the generated pressure can be huge. Unfortunately, the bulk modulus of PF 5060 is not

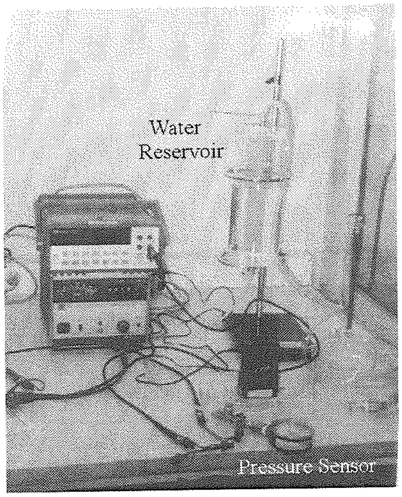

Figure 7-29 Water Test Setup

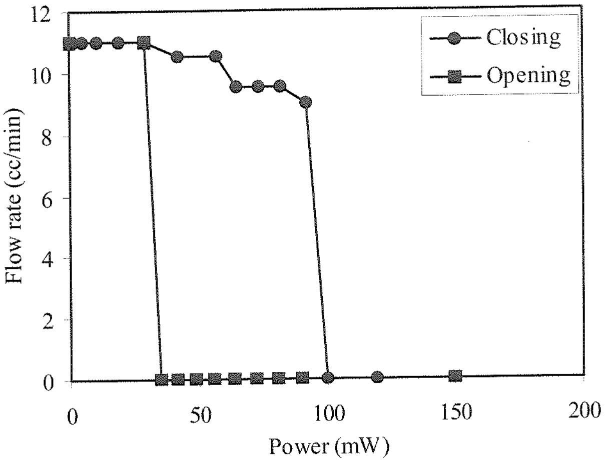

Figure 7-30 Flow *Vs*. Power

available from the manufacturer. Take water as an example. Water has a bulk modulus of 3.3×10^5 psi, which means in order to generate 60 psi, only 0.02% volume change is needed. Since PF 5060 has a thermal expansion coefficient of 0.16%/°C, the pressure can be generated by raising the temperature of PF 5060 by less than 0.1 °C if its volume is held constant. The point is because of the huge bulk modulus of liquid, the volume of cavity and hence the temperature and power consumption do not change that much for different inlet pressures. The higher power consumption of the valve at lower inlet pressure can be explained by the fact that when the inlet pressure is low, the cavity is free to expand. As a result of this expansion, there is a larger contact area between the membrane and silicon valve seat and this causes higher heat loss due to the very high thermal conductivity of silicon.

7.6.3 Valve Performance with Water

Valves were also tested with water. The test setup is shown in Figure 7-29. It was similar to the nitrogen testing setup except that a water reservoir pressurized with compressed nitrogen served as water source. The water pressure is regulated by monitoring the pressure of compressed nitrogen. Inlet pressure to the valve was measured with a water pressure sensor while the flow rate was measured with a graduated cylinder and a stop

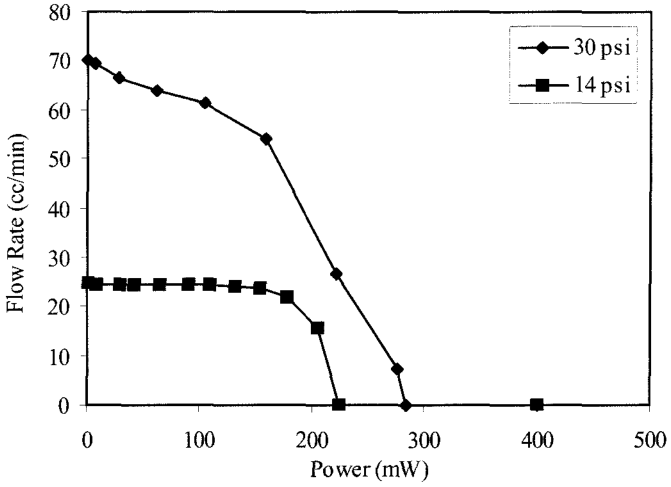

Figure 7-31 Flow *Vs.* Power at Various Inlet Pressures

watch. Figure 7-30 shows testing results with inlet pressure of 32 psi and flow rate of 11 cc per minute. The valve used in this case was the same one that achieved lowest power consumption for nitrogen flow. In this case, it took 100 mW power to close the valve and at that power input, the average temperature on the heater surface was 35 °C above room temperature. For the same inlet pressure, it required an extra 65 mW of power to close the water flow *vs.* the nitrogen flow. The cause of the higher power consumption is due to the convection heat loss to the water flow. This also explains the large hysteresis shown in Figure 7-30. It took more power to heat up the liquid and close the valve, but once the valve was closed, there was no convection heat loss and it took less power to keep the valve closed.

Figure 7-31 shows the testing results with inlet pressure of 32 psi and 14 psi. The valve used had 600 × 600 μm^2 inlet/outlet. The flow rate was higher, but it took much higher power input to close the valve.

7.7 Conclusion

A normally open, low power thermopneumatic MEMS valve utilizing a composite silicone rubber/Parylene membrane has been designed, fabricated, and tested. A novel suspended silicon nitride membrane heater has been developed to reduce heat loss. By using a “soft” membrane with a large gap and thermopneumatic actuation, high flow rates are achievable while still keeping power consumption low. A new valve seat has been developed to reduce the leak rate of the valve when the valve is closed. The steady state and transient response of the thermopneumatic action with various working liquids have been studied and the results show that Fluorinert^{TM} PF 5060 deliver the best thermopneumatic performance. Valves of various constructions have been tested extensively with nitrogen and water flow. A very low power consumption has been demonstrated. A power of 35.5 mW is sufficient to control a nitrogen flow of 1.04 lpm with an inlet pressure of 32 psi.

Bibliography

[1] X. Yang, C. Grosjean, Y. C. Tai, and C. M. Ho, "A MEMS Thermopneumatic Silicone Membrane Valve," Proceedings of IEEE Workshop on Micro Electro Mechanical Systems (MEMS'97), pp. 114-118, Nagoya, Japan, January 1997.

[2] X. Yang, C. Grosjean, Y. C. Tai, and C. M. Ho, "A MEMS Thermopneumatic Silicone Rubber Membrane Valve," Sensors and Actuators A, 64, pp. 101-108, 1998.

[3] *Parylene Conformal Coatings Specifications and Properties*, Specialty Coating Systems, Inc., 5707 West Minnesota Street, Indianapolis, IN 46241, Tel: (800)356-8260, Fax: (317)240-2073.

[4] O. Tabata, K. Kawahata, S. Sugiyama, and I. Igarashi, "Mechanical Property Measurements of Thin Films Using Load Deflection of Composite Rectangular Membranes," Sensors and Actuators A, 20, pp. 135-141, 1989.

[5] X. Q. Wang, X. Yang, K. Walsh, and Y. C. Tai, "Gas Phase Silicon Etching with Bromine Trifluoride," Technical Digest, International Conference on Solid-State Sensors and Actuators (Transducers'97), Vol. 2, pp. 1505-1508, Chicago, June 1997.

[6] Precision-Dynamics, Inc., 1155 Appleby Lane, Unit E8, Burlington, Ontario, Canada, L7L 5H9, Tel: (905)332-7192, Fax: (905)332-1808.

[7] F. M. White, *Fluid Mechanics (Second Edition)*, pp. 306, McGraw Hill, Inc., 1986.

[8] X. Yang, C. Grosjean, and Y. C. Tai, "Thermopneumatically Actuated Microvalves and Integrated Electro-fluidic Circuits," Technical Digest, Solid State Sensor and Actuator Workshop (Hilton Head '98), pp. 616-319, Hilton Head Island, South Carolina, USA, June 1998.

Chapter 8

Conclusion

Review of the history and current research of MEMS shows that the application of MEMS and microfluidics will potentially have a tremendous impact on biological and chemical analysis. In this thesis, several microfluidic devices have been developed.

First, various particle membrane filters (8×8 mm^2) with circular, hexagonal, and rectangular filtering holes have been designed, fabricated, and tested. By varying hole dimensions from 6 to 12 μm, opening factors from 4% to 45% are achieved. A composite silicon nitride/Parylene membrane technology is developed to enhance filter strength. Fluid dynamic performance of the filters has been studied extensively through experiments and numerical simulations. It is found that the gaseous flow in the filters strongly depends on opening factors. Furthermore, the measured pressure drops are much lower in comparison to numerical simulation results. Numerical calculation with a slip boundary condition shows that surface velocity slip can only account for a minor part of the difference.

High flow rate, high pressure range, and low power consumption valves require large actuation deflections and forces. Electrostatic, electromagnetic, bimetallic, and thermopneumatic actuation have been studied and compared. The results show that thermopneumatic actuation can provide the largest actuation force among the four. To achieve large deflection, the mechanical performance of the membrane has been examined. Microbellows structure and low modulus materials (silicone rubber and Parylene) are proposed to achieve large deflection and small size in the valve actuator.

Three key technologies for microbellows design and fabrication have been studied. First, LPCVD polysilicon has been explored as the sacrificial layer for surface micromachined process. Channels and membranes have been designed and fabricated, and etch rates of the polysilicon sacrificial layer in TMAH under various conditions have been calibrated. Etch stop characteristics of heavily boron doped polysilicon in TMAH have also been explored. Good etch stop has been achieved with boron doping concentration of $8\times10^{20}/\mathrm{cm}^3$. Polysilicon sacrificial layer etching using gas-phase BrF_3 has also been tried. This vapor etching is tension free and hence completely avoids the problem of structure stiction. Second, the cracking of surface micromachined structures during the final freeing process has been studied. Straight channels, circular, and square membranes have been design, fabricated, and tested. The cracking behavior can be qualitatively explained using the Griffith criterion. It is found that relaxation of residual stress in the structural layer is responsible for the structure cracking. Several guidelines for successful design and fabrication of MEMS devices are provided based on this analysis. Finally, the strength of surface micromachined membranes is experimentally studied. It is found that the membrane strength strongly depends on the membrane boundary conditions. A new fabrication technique without changing the mask and fabrication process is proposed to improve the common step-up boundary condition. Membranes with diameters from 200 μm to 800 μm and three different boundary conditions have been fabricated and tested. The application of this technique to other surface micromachined structures such as cantilever beams is also described.

Two generations of microbellow actuators have been successfully developed using surface micromachining technology. With polysilicon as the sacrificial layer, the structure of the microbellows has been optimized to achieve large deflection and high strength. Experimentally, it has been shown that the microbellow can deliver more than three times the deflection of a flat membrane of the same size. Also, thermopneumatic actuators using the microbellows has been demonstrated. The microbellow actuators are very promising and suitable for microvalve and micropump applications.

Several methods for fabricating silicone rubber membranes and integrating them with micromachined components to make actuators and valves have been developed. The silicone rubber has been characterized and has been found to have many desirable properties including high elongation, good sealing, low modulus of elasticity, and compatibility with IC processes. A thermopneumatically actuated valve has been successfully demonstrated. It was shown that 280 mW will close a 1.34 lpm air flow at 20 psi.

A normally open low power thermopneumatic MEMS valve utilizing a composite silicone rubber/Parylene membrane has been designed, fabricated, and tested. A novel suspended silicon nitride membrane heater has been developed to reduce heat loss. By using a “soft” membrane with a large gap, and thermopneumatic actuation, high flow rates are achievable while still keeping power consumption low. A new valve seat has been developed to reduce the leak rate of the valve when the valve is closed. The steady state and transient response of the thermopneumatic action with various working liquids have been studied and the results show that Fluorinert^{TM} PF 5060 delivers the best thermopneumatic performance. Valves with various constructions have been tested extensively with nitrogen and water flow. A very low power consumption has been demonstrated. As low as 35.5 mW of power is sufficient to control a nitrogen flow of 1.04 lpm with an inlet pressure of 32 psi.

Although a low power high performance valve has been developed, several improvements can be made in the future. First, the current valve structure is very complicated and requires tedious hand aligning and assembling. The structure can be simplified by integrating several chips into one chip. Second, the deflection of current valve membrane is limited by Parylene layer. Larger deflection can be achieved by making the Parylene layer into a microbellow actuator. Third and most importantly, by integrating the valve with other fluid devices, such as flow channel, reservoirs, and pumps, an integrated fluid handling system can be made.